A STUDY OF PLASMA SOURCE ION IMPLANTATION

BY

KIM THOMAS

Submitted in partial fulfillment of
the requirements for the degree of
Master of Science
in the
Department of Physics,
University of Natal, Durban

Durban
November 1993

PREFACE

The work described in this thesis was carried out at the Plasma Physics Research Institute at the University of Natal, Durban, from July 1992 to November 1993 under the supervision of Doctor M. J. Alport.

These studies represent the original work and have not been submitted in any form to another University. Unless otherwise stated, the work presented is that of the author's. Where use was made of the work of others, it has been duly acknowledged in the text.

ACKNOWLEDGMENTS

I wish to thank my supervisor, Mike Alport for his guidance and many helpful discussions during the progress of this study. I am also grateful to Terry Sheridan, who provided, and patiently explained the PLANAR.C program.

I would also like to thank Clemens Dempers for technical guidance (taking apart computers), advice (don't do this degree!!!) and humour (or sarcasm), which made this project a lot more fun.

Thanks also to Terry Nicklin, for all the interruptions! Thanks to my father, for some financial assistance.

Thanks are also due to the Foundation for Research and Development for funding this research.

ABSTRACT

The work described in this thesis is an analysis of the Plasma Source Ion Implantation (PSII) process. A metal target is placed within a plasma, and pulsed to a high negative potential (10 - 50 kV). The electrons in the plasma close to the target are then repelled very rapidly, leaving an area of uniform positive charge. This causes an electric field to be set up between the plasma and the metal target. The ions close to the target are then accelerated towards the target by the electric field. The ions reach the target at high velocities, and implant deeply into the metal (~5 x 10^{-8} m), and form nitrides, which pin dislocations within the metal's atomic structure. The strength of the metal is therefore increased, and other properties such as the corrosion resistance of the metal are also improved. Metals that have undergone the PSII process have widely diverse applications. For example, in the motor industry, ion implanted metal punches last much longer than nitrided punches, while in the medical industry ion implanted metals are used for artificial limbs.

A combination of a number of different analytic, numerical and simulation models are used to describe the PSII process, including the plasma behaviour and final nitrogen implantation profile in the metal target after the application of the voltage pulse. In all cases, a specific attempt has been made to realistically describe as closely as possible, the actual experimental arrangement at the University of Natal. For example: a waveform with a fast rise time, short plateau and exponential decay was used; the nitrogen plasma was more realistically described by a two species fluid to account for the measured N^+, N_2^+ mix; and finally, the actual atomic composition for 304 stainless steel was used in the TAMIX particle simulation.

This work thus models the whole PSII process, and could form the basis of future studies for the optimisation of the process.

LIST OF SYMBOLS

PLASMA PARAMETERS

ε_0	permittivity of free space
λ_D	Debye length
ϕ, V	potential
ω_{pe}	electron plasma frequency
ω_{pi}	ion plasma frequency
c_s	ion sound speed
e	electron charge
E	electric field
k	Boltzmann constant
m	electron mass
M	ion mass
n_0	total initial density
n_e	electron density
T_e	electron temperature

ANALYTICAL MODEL

τ	normalized time
τ_r	time over which the potential rises to V_0
τ_p	time at which the potential remains at V_0
τ_f	time that the potential takes to fall to zero or a fraction of V_0
j	current density
J	normalized current density
s	sheath width
S	normalized sheath width
t	time
V_0	peak potential
$\tilde{V}$	normalized potential

NUMERICAL MODEL

α	ion mass ratio
ξ	normalized position
η	normalized potential
ω_{pi1}	ion plasma frequency, relative to ion 1
ω_{pi2}	ion plasma frequency, relative to ion 2
$M_{1,2}$	mass of ions in fluid 1,2
$n_{i1,2}$	initial density of ion fluid 1,2
$\tilde{n}_e$	normalized electron density
$\tilde{n}_{i1,2}$	normalized initial density of ion fluid 1,2
$q_{1,2}$	charge on ions in fluid 1,2

CONTENTS

CHAPTER 1

INTRODUCTION

1.1 INTRODUCTION

This thesis describes an analytical, numerical and Monte Carlo analysis of the Plasma Source Ion Implantation (PSII)[1,2] process. Surface modification by plasma source ion implantation has been shown[3] to produce an improvement in the corrosion, fatigue and friction properties of materials as well as substantially improving the life of cutting tools such as punches[2], taps, dies and cutting inserts. PSII also holds great promise for the surface modification of other industrial materials including metals, plastics and ceramics.

At present, ion plating and nitriding are the more popular methods of surface modification, where the tool surface is coated with a protective layer. In the ion plating process, titanium nitride (TiN) is generally used. In Figure 1a[37], electrons are accelerated towards a Ti deposit. The Ti deposit is evaporated, and forms a gas within the vacuum vessel, at a pressure of ~3 mTorr, which is larger than that required for PSII (10^{-4} Torr). This Ti gas may be mixed with nitrogen or other gases, depending on the desired coating. A coating forms (5-6 μm) on the substrate (which is at ~500°C), by a combination of diffusion and bombardment by ions of low energy (1-5 keV).

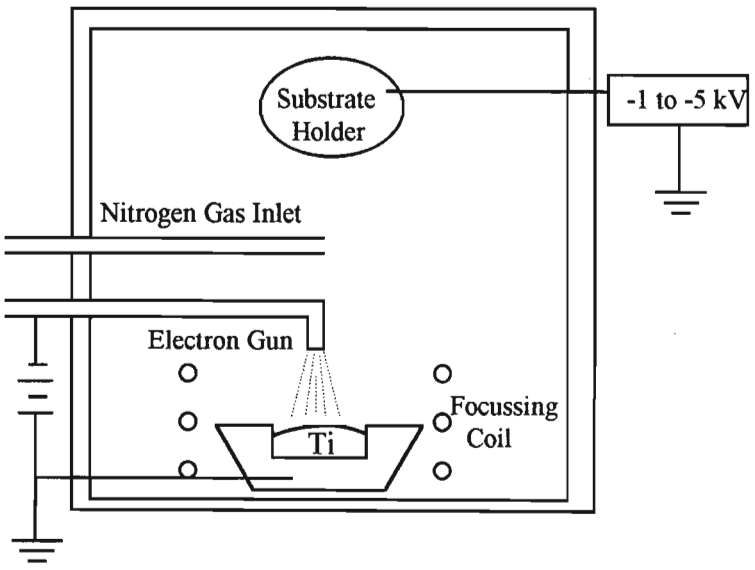

Fig 1a. Ion plating.

Conventional ion implantation, as used for example in the production of semi-conductor wafers, is a process in which ions are extracted from an ion source, which may be a plasma, and accelerated as a beam to high energy, and then raster scanned across the target. This means that only those parts of the target that are in line of sight of the ion beam will be exposed to ion implantation. If the target is complicated in shape, then the ion beam may not strike the target surface perpendicularly, which results in damage of the target surface by sputtering. For a complicated target shape, this process in addition requires 3 dimensional target manipulation, as shown in Figure 1b.

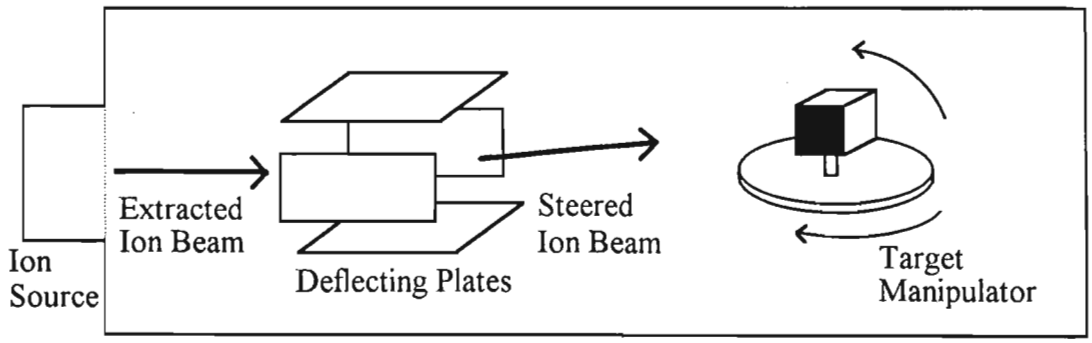

Fig 1b. Conventional Beamline Ion Implantation

In the PSII process, however, the object that is to be ion implanted is actually immersed in the plasma, as shown in Figure 1c.

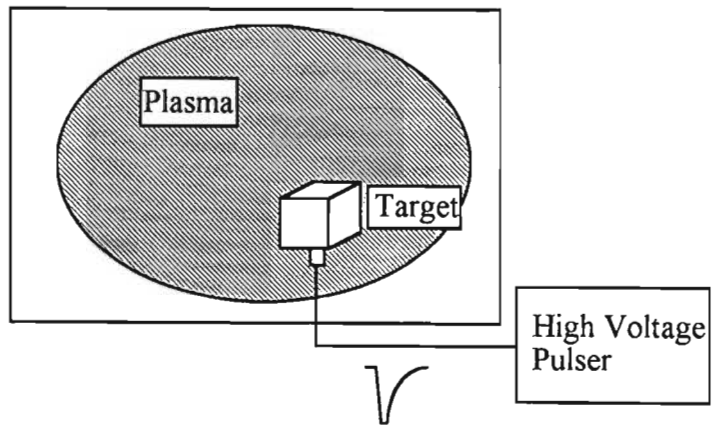

Fig 1c. Plasma Source Ion Implantation

The target is then repeatedly pulsed to a large negative potential (V_0~10-50 kV), which has the effect of repelling the surrounding electrons, thereby forming a sheath around the target. The plasma ions are then accelerated by the electric field set up in the sheath, causing them to bombard the entire target surface with approximately normal angle of incidence. This is a major improvement over conventional ion implantation, as the line-of-sight limitation in conventional ion implantation is no longer a problem in PSII. In comparison to nitriding, PSII has a number of advantages[1-3]: the surface

properties of materials can be changed without altering bulk material properties; there are no problems with bonding failure or delamination, since ion implantation is not a film or a coating; the ion implantation process is generally an athermal process, so that the workpiece will not distort or soften excessively; the implant depth is very thin (50 nm); there are no dimensional changes, and finally, ion implantation is a non-equilibrium process, so non-equilibrium phases or alloys can be formed. PSII does have the disadvantage that it is difficult to mount large or heavy objects, at high potential, in a plasma on insulated supports. In addition, it is difficult to provide the necessary current to the object. Furthermore, PSII can also be wasteful of the ion beam in that current has to be provided to all exposed surfaces even those that do not require it.

1.2 PLASMA PROCESSING IN INDUSTRY

In 1989, a Plasma Science Committee was established under the American National Research Council. Among its first projects, the committee produced a report on plasma processing of materials[4].

It was established that there are a large number of industrial applications for plasma-based systems for the processing and surface modification of materials, particularly in the electronics, aerospace and automotive industries. Plasma processing is also important in the biomedical and steel industries as well as in toxic waste management.

One of the reasons for the wide applicability of plasma processing is that plasmas provide a highly excited medium which has no chemical or physical counterpart in the natural, equilibrium environment. Plasmas are able to alter the normal pathways through which chemical systems evolve from one stable state to another, so that plasmas can potentially produce materials with specific properties not attainable by any other means. Because of the broad range of plasma conditions, geometries and excitation methods, the applications of plasma processing are diverse. Figure 2 shows a graph of plasma density as a function of electron temperature, illustrating the wide range of plasmas found in nature as well as the laboratory.

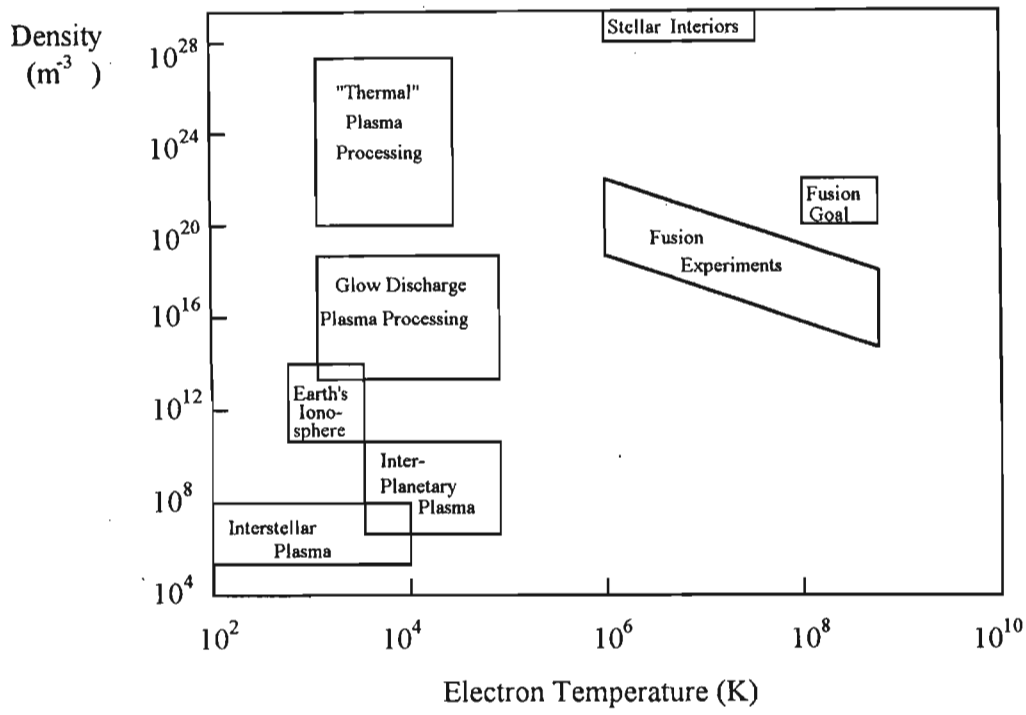

Figure 2. Plasma density is plotted as a function of electron temperature, to illustrate the wide range of plasmas found in nature as well as in the laboratory.

In America, in particular, plasmas are used in a large number of industrial applications. Some examples are[4]: plasma controlled anisotropic etching in fabrication of microelectronic chips; plasma-enhanced chemical vapour deposition (PECVD) of amorphous silicon films used in solar cells; plasma nitriding, which is used to harden the surface of steel and plasma sputter deposition of magnetic films for memory devices.

The electronics industry is undergoing rapid growth and expansion as the world becomes more and more dependent on electronic components. It is dependent on the semi-conductor industry, for the fabrication of microelectronic integrated circuits, the principal components of electronic systems. The ability to make large quantities of low-cost semiconductors depends directly on the quality of manufacturing equipment and materials. Plasma equipment and plasma processing are thus vital to the electronics industry.

For example, plasma processing is necessary to obtain high-density packing of microscopic circuit components, where anisotropic etching is essential. Wet chemical techniques used in the past result in isotropic etching, where both vertical and lateral etch rates are comparable (Figure 3). Only plasma etching provides the anisotropic etching and high fidelity pattern transfer capability needed.

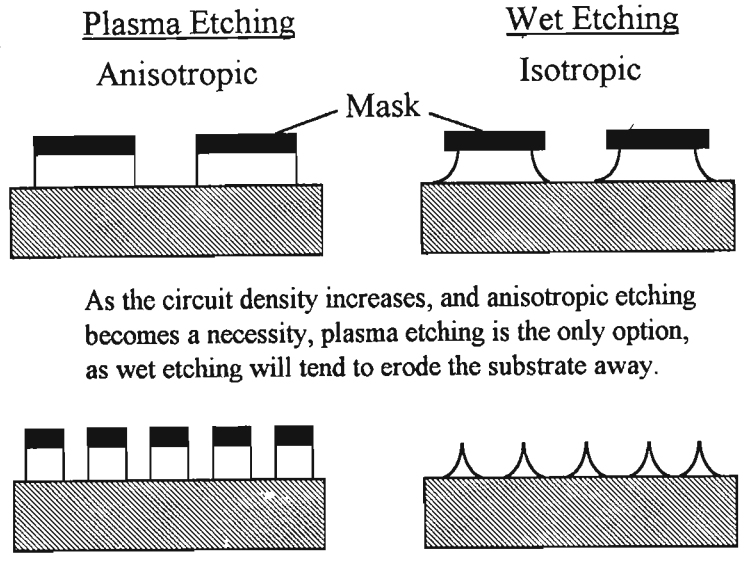

Fig. 3 A comparison of the results of plasma etching and wet chemical etching. For the accuracy needed in high density circuit components, plasma etching is essential.

PSII is likely to become an important part of plasma processing, particularly in the electronics, automotive, steel and biomedical industries, where its greater accuracy, cost efficiency and throughput[1-3] are advantageous.

1.3 COMPARISON OF PSII AND CONVENTIONAL METHODS.

In industry, where ion bombardment is used for surface modification, the conventional directed ion beam method is generally used. This conventional method is a line-of-sight process[1,2,3], where a directed beam of ions is rastered across the target. If the target is non planar, then it becomes necessary to manipulate the target to expose all surfaces to the ion beam. If the object is large or heavy, the process becomes less cost effective. Also, if the target's shape is complicated, shadowing and sputtering can occur, which reduces the retained dose of ions, D, which depends on the angle of incidence, θ, of the ion beam: $D \sim \cos\theta$ for low fluences and $D \sim \cos^{8/3}\theta$ for higher fluences[1,2,3]. As a result, for grazing angles of incidence, it is necessary to mask the target to allow for a uniform dose, leading to part of the ion beam being wasted on the masking material.

With PSII, because a plasma sheath forms around the target, the ions, attracted by the target's negative potential, are, in general, accelerated along the field lines, perpendicular to the target surface although recent work has shown that this does not necessarily occur at the sharp edges of a wedge shaped object[5,6,7]. This means that even if the workpiece is complicated in shape, shadowing is reduced and there is generally no need to mask or manipulate the target to produce a uniform surface depth profile of implanted ions. Also, if the pulse repetition rate is increased, the PSII process requires a much shorter implantation time than ion nitriding.

PSII has also resulted in improved microhardness wear properties[3]. There is increased resistance to adhesive and mild abrasive wear[3], while the coefficient of friction is reduced[2,3]. Another advantage is that, if the duty cycle is limited, the PSII process can be run at low temperatures so that surface properties are modified with no change in bulk properties, and no distortion of the implanted component will occur. As an example, an implanted gear would have exactly the same dimensions as a similar unimplanted gear.

PSII also greatly improves the life of manufacturing tools. For implanted tool steel, a high density of finely divided chromium nitrides are formed, which pin dislocations near surface - inhibiting fractures and back extrusion. For example, the lifetime of PSII-implanted M2 pierce punches improved by 70 - 80 times[2].

PSII also has biomedical applications. It enhances hardness[8], wear, fatigue, and corrosion resistance of biomedical devices such as knee, hip ball and wrist prostheses. It also enhances biocompatibility of implant materials due to ion assisted growth of thin hydroxyapatite films which enhance bone ingrowth.

1.4 OVERVIEW OF THESIS

The following chapter deals with a fuller description of the PSII process, as well as a survey of work performed in the PSII field.

Chapter three covers the theoretical aspects of each part of the work performed. Basic sheath theory is discussed and the plasma behaviour in the PSII process is described by three analytical models, a Runge-Kutta model and the numerical solution of plasma fluid equations. The TAMIX particle simulation program that describes the implantation of ions in a solid target is also discussed.

Chapter four describes the set-up of the plasma device that is used to implant small metal targets. Some experimental results obtained are compared with the results of the analytical and numerical models. The corresponding TAMIX results are also included.

Chapter five concludes this work with a review of the results and suggestions for further work in this field.

CHAPTER 2

PSII REVIEW

2.1 DESCRIPTION OF PSII

In the PSII process, the object that is to be hardened is immersed in a plasma, then repeatedly pulsed to a very large negative potential, (V_0~-50 kV). As the negative potential of the target increases, the electrons experience a repulsive force, and are accelerated rapidly away from the target's surface. This occurs over the very short time scale of the electron plasma period, ω_{pe}^{-1}. The more massive ions are effectively motionless over this time period, and form an homogeneous sheath around the target. This initial sheath is called an ion matrix sheath[2]. As the electrons are repelled further, the ion matrix sheath width increases rapidly, with the sheath edge moving outwards at roughly $20c_s$, where c_s is the ion sound speed.

Next, over the longer time scale of the ion plasma period, ω_{pi}^{-1}, ions are accelerated towards the target by the negative potential. As a result, the ion matrix becomes depleted. The sheath continues to move outwards, as more electrons are repelled to maintain charge neutrality within the plasma[9]. Over this time period, the sheath expansion velocity decreases to around c_s. The sheath will continue to expand outwards until the ion current across it is sufficient to equal the current drawn by the target. The question of whether the sheath reaches a final equilibrium position or not depends upon whether the ions have sufficient time to be accelerated by the presheath.

2.2 REVIEW OF RECENT WORK ON PSII

This section summarises previously published literature dealing with the theoretical and experimental aspects of PSII. The first papers deal with models for the PSII process, while the rest deal with comparisons of models with experimental data, or experimental data only. In this thesis, PSII is the term used to describe this ion implantation process. However, in the following papers, a number of other terms may be used, for example: Plasma Immersion Ion Implantation (PIII or PI[3]); Plasma Source Implantation (PSI) and Plasma Ion Implantation (PII). In the absence of a clear distinction between these other named processes, we shall rather use the more generic PSII nomenclature since it is this acronym that appears in the US patent (# 4,764,394). This patent (See Appendix B) covers the PSII method comprising: the provision of a chamber having electrically conductive walls; the suspension of a target within the chamber, spaced away from the

walls of the chamber; the evacuation of the interior of the chamber to a very low base pressure; the formation of a plasma of ions in the chamber around the target object, and the application of repetitive pulses of high voltage between the chamber walls and the target object, to draw plasma ions to the target object, at a voltage sufficient to implant the ions into the target, with the width of the pulses being selected so that the plasma sheath surrounding the target does not expand to contact the enclosure walls during the pulse.

CONRAD and FOREST[1] gave the first report of PSII at the IEEE International Conference of Plasma Science in Saskatoon, Canada in May, 1986. The PSII technique was being developed as a new, cost-effective ion implantation technique.

CONRAD *et al* [2] later presented another introductory paper, comparing conventional ion implantation to Plasma Source Ion Implantation. PSII was experimentally shown to implant ions to depths (~0.5 μm) and concentrations required for surface modification, as well as producing materials with improved micro-hardness and wear properties, dramatically improving the life of manufacturing tools in actual industrial applications.

CIPPOLA AND SILEVITCH[10] presented a 1 dimensional model for the time-dependent behaviour caused by placing an uncharged conducting surface in contact with a uniform equilibrium plasma. The formation and expansion of a quasi-neutral region connecting the non-neutral sheath with the distant undisturbed plasma was considered, with the validity of assuming the existence of a sheath edge also being questioned. The role of both static and dynamic Bohm sheath criteria in the theory of unsteady sheath development was studied. This formed the basis of many subsequent models of sheath behaviour.

LIEBERMAN[9] produced a one dimensional model of PSII, using a 'top hat' shaped voltage form. The target is immersed in a plasma and a series of negative high voltage pulses are applied to the target. This causes the formation of an ion matrix sheath. The ions in the sheath are accelerated towards the target, producing a time varying implantation current. A very simple analytical model is developed to determine the implantation current, as well as the total dose and the energy distribution of the implanted ions. The series of assumptions for this model are reasonable for low pressure plasmas, where the implantation time scale is much longer than the electron plasma period, and the applied voltage is much greater than the electron temperature so that the Debye length is much less than the ion matrix sheath width. This model produces an equation for the temporal sheath expansion, but is quite inaccurate for larger time scales, due to the large number of simplifying assumptions. The final current density function is also discontinuous, since the voltage form does not have a continuous first derivative.

STEWART AND LIEBERMAN[11] later improved on this model, developing another analytical model in 1 dimensional planar geometry, using a voltage form of trapezoidal shape with finite rise and fall times. This model determined the time varying

implantation current, the total dose and the energy distribution of the implanted ions. By comparison with numerical simulations, it was demonstrated that the accuracy of the model is characterised by the ratio of the ion flight time to the pulse rise time. This model also requires a very similar series of assumptions to Lieberman's first paper: collisionless ion flow again requires low density plasmas (in the paper, low pressure is used instead of low density, but low density seems more appropriate); the implantation time scale must again be much longer than the electron plasma period, and the applied voltage is required to be much greater than the electron temperature so that the Debye length is much less than the ion matrix sheath width. To prevent the plot of current density as a function of time from being discontinuous, the trapezoidal voltage form is 'rounded'. This works well if the rise, plateau and fall times are of the same order, but if the fall time is substantially larger than the rise time, the 'smoothed' voltage form is no longer very smooth. A trapezoid may be a good approximation for the voltage forms of some equipment, but for a pulse due to a capacitor discharge, its accuracy is limited. Another analytical model for this exponential voltage decay was developed by the author, and is described in Section 3.3.4.

SHERIDAN AND GOREE[12] derived an analytical expression for the spatial dependence of the electric potential in a collisionless and source free planar plasma sheath. The expression reduces to Child's Law as the potential drop across the sheath becomes large with respect to the electron temperature, T_e. Comparisons of the numerical solution of the model equations with the derived expression show that the expression is accurate for $|e\phi/kT_e| > 10$ which is a substantial improvement, as Child's Law is only accurate for $|e\phi/kT_e| > 10^4$.

QIN *et al* [13] developed a collisional one dimensional model that describes the response of a plasma to a high voltage pulse, as occurs in PSII. Their experimental measurements of sheath position and target current fitted well with the model. The predicted sheath width using a collisional model is much smaller than the sheath width predicted by similar non collisional models. A useful method for finding the initial ion matrix sheath width was also presented, allowing for an axially varying density profile.

SCHEUER *et al* [14] developed a one dimensional model that describes the motion of a transient sheath that forms around a conductor. This model assumes that the sheath obeys the Child Law at each instant in the propagation of the sheath. Because of this assumption, this model is not as accurate as the above two models, but does have the advantage of describing sheath propagation for planar, cylindrical and spherical geometries. Unfortunately, the results are not very convincing, since only 4 data points were used to compare experimental data with the two models. Based on this sparse data set, the conclusion was drawn that the drift velocity of incoming ions is negligible, greatly simplifying the basic equations.

CONRAD[15] obtained analytical expressions for the potential profile and sheath thickness of the transient ion-matrix sheath which forms when a large negative step potential is applied to planar, cylindrical and spherical electrodes which are immersed

in a plasma. Here, again, the assumption of an instantaneous switch on of the voltage limits the accuracy of the model.

SHAMIM *et al* [16] presented a comparison of experimental measurement and numerical calculations of temporal and spatial evolution of the plasma sheath, using spherical and cylindrical targets biased negatively to 20-50 kV in an Argon plasma of density 2×10^8 - 8×10^9 cm^{-3}. The numerical calculations were based, in part, on the Lieberman papers[9,11], and were in good agreement with the experimental measurements.

EMMERT and HENRY[17] have developed a one dimensional numerical simulation for the time evolution of the sheath in PSII. This model compared successfully with experimental results. The time-dependent potential profile is calculated from Poisson's Equation coupled with collisionless fluid equations for the ions and a Boltzmann distribution for the electrons. In addition to the potential profile the density profile, ion current to the surface and energy spectrum of ions incident on the surface are calculated. The simulation results tend to be quite oscillatory. This could possibly be rectified with greater resolution in the time steps.

CONRAD *et al* [3] used Rutherford back scattering spectroscopy and secondary ion mass spectrometry to characterise the dose uniformity of implanted ions on 4 spherical Ti-6Al-4V targets which were implanted simultaneously as a 2 x 2 square array in a nitrogen plasma. An applied potential of 50 kV and density of $n = 3 \times 10^9$ cm^{-3} resulted in a dose of 3×10^{17} atoms per square centimetre. The measured rms. variation of the retained dose and the statistical variance was less than 15%, which is well within tolerance range for non semiconductor applications of PSII. These results demonstrate that PSII can achieve acceptable uniformity on non planar targets without target manipulation, in batch processing mode.

DONNELLY and WATTERSON[5] used numerical methods to find the electric potential distribution in the stationary ion sheath that initially surrounds wedge shaped cathodes in a plasma, following the application of a large negative voltage pulse. It was found that for concave wedges, the sheath width increases and the electric field decreases near the wedge tip, so that ion currents will probably be smallest in that area. For convex wedges, the sheath width is smallest near the tip, but returns to the planar sheath width within a distance of less than the planar sheath width from the tip of the wedge. The electric field lines are concentrated towards the tip, suggesting that the largest ion current over a period longer than the ion plasma period will be in the region of convex edges. As a result, the dose to sharp edges would be enhanced.

WATTERSON[6] calculated numerically the steady state Child-Langmuir sheath around a wedge shaped cathode immersed in a plasma. It is assumed that all ions cross the interface between the plasma and the sheath with the same density and speed, perpendicular to the interface. Whether this is sufficiently accurate is not clear, without further modelling of the ion velocity distribution in the presheath. Ion collisions were

also neglected, thus these results would not apply for low voltages and high density plasmas. Ions drawn from the plasma by the electric field may either sputter material from the cathode or implant into the cathode, depending on the size of the applied negative voltage. The ion impact rate is 2.2 times higher near a square edge and 3.6 times higher near a knife edge than the ion impact rate for planar cathode surfaces. However, the ion impact rate falls to zero at the knife edge. All the ions strike the cathode with the same kinetic energy, but they do not strike perpendicularly near the cathode edge, which could reduce implantation depth and increase sputtering. Since the PSII process was developed with the thought that ions would implant perpendicularly, this result is quite ironic.

SHERIDAN and ALPORT[7] produced similar results for a trough, showing that the ions, while accelerated by the target potential, do not implant perpendicularly, as their own inertia plays a significant part in their motion.

TENDYS *et al* [18] generated medium and high density plasmas with low and medium power radio frequency techniques. The medium density plasma consisted mainly of N_2^+ ions with a density of 2-4 x 10^9 cm^{-3} and an electron temperature of 5 eV, and a negligible magnetic field. The high density plasma consisted mainly of N^+ ions with an ion density of 3 x 10^{12} cm^{-3} and a higher electron temperature of 10 eV. The high density plasma had a steady magnetic field of 5 mT. Both plasmas were run at a filling pressure of 1 mTorr. High densities are advantageous because the implantation time is lessened, and the sheath formed around the sample is smaller, so that for complicated shapes, implantation is more uniform. Problems were encountered with high density plasmas because the surface of the sample became damaged due to arcing between the plasma and the sample. The situation would be improved with better bias voltage circuitry and shorter pulse widths of less than 8 μs. It was also observed that penetration was enhanced when the temperature of the sample remained high for a long period of time, since greater diffusion into the cathode could occur.

TANG *et al* [19] determined ion species and their ratios in nitrogen, oxygen and argon plasmas, using a simple and low cost measurement system. The measured ion species ratio in the nitrogen plasma was used as an input parameter for the TAMIX simulation code, which predicts atomic composition as a function of depth. This data was in close agreement with data from an Auger analysis for a nitrogen implanted Ti-6Al-4V alloy. The paper describes the measurement system and gives percentages of ion species for different density plasmas. The ratios given here were used in this thesis, with 25% N^+ and 75% N_2^+ ions assumed to make up the total plasma density.

QIN *et al* [20] computed the ion energy distribution during PSII. The model is based on collisions resulting in charge transfer in a dynamic sheath. The charge transfer cross section is found to be of the order of 2.3 x 10^{-15} cm^2. Experimental results for boron ion energy distribution were consistent with the theoretical predictions. Both experimental and theoretical results indicate that the ions have a wide energy

distribution, and many of the ions have low energies due to collisions in the sheath. These low energy ions would tend to cause sputtering of the target. The ion densities in this experiment were fairly high (10^9 - 10^{12}) so that it is necessary to take collisions into account.

VAREY and SANDER[21] measured the growth of an ion sheath formed on a plane electrode in a mercury plasma of density 10^{10} - 10^{11} cm^{-3}. The electrode potential changed at a rate of up to 3 $kV.\mu s^{-1}$ and reached a maximum value of -10 kV. The thickness of the sheath is compared with various theoretical models. An expression for the current flowing in the sheath is derived and compared with experimental results, with reasonably good agreement.

SZAPIRO *et al* [22] measured the secondary electron emission coefficient of various materials undergoing helium ion bombardment in the energy range 0.5 to 20 keV, for cathodes in high voltage discharges. The surfaces of the different materials were conditioned by operating the materials as cold cathodes in a high voltage discharge before electron yield measurement. Both the cathode samples and the discharge anode are water cooled. Of the materials tested, oxidised magnesium had the largest electron yields per ion: around 9 per 20 keV helium ion. Stainless steel had a yield of around 3 electrons per 20 keV helium ion.

SZAPIRO and ROCCA[23] measured the electron yields of 7 glow-discharge cathode materials under bombardment by neon and argon ions with energies in the range of 1 to 20 keV. The surfaces were conditioned as above[22]. The dependence of electron yield on ion velocity was found to be approximately linear for all gases and surfaces tested, with the slopes being strongly dependent on the cathode material. Of the materials tested, oxidised magnesium again had the largest electron yields per ion: around 16 per 20 keV neon ion or 12 per 20 keV argon ion. Stainless steel had a yield of around 5 electrons per 20 keV neon ion or 4 per 20 keV argon ion. The glow discharge current intensity was found to increase very rapidly with electron yield.

SHAMIM *et al* [24] developed an experimental procedure to measure electron emission due to energetic ion bombardment during PSII. This is useful for comparison of the model with experimentally-collected currents. The electron emission coefficient, γ, for 20 keV argon ions incident on type 304 stainless steel was found to be 4.

SHAMIM *et al* [25] made a comparison of experimental measurements and numerical calculations of temporal and spatial sheath evolution for planar targets. It was found that the propagating sheath edge initially emanates in an ellipsoidal shape elongated along the shape of the target, and then transforms to a spherical shape at a distance of ~ 1 diameter from the target. It was also found that the sheath eventually becomes stationary at a distance dependent on the plasma parameters and target dimensions. Silicon wafers were implanted with nitrogen, and surface profilometry and scanning Auger microprobe measurements showed greater sputtering and shallower implantation depths at the edge of the wafer, in qualitative agreement with the sheath

expansion measurements. A number of the results agree with the results presented in this thesis, although there is a dependence on the specific plasma parameters used. The target ion current calculation was presented for a very small time scale (15 μs), though, and with low resolution (2 μs).

WEI *et al* [26] performed wear tests of ferrite (pure a-Fe) and austenite (AISI 304 SS) implanted with nitrogen, using a unique oscillating pin-on-disk test machine. The results show that nitrogen implantation at elevated temperatures to high doses dramatically improves the adhesive wear resistance of ferrite and the critical load at which the wear changes from mild to severe adhesive wear for 304 SS. It was also established that nitrogen does diffuse into both the ferrite and the 304 SS rapidly when they are implanted at an elevated temperature, and that this enhances their wear resistance. An important result in this paper is that nitrides do not break up during the wear process, so that diffusion of the nitrogen during wear is unlikely. Previous wear testing made use of a fixed pin device, and the data from this testing was erroneously interpreted to indicate that nitrogen migration occurred. It was concluded that the oscillating pin device should be used as a wear tester in future.

For this thesis, great use was made of the two papers by Lieberman[9,11], as well as the paper by Qin *et al* [13] which gave a calculation of and an analytical expression for the ion matrix sheath width. The data produced by Tang *et al* [19] was also very useful for predicting the percentages of each kind of nitrogen ion. The analytical expression for the spatial dependence of the electric potential given by Sheridan and Goree[12] was also useful.

CHAPTER 3

THEORY

3.1 INTRODUCTION

In the literature, a number of models for the PSII process have been proposed. Analytic expressions to describe the one dimensional ion matrix sheath (the sheath that exists before the ions have had time to respond to the target voltage), its subsequent evolution and potential profile for planar, cylindrical and spherical electrodes have been obtained in various papers[9-11,13-17]. Generally, the electron density is assumed to be zero during the ion matrix phase of the sheath evolution, and the ion density is assumed to remain at the initial density. This greatly simplifies the one dimensional Poisson's equation, which is then solved with the additional assumption that the potential at the sheath edge is zero and that the potential at the target is equal to the applied potential.

The analytical model developed by Lieberman[9] describes the time varying implantation current, the total dose and the energy distribution of the implanted ions for an applied potential having a 'top hat' shape. Ion collisions are neglected, and it is assumed that electron motion is inertialess. These assumptions are reasonable for low gas pressures and time scales that are large in comparison to ω_{pe}^{-1}. The applied potential is also assumed to be much larger than the electron temperature, so that the Debye length is much less than the initial ion matrix sheath width, with the result that the sheath edge can be assumed to be abrupt. Two more assumptions are made that limit the generality of the model. Firstly, it is assumed that during and after matrix sheath implantation, a quasi static Child Law sheath forms. Secondly, during the motion of an ion across the sheath, the electric field is frozen at its initial value and remains time independent, except for the change due to the velocity of the moving sheath.

This model was later improved by Stewart and Lieberman[11], to describe a trapezoidal voltage form. All the above assumptions, however, remain unchanged, except that the physical picture of the formation of a nearly instantaneous ion-matrix sheath is replaced by a gradually expanding non uniform sheath. This determines the time evolution of the implanted ion current and energy distribution. For a low density plasma and a large negative potential, these assumptions are reasonable. It is necessary to adapt this model to describe the sheath expansion and current density generated for the Natal University experimental R-C discharge, where the voltage form consists of a short rise (1-2 μs), a short plateau (~10 μs) and then an exponential drop over a long time scale (~200 μs). Firstly, however, it is necessary to study the formation of the initial ion matrix sheath.

3.2 DEVELOPMENT OF THE ION MATRIX SHEATH.

3.2.1 Time Scales

In PSII, a very large negative potential is applied to a target which is immersed in a plasma: $|V_0| \gg kT_e/e$. Three time scales are important in the formation and evolution of the sheath. At time $t = 0$, the target is at zero potential. As the negative potential of the target increases to V_0, the electrons in the region near the target are repelled. This occurs on a time scale of the electron plasma period, $\omega_{pe}^{-1} = \sqrt{(n_0 e^2)/(\varepsilon_0 m_e)} \sim 10^{-10}$ s, for a medium density plasma ($n_0 = 10^9$ cm^{-3}). Over this time scale, the motion of the far more massive ions is negligible. As a result, the electrons leave behind an ion matrix - a region of uniform ion space charge. Over the slower time scale of the ion plasma period, $\omega_{pi}^{-1} = \sqrt{(n_0 e^2)/(\varepsilon_0 M)} \sim 10^{-6}$ s, ions are accelerated towards the electrode by the potential drop between the neutral plasma and the negatively charged target. The ions are moving at high velocities when they reach the target and are implanted. On an even longer time scale, the decreasing charge density inside the sheath region causes the sheath to expand into the plasma at the ion acoustic velocity, $c_s = \sqrt{(kT_e)/M} \sim 10^3$ m.s^{-1}.

3.2.2 Ion Matrix Sheath Width

To calculate the ion matrix sheath width, Poisson's equation, $\nabla^2\phi = -\frac{e}{\varepsilon_0}(n_i - n_e)$, is solved, with the assumption that the electron motion is instantaneous, so that the electron density, $n_e = 0$ within the sheath. Generally, plasma ion density, n_i, is assumed to be constant, which is a reasonable assumption for most plasma sources. For completeness, however, the model developed by Qin *et al* [13] is reviewed here. In this model, the plasma ion density is assumed to increase linearly in the axial (z) direction, so that the ion density is given by $n_i(z) = n_0 + (dn/dz)z$. Poisson's equation is now:

$$\frac{d^2\phi}{dz^2} = \frac{-e}{\varepsilon_0}\left(n_0 + \frac{dn}{dz}z\right) \qquad (1)$$

This equation is solved under the additional assumptions that at the ion-matrix sheath edge, s_0, the electric field, $\mathbf{E}(s_0) = 0$ and the potential, $\phi(s_0) \approx 0$. The applied potential, V_0 is also assumed to be much greater than the electron temperature, T_e. Integrating twice and applying the boundary conditions, $\mathbf{E}(s_0) = 0$, $\phi(s_0) = 0$ and $\phi(0) = -V_0$ yields:

$$V_0 = \frac{e}{\varepsilon_0}\left(\frac{n_0}{2}s_0^2 + \frac{1}{3}\frac{dn}{dz}s_0^3\right) \qquad (2)$$

Equation 2 can be solved for the ion matrix sheath width, s_0 as a function of density, n_0, density gradient, dn/dz, and applied peak potential, V_0. Figure 4 shows (dotted line)

$s_0(V_0)$ using the experimental parameters given in Qin's[13] paper $n_0 = 2 \times 10^{10}$ cm^{-3} and $dn/dz = 0.75 \times 10^{10}$ cm^{-3} cm^{-1}. For comparison, $s_0(V_0)$ is also shown (solid line) for $dn/dz = 0$.

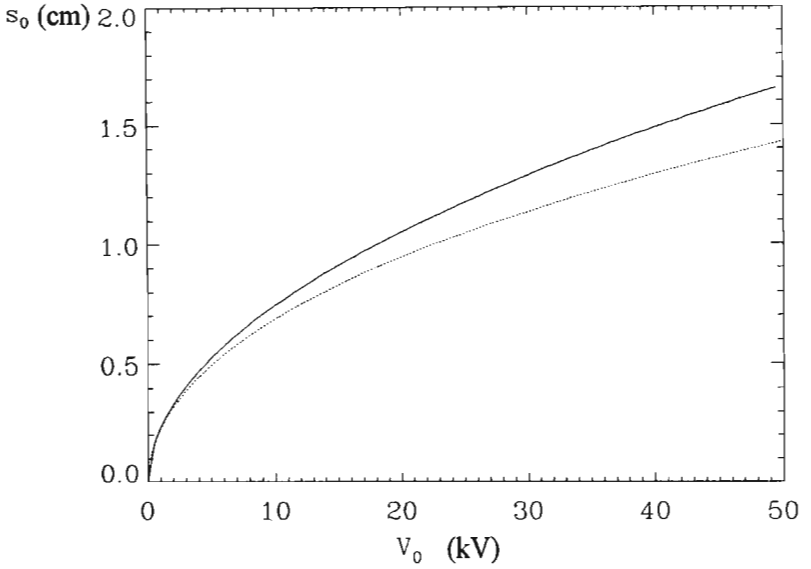

Fig. 4 Ion matrix sheath width as a function of applied peak potential, V_0 from (2), for $n_0 = 2 \times 10^{10}$ cm^{-3} and $dn/dz = 0.75 \times 10^{10}$ cm^{-3} cm^{-1}. For comparison, $s_0(V_0)$ is also shown (solid line) for $dn/dz = 0$.

Figure 5 shows the variation of s_0 with plasma density, n_0, for peak voltage $V_0 = 10$ kV, consistent with the peak voltage used in the experiment performed at Natal University. The dotted line is for a density gradient $dn/dz = 0.75 \times 10^{10}$ cm^{-3} cm^{-1} while the solid line is for $dn/dz = 0$. Over the density range shown, these two lines are indistinguishable to within a maximum of 0.001 % for $s_0 = 12$.

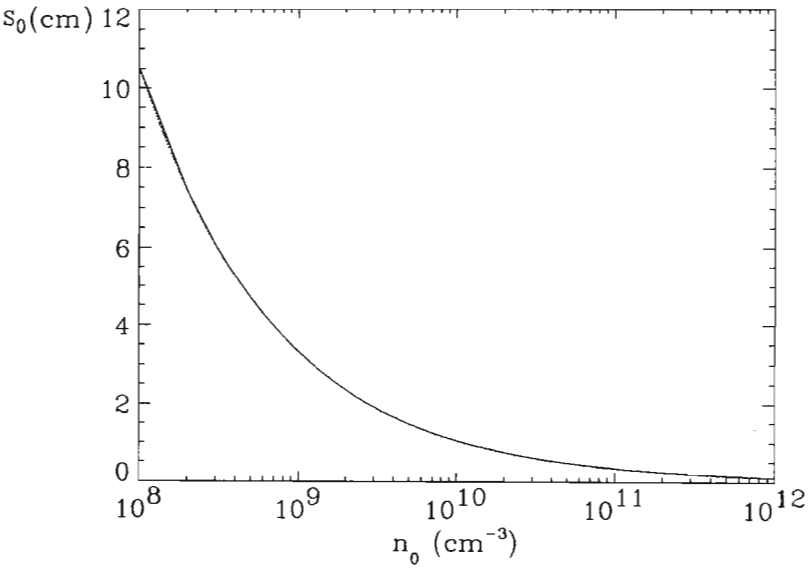

Fig. 5 Ion matrix sheath width as a function of initial plasma density, n_0, with $V_0 = 10$ kV and $dn/dz = 0.75 \times 10^{10}$ cm^{-3} cm^{-1} (dotted line) and $dn/dz = 0$ (solid line). The two lines are virtually indistinguishable.

It follows from Figures 4 and 5 that it is reasonable to neglect the density gradient for the experimental peak potential of 8 - 10 000 V and density of 10^9 - 10^{10} cm^{-3}. The width of the ion matrix sheath can thus be approximated by:

$$s_0 = \sqrt{(2\varepsilon_0 V_0)/(e n_0)} \quad \text{or}$$
$$s_0 = 1052\sqrt{V_0/n_0} \qquad (3)$$

where the second equation gives s_0 in cm, for n_0 in cm^{-3}.

3.3 ANALYTICAL MODELS

The following symbols will be used in the discussion that follows. Real time is represented by t, while normalised time is represented by $\tau = \omega_{pi} t$, where ω_{pi} is the ion plasma frequency. Voltage is represented by V and the normalised voltage by $\tilde{V} = V/V_0$, where V_0 is the peak voltage. Sheath width is represented by s and $S = s/s_0$ where s_0 is the initial ion matrix sheath width. Current density is represented by j and $J = j/e n_0 u_0$ where e is the electron charge, n_0 is the initial plasma density and u_0 is the characteristic ion velocity, given by $u_0 = \sqrt{2eV_0/M}$. In the Natal University experimental results were obtained for an argon plasma with target peak potential V_0 = 10000 V, ion mass M = 39.948 a.m.u., plasma density n_0 = 10^8 cm^{-3} and electron temperature T_e = 2 eV.

The following models (3.3.1, 3.3.2 and 3.3.3) make use of the assumption that a quasistatic Child law sheath forms during and after the formation of the ion matrix sheath. The Child law is based on the assumption that all current to the cathode (target) is provided by a Bohm ion flux at the sheath boundary. This is not the case, and provokes a valid criticism as there is no justification in using the Child law to describe a non-equilibrium sheath, particularly if the current due to the sheath expansion is larger than the current due to the ion flux at the sheath boundary.

3.3.1 Lieberman Model

3.3.1.1 Voltage Profile

Lieberman[9] produced the first analytical model for the PSII process. This model was developed to describe the sheath propagation for a simple top hat voltage form as shown in Figure 6:

$$\tilde{V}(\tau) = \frac{V}{V_0} = \begin{cases} 0 & \tau < 0 \\ 1 & 0 \le \tau \le \tau_p \\ 0 & \tau > \tau_p \end{cases} \qquad (4)$$

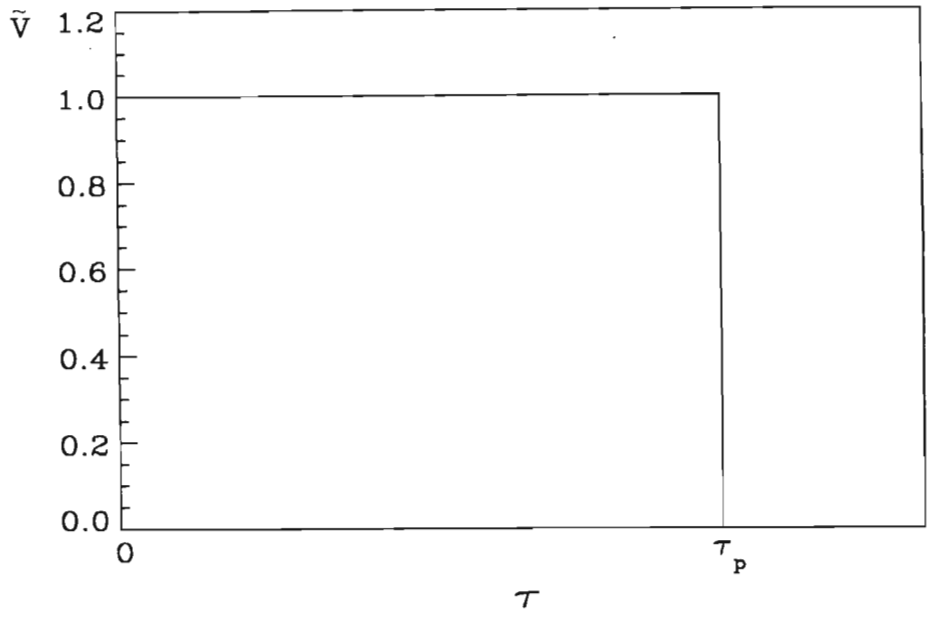

Fig 6 A plot of normalised target potential as a function of normalised time.

The following section shows how the sheath edge position as a function of time was derived by Lieberman[9], using this voltage form.

3.3.1.2 Sheath Edge Motion

The ion matrix sheath is assumed to form instantaneously. The Child law current density for ions of charge e and mass M for a voltage V_0 across a sheath of thickness s is given by[27,28]:

$$j_c = \frac{4}{9}\left(\frac{2e}{M}\right)^{1/2} \varepsilon_0 \frac{V_0^{3/2}}{s^2} \qquad (5)$$

This current density is equated to the charge crossing the sheath boundary per unit time, $j = en_0v$. Here, v is the sum of the velocity of the sheath, ds/dt, and the velocity at which the ions enter the sheath. This is assumed to be the Bohm velocity[29], $c_s = \sqrt{kT_e/M} \sim 10^3$ m.s^{-1}, the velocity at which ions enter a stationary sheath.

$$j_c = e n_0 \left(\frac{ds}{dt} + c_s\right) \qquad (6)$$

Initially, the sheath expands at a rate $ds/dt \sim 20\ c_s$, so that the applicability of the c_s term is questionable. In both Lieberman[9,11] models, the c_s term is neglected. Equations (5) and (6) are combined and solved for ds/dt:

$$\frac{ds}{dt} = \frac{2}{9}\frac{s_0^2 u_0}{s^2} - c_s \qquad (7)$$

where, according to (3), $s_0 = \sqrt{2\varepsilon_0 V_0/en_0}$ is the initial ion matrix sheath width and $u_0 = \sqrt{2eV_0/M} \sim 10^6$ m.s^{-1} is the characteristic ion velocity ($u_0 \gg c_s$). Normalisation

and integration of this equation results in the following form for the sheath width as a function of time, if terms smaller than $s_c = s_0\sqrt{\frac{2}{9}u_0/c_s}$, the steady state Child Law sheath width, are neglected.

$$S = \left(\frac{2}{3}\tau + 1\right)^{1/3} \tag{8}$$

As previously defined, $S = s/s_0$ is the normalised sheath width and $\tau = \omega_{pi}\, t = u_0/s_0\, t$ is the normalised time. The above equation is only valid for $s < s_c$, where $s_c \sim 15\ s_0$. Figure 7 shows a plot of sheath width as a function of time calculated from equation (8).

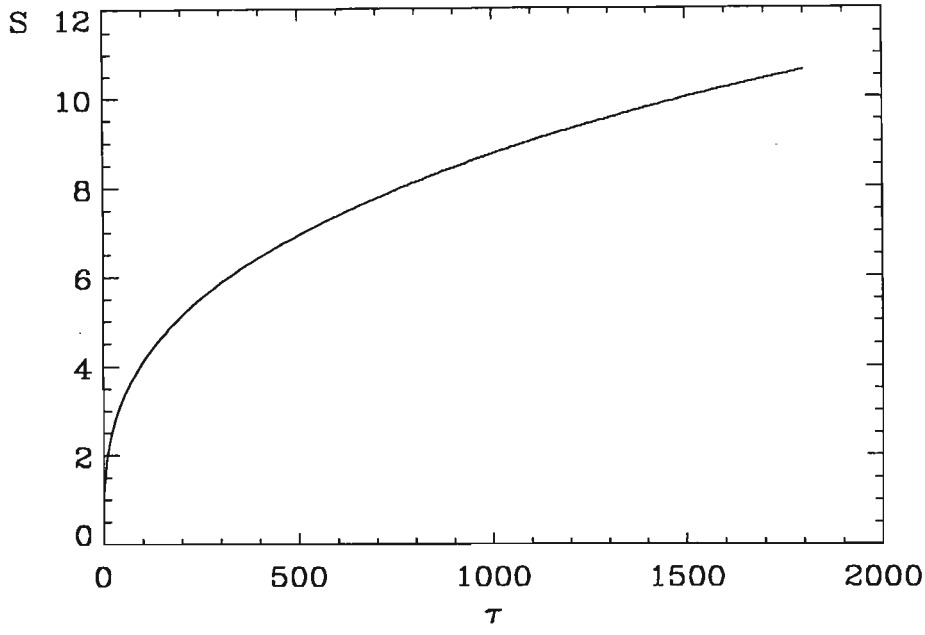

Fig. 7 The normalised sheath width is plotted as a function of normalised time, with S = 1 (s = s_0) at $\tau = 0$.

The effect of the c_s term is discussed in more detail in Section 3.3.4.

3.3.1.3 Current Density

The current density and energy distribution are calculated for two different time regimes. The current density due to the initial ion matrix sheath is calculated, using the fact that the charge density in the ion matrix sheath is initially uniform, so that the electric field varies linearly with position, x. Thus, the ion motion is given by:

$$\begin{aligned}\frac{d^2x}{dt^2} = \frac{e}{M}E &= \omega_{pi}^2\,(x - s) \\ &= \omega_{pi}^2\,(x - s_0) - \frac{2}{9}\,u_0\,\omega_{pi}^2\,t\end{aligned} \tag{9}$$

neglecting c_s in (7), and using the result that:

$$s = s_0 + \left.\frac{ds}{dt}\right|_{t=0} t = s_0 + \frac{2}{9}\frac{s_0^2 u_0}{s_0^2} t \qquad (10)$$

Integrating the differential equation (9) gives the particle position, x, as a function of time. Next, in a time interval dt, ions from a region dx are implanted into the target. The implantation current density $j = e\, n_0\, dx/dt$ is normalised to give[9]:

$$J(\tau) = \frac{\sinh\tau}{\cosh^2\tau} + \frac{2}{9}\left(\frac{1+\tau\sinh\tau+\cosh\tau}{\cosh^2\tau}\right) \qquad (11)$$

for $0 < x_0 < s_0$, or equivalently, $0 < \tau < 2.7$.

Next, the current density due to the ions initially outside the ion matrix sheath ($x_0 > s_0$) is considered. The assumption is that the current demanded by the sheath is supplied by uncovering ions at the moving sheath edge and by the drift of ions towards the target at c_s. The sheath edge reaches an ion at x_0 within the plasma, with time τ_s given by (8),

$$\tau_s = \omega_{pi}\, t_s = \frac{3}{2}\left(\frac{x_0^3}{s_0^3} - 1\right) \qquad (12)$$

At this time, the ion begins its flight across the sheath. The electric field is assumed to be frozen at its initial value. The flight time is given by[27]:

$$\tau' = \omega_{pi}\, t' = 3\frac{x_0}{s_0} \qquad (13)$$

Finally, an ion initially at x_0 reaches the target at $\tau = \tau_s + \tau'$:

$$\tau = \omega_{pi}\, t = \frac{3}{2}\left(\frac{x_0^3}{s_0^3} - 1\right) + 3\,\frac{x_0}{s_0} \qquad (14)$$

Differentiating this equation and solving for dx_0/dt yields :

$$\frac{dx_0}{dt} = u_0\left(\frac{9}{2}\frac{x_0^2}{s_0^2} + 3\right)^{-1} \qquad (15)$$

And, finally, the normalised current density as a parametric function of time is[9]:

$$J = \left(\frac{9}{2}\frac{x_0^2}{s_0^2} + 3\right)^{-1} \qquad (16)$$

Now, the minimum value for τ in (14) is for $x_0 = s_0$, when $\tau = 3$. In equation (11), the maximum value for τ is only $\tau \sim 2.7$. As a result, there is a discontinuity, brought about by the simplifying assumptions. Figure 8 shows current density as a function of time.

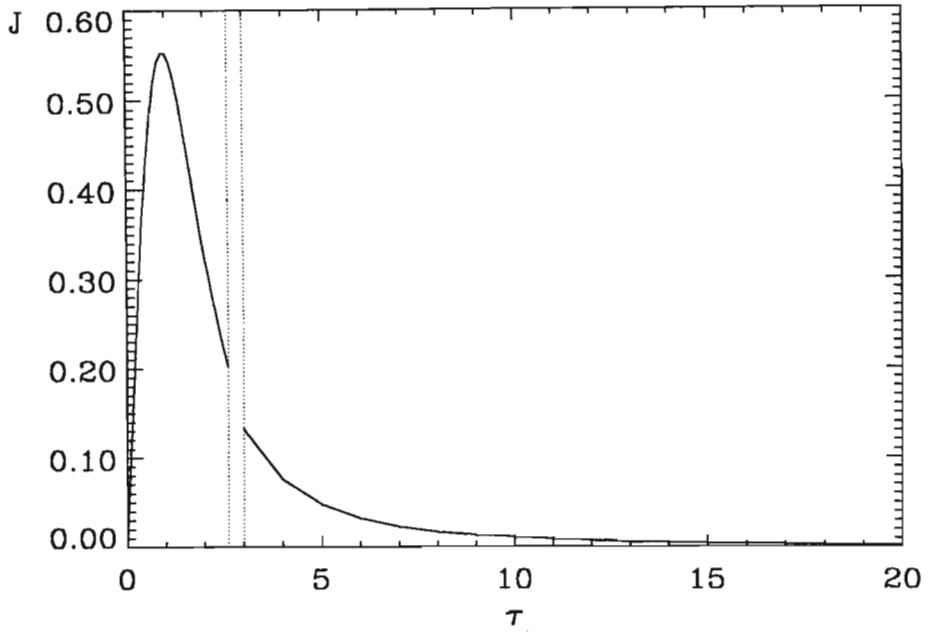

Fig. 8 Current density plotted as a function of time. The discontinuity occurs in both J and τ.

3.3.1.4 Energy Distribution

The pulse width, τ_p is assumed greater than 3, so that all matrix sheath ions will be implanted, as well as ions uncovered by the expanding sheath. These cases are dealt with separately, and the final energy distribution is formed from the sum of the energy distributions for each case.

For the matrix sheath ions, the potential varies quadratically with distance from sheath edge, so that an ion starting at $x_0 < s_0$ implants with an energy

$$W = V_0\left(1-\left(1-\frac{x_0}{s_0}\right)^2\right) \qquad (17)$$

where W is measured in the units of V_0.

Within the energy interval dW, there are $dN = n_0 dx_0$ ions per unit area implanted:

$$\frac{dN}{dW} = \frac{n_0 s_0^2}{2} V_0 (s_0 - x_0) \qquad (18)$$

Substituting (17) into (18) yields:

$$\frac{dN}{dW} = \frac{n_0 s_0}{2V_0^{1/2}} (V_0 - W)^{-1/2} \qquad (19)$$

For $\tau_p > 3$, all the ions from $s_0 < x_0 < x_\tau$ implant at full energy ($W = V_0$). The value of x_τ is found from (14):

$$\tau_p = \frac{3}{2}\left(\frac{x_\tau^3}{s_0^3} - 1\right) + 3\frac{x_\tau}{s_0}, \tag{20}$$

A Dirac delta function is used to give the value of dN/dW at $W = V_0$ in the distribution:

$$\frac{dN}{dW} = n_0(x_\tau - s_0)\,\delta(W - V_0) \tag{21}$$

At τ_p, the sheath has reached a width s_τ given by (12). The ions originally at $x_\tau < x_0 < s_\tau$ are in transit across the sheath, when the pulse is turned off. The density and potential in the sheath just before turnoff are given by[27]:

$$\begin{aligned} n(x_0) &\propto \left(\frac{s_\tau}{s_\tau - x_0}\right)^{1/3} \\ \phi(x_0) &= -V_0\left(\frac{s_\tau - x_0}{s_\tau}\right)^{5/3} \end{aligned} \tag{22}$$

The ion energy is then given by:

$$W(x_0) = -V_0\left(1 - \left(\frac{s_\tau - x_0}{s_\tau}\right)^{5/3}\right) \tag{23}$$

Finally, normalising so that $N = n_0(s_\tau - x_\tau)$:

$$\frac{dN}{dW} = \frac{2}{5}\frac{s_\tau - x_\tau}{V_0^{2/5}} n_0 (V_0 - W)^{-3/5} \tag{24}$$

The total energy distribution is now the sum of the three distributions above. The total implanted dose will be $n_0 s_\tau$.

$$\frac{dN}{dW} = \left[\frac{n_0 s_0}{2V_0^{1/2}}(V_0 - W)^{-1/2}\right] + \left[n_0(x_\tau - s_0)\,\delta(W - V_0)\right] + \left[\frac{2}{5}\frac{s_\tau - x_\tau}{V_0^{2/5}} n_0 (V_0 - W)^{-3/5}\right] \tag{25}$$

In Figure 9, the energy distribution, dN/dW, is plotted as a function of ion energy, W. The dotted line corresponds to the first term, while the dashed line corresponds to the third term. The second term is finite only at $W = 10000$, where its value is approximately 2×10^{14}.

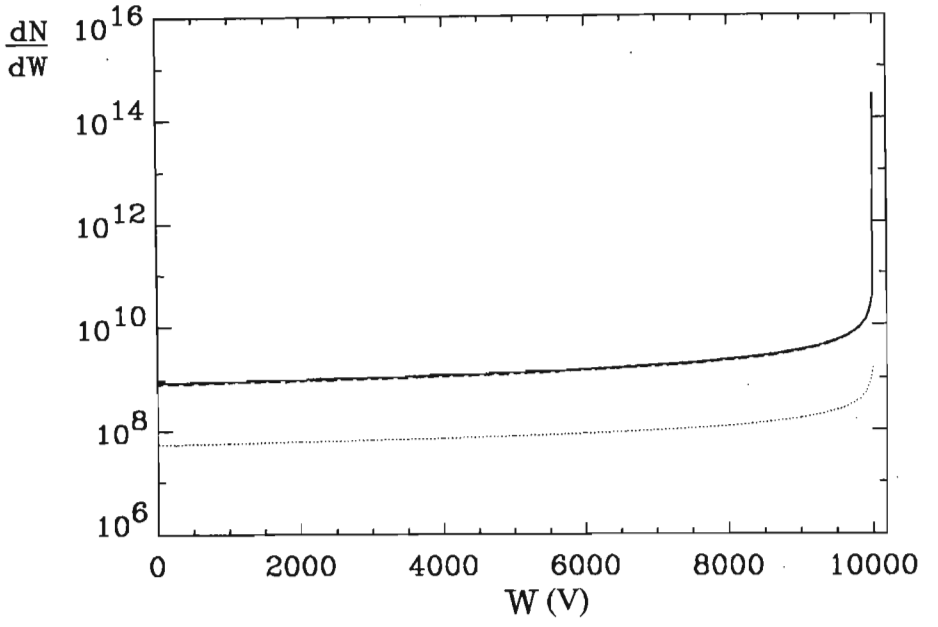

Fig. 9 Energy distribution plotted as a function of ion energy. The dotted line corresponds to the first term in (25), while the dashed line corresponds to the third term. The second term is responsible for the peak at W = 10000.

This equation can be integrated from 0 to W_{min} to find the fraction of ions implanting with energy less than W_{min}. This is useful to find the fraction of ions which produce sputtering as they have insufficient energy to be implanted. Figure 10 shows the above energy distribution numerically integrated from 0 to W_{min}, as a function of W_{min}. W_{min} varies from 0 to V_0. The upper (solid line) and lower sum (dotted line) are identical, except at $W_{min} = V_0$, where the lower sum has no value.

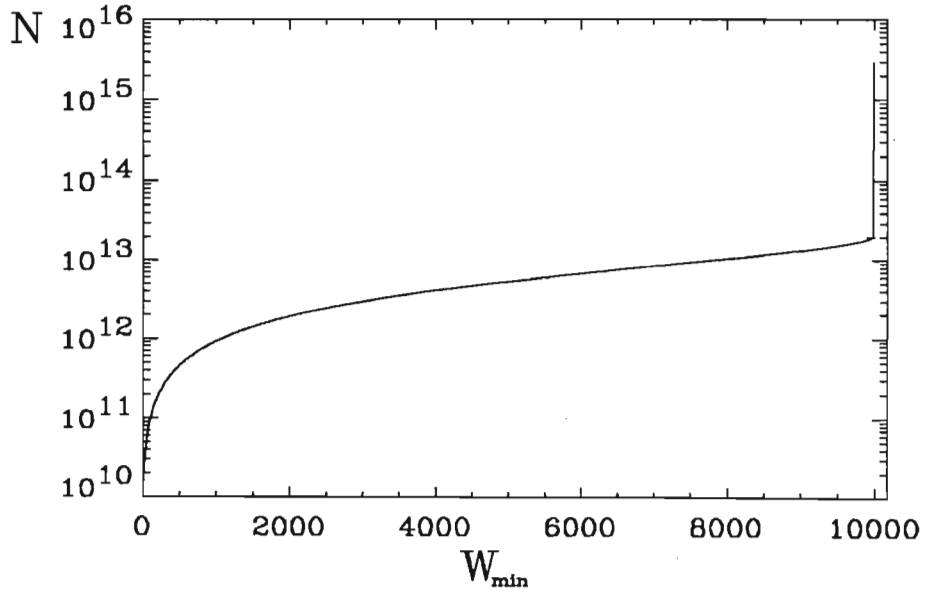

Fig. 10 The fraction of ions of energy less than W_{min} is plotted against the energy, W_{min}. The solid line represents the upper sum, while the dotted line is the lower sum. These lines are indistinguishable, except at $W_{min} = V_0$, where the lower sum has no value.

3.3.2 Stewart - Lieberman Model for a Trapezoidal Voltage Form

3.3.2.1 Voltage Profile

Stewart and Lieberman[11] later developed a model to describe the sheath evolution for voltage pulses with finite rise, plateau and fall times (Fig 11). The normalised voltage is of the form:

$$\tilde{V}(\tau)=\begin{cases}0 & \tau<0\\ \tau/\tau_r & 0\le\tau\le\tau_r\\ 1 & \tau_r\le\tau\le\tau_r+\tau_p\\ (\tau_t-\tau)/\tau_f & \tau_r+\tau_p\le\tau\le\tau_t\end{cases} \qquad (26)$$

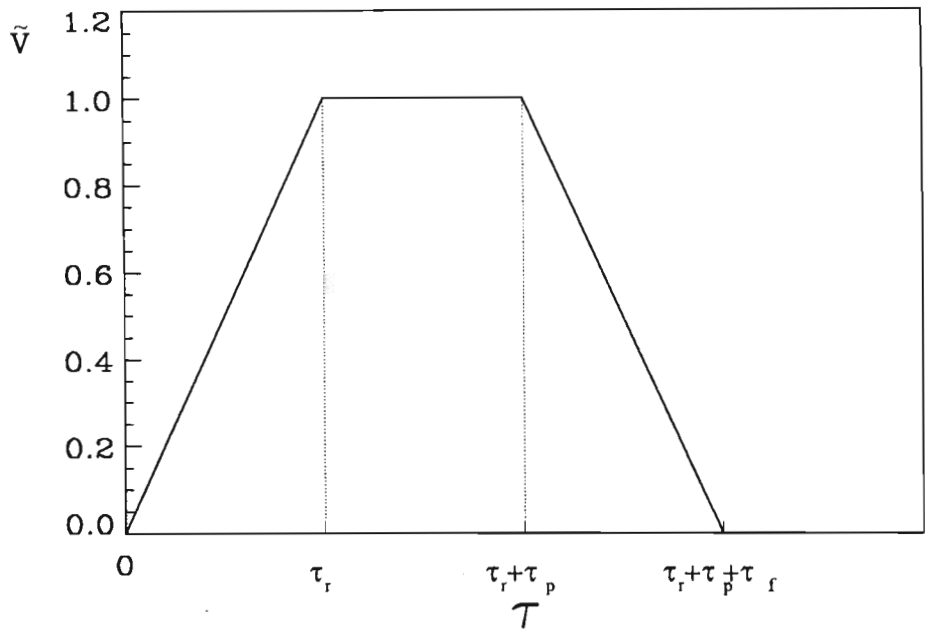

Fig. 11 The trapezoidal potential profile for the Lieberman model

3.3.2.2 Sheath Edge Motion

As for the Lieberman[9] model, the Child Law current density is equated to the sheath velocity, however, c_s is now neglected, because it is assumed that the sheath moves with a velocity much greater than the ion sound speed within the plasma. The sheath velocity equation is normalised, using the same factors as in 3.3.1, and the following equation results:

$$\frac{dS}{d\tau}=\frac{2}{9}\frac{1}{S^2}\tilde{V}^{3/2}(\tau) \qquad (27)$$

This equation may be integrated over each time period, resulting in the following set of equations.

$$S(\tau) = \left(\tfrac{4}{15}\right)^{1/3} \tau^{5/6} / \tau_r^{1/2} \qquad 0 \le \tau \le \tau_r$$

$$S(\tau) = \left(\tfrac{2}{3}\tau - \tfrac{2}{5}\tau_r\right)^{1/3} \qquad \tau_r \le \tau \le \tau_r + \tau_p$$

$$S(\tau) = \left(\tfrac{2}{3}\tau_p + \tfrac{4}{15}\left(\tau_r + \tau_f\right) - \tfrac{4}{15}\left(\tau_t - \tau\right)^{5/2} / \tau_f^{3/2}\right)^{1/3} \qquad \tau_r + \tau_p \le \tau \le \tau_t$$

(28)

It is noteworthy that at $\tau = 0$, $S = 0$, unlike in 3.2.1, where at $\tau = 0$, $S = 1$. In this model, the physical picture of the 'instantaneous' formation of the ion matrix sheath is replaced by that of a gradually expanding non-uniform sheath.

The following graphs show the normalised potential and sheath width as functions of time. The results were generated, for the experimental rise time of 2 μs ($\tau \sim 7.0$), plateau of 10 μs ($\tau \sim 35.2$) and fall time of 200 μs ($\tau \sim 703.5$). The rise time is so short that the ramp to maximum potential appears almost instantaneous. The sheath width increases sharply with the initial increase in potential, and as the potential decreases for larger τ, the sheath width expansion slows down, with the maximum sheath width at approximately 6 units ($s = 6\ s_0$).

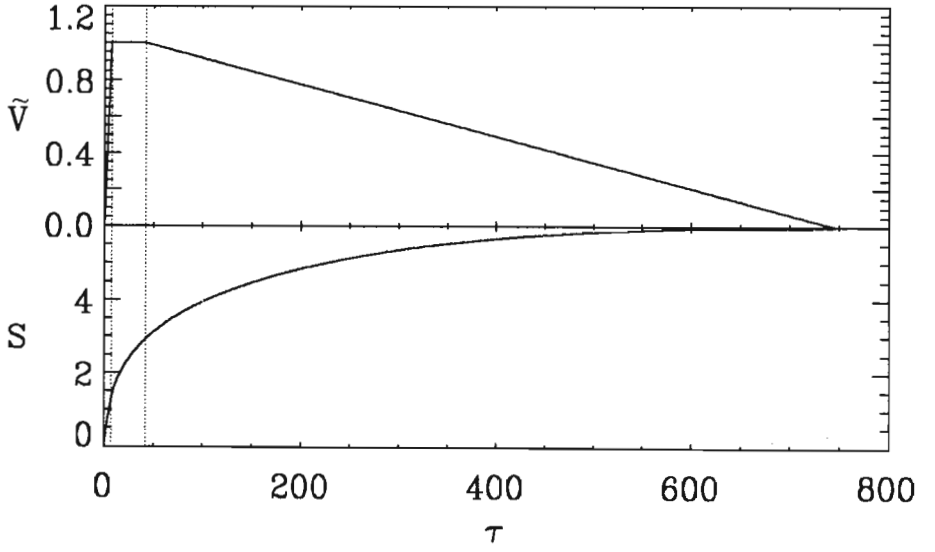

Fig 12. A plot of the sheath edge position as a function of time, showing also how the voltage changes in time.

3.3.2.3 Current Density

Next, the normalised current density $J(\tau)$ is calculated. Quasi-Static Implantation is assumed. This means that the ions are assumed to have an initial normalised position $X_0 = x_0/s_0$, which is reached by the expanding sheath edge at time τ_s. At this time the ion begins to move across the sheath, down the potential gradient. The sheath is assumed to be stationary, during the flight of the ion across the sheath. This assumption is necessary for the analytical solution of the equations, however, the author feels that it is an oversimplification of the situation. Firstly, $S(\tau)$ is set to X_0 at

$\tau = \tau_s$, so that $X_0 = S(\tau_s)$. Inverting this equation gives τ_s as a function of X_0, $\tau_s = f(X_0)$. At $\tau = \tau_s$, the ion begins its flight. The total flight time is calculated to be:

$$\tau' = \frac{3X_0}{\tilde{V}(\tau_s)} \tag{29}$$

The ion then reaches the target at time

$$\tau = \tau_s + \tau' = f(X_0) + \frac{3X_0}{\tilde{V}^{-1/2}(\tau_s)} \tag{30}$$

Now, the normalised implantation current density is given by:

$$J(\tau_s) = \frac{j(\tau_s)}{en_0u_0} = \left(\frac{d\tau(X_0)}{dX_0}\right)^{-1} \tag{31}$$

The $J(\tau_s)$ function is required to be continuous. Stewart and Lieberman chose to smooth the voltage form:

$$\tilde{V}(\tau_s) = \begin{cases} \dfrac{\tau_s/\tau_r}{\left(1+(\tau_s/\tau_r)^8\right)^{1/8}} & 0 < \tau_s < \tau_r + \frac{1}{2}\tau_p \\ \dfrac{(\tau_t - \tau_s)/\tau_f}{\left(1+((\tau_t - \tau_s)/\tau_f)^8\right)^{1/8}} & \tau_r + \frac{1}{2}\tau_p < \tau_s < \tau_t \end{cases} \tag{32}$$

This smoothing works well when the rise, plateau and fall times are of the same order, as in the voltage form in Figure 13, where $\tau_r = \tau_p = \tau_f = 70.3$, the equivalent of 20 μs.

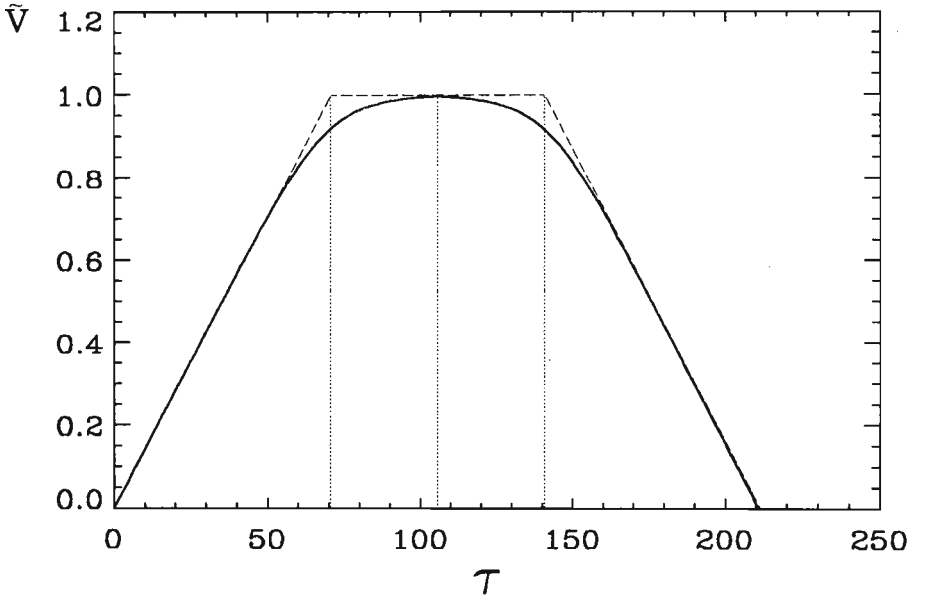

Fig. 13. The smoothed trapezoidal voltage form, with $\tau_r = \tau_p = \tau_f = 70.3$. The dotted lines are at $\tau = \tau_r, \tau_r + \tau_p/2$ and $\tau_r + \tau_p$.

It was discovered that a problem occurs when τ_r is substantially smaller than τ_f, as is the case for the Natal University experimental data. For the voltage function to be continuous at $\tau_{mid} = \tau_r + \tau_p/2$, it is necessary that $(\tau_t - \tau_{mid})/\tau_f \approx \tau_{mid}/\tau_r$, from (32). This results in the requirement that $1+\tau_p/2\tau_f \approx 1+\tau_p/2\tau_r$. For $\tau_r \ll \tau_f$, this will not occur, and the voltage function is no longer smooth (i.e. *dV/dt* is not continuous), as can be seen in Figure 14.

Using the method given by (29)-(31), with the smoothed voltage form (32), the current density is given by[11]:

$$J(\tau_s) = \left(\frac{6}{5}\frac{\tau_s}{X_0} + \frac{6}{5}\beta^{-1/2}\left(1+\beta^8\right)^{1/16} + \frac{9}{5}\beta^{15/2}\left(1+\beta^8\right)^{-15/16} \right)^{-1} \qquad 0 \le \tau_s \le \tau_r \tag{33}$$

$$J(\tau_s) = \left(\frac{9}{2}X_0^2 + 3\beta^{-1/2}\left(1+\beta^8\right)^{1/16} - \frac{27}{4}\sigma\beta^{-3/2}\left(1+\beta^8\right)^{1/16} + \frac{27}{4}\sigma\beta^{13/2}\left(1+\beta^8\right)^{-15/16} \right)^{-1} \qquad \tau_r \le \tau_s \le \tau_r + \tfrac{1}{2}\tau_p \tag{34}$$

with $\beta = \tau_s/\tau_r$, and $\sigma = X_0^3/\tau_r$. Over the second part of the voltage form,

$$J(\tau_s) = \left(\frac{9}{2}X_0^2 + 3\beta^{-1/2}\left(1+\beta^8\right)^{1/16} + \frac{27}{4}\sigma\beta^{-3/2}\left(1+\beta^8\right)^{1/16} - \frac{27}{4}\sigma\beta^{13/2}\left(1+\beta^8\right)^{-15/16} \right)^{-1} \qquad \tau_r + \tfrac{1}{2}\tau_p \le \tau_s \le \tau_p \tag{35}$$

$$J(\tau_s) = \left(\frac{9}{2}X_0^2\beta^{-3/2} + 3\beta^{-1/2}\left(1+\beta^8\right)^{-1/16} + \frac{27}{4}\sigma\beta^{-3}\left(1+\beta^8\right)^{1/16} - \frac{27}{4}\sigma\beta^{5}\left(1+\beta^8\right)^{-15/16} \right)^{-1} \qquad \tau_p \le \tau_s \le \tau_t \tag{36}$$

with $\beta = (\tau_t - \tau_s)/\tau_f$ and $\sigma = X_0^3/\tau_f$.

The Natal University experimental time periods were used to generate Figure 14: a 2 μs ($\tau_r \sim 7.0$) rise time, a 10 μs ($\tau_p \sim 35.2$) plateau and a 200 μs ($\tau_f \sim 703.5$) fall time. As predicted, the approximation (32) does not produce the desired voltage form with rounded corners. As a result, the current density is also not smooth, with discontinuities at $\tau = \tau_r$ and $\tau_r + \tau_p$.

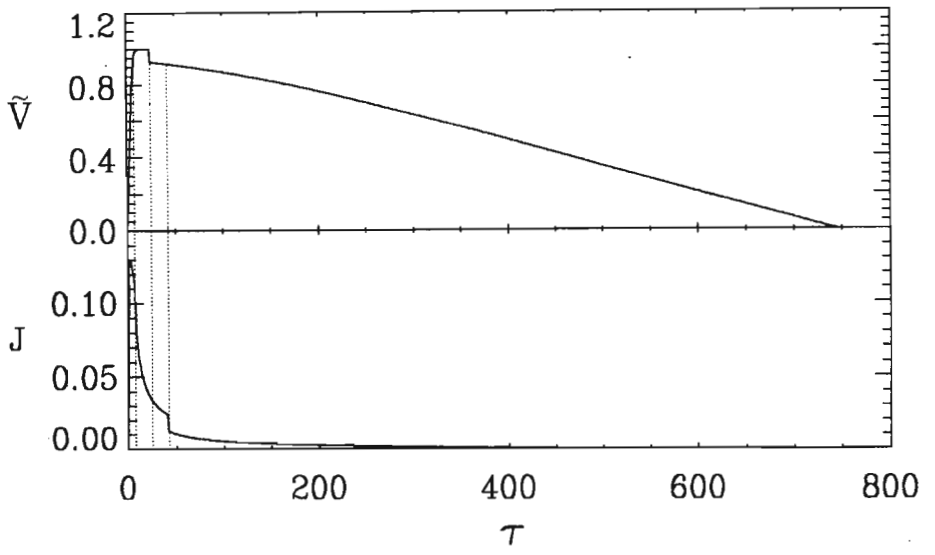

Fig 14 Normalised current density plotted as a function of normalised time. The dotted lines are at $\tau = \tau_r$, $\tau_r + \tau_p/2$ and $\tau_r + \tau_p$.

3.3.2.4 Energy Distribution

The energy distribution is calculated using the original exact trapezoidal voltage form (26), for accuracy. Since the electric field is assumed frozen at its initial value at the start of an ion's flight, the ion is assumed to implant with energy $W = V(\tau_s)$, where W is given in the units of the potential. For $0 \le \tau_s \le \tau_r$, we find that

$$W = V(\tau_s) = V_0(\tau_s/\tau_r) \tag{37}$$

This equation is rearranged, to give:

$$\tau_s = \tau_r \frac{W}{V_0} \tag{38}$$

From the current density calculation, we know that

$$S(\tau_s) = X_0 = \left(\frac{4}{15}\right)^{1/3} \frac{\tau_s^{5/6}}{\tau_r^{1/2}} \tag{39}$$

which, when rearranged gives $\tau_s = \left(\frac{15}{4}\right)^{2/5} X_0^{6/5} \tau_r^{3/5}$. This and equation (38) are combined, solving for W:

$$W = \left(\frac{15}{4}\right)^{2/5} V_0 \frac{X_0^{6/5}}{\tau_r^{-2/5}} \tag{40}$$

As with 3.3.1, there are $dN = n_0\, dx_0 = n_0\, s_0\, dX_0$ ions implanted per unit area within the energy interval $dW = \frac{6}{5}\left(\frac{15}{4}\right)^{2/5} V_0\, X_0^{1/5}\, \tau_r^{-2/5}\, dX_0$. Finally,

$$\frac{dN}{dW} = \frac{5}{6}\left(\frac{4}{15}\right)^{2/5} \frac{n_0 s_0}{V_0} X_0^{-1/5} \tau_r^{2/5} \qquad (41)$$

This may be further simplified, using (40) to:

$$\frac{dN}{dW} = \left(\frac{25}{162}\right)^{1/3} \frac{n_0 s_0 \tau_r^{1/3}}{W^{1/6} V_0^{5/6}} \qquad (42)$$

Over the plateau region, ions are implanted with full energy $W = V_0$:

$$\frac{dN}{dW} = n_0 s_0 \left(S_p - S_r\right) \delta(W - V_0) \ , \qquad (43)$$

where $\delta = 1$ throughout the plateau region, where $W = V_0$. S_r and S_p are the sheath widths at $\tau = \tau_r$ and $\tau = \tau_r + \tau_p$ respectively.

Similarly, the energy distribution for $\tau > \tau_r + \tau_p$ is:

$$\frac{dN}{dW} = -\frac{2}{9} n_0 s_0 \frac{\tau_f W^{3/2}}{V_0^{5/2}} \left(\frac{2}{3}\tau_p + \frac{4}{15}\tau_r + \frac{4}{15}\tau_f \left(1 - \frac{W}{V_0}\right)^{5/2} \right)^{-2/3} \qquad (44)$$

This part of the distribution is negative. Although the authors of the paper[11], Stewart and Lieberman do not comment on this fact, the derivation appears correct. Physically, this distribution is negative because in this time interval, the target potential, and therefore the energy of ions is decreasing, and as a result, $dW < 0$, while dN is still positive. A similar result occurs in 3.3.3.4.

The total energy distribution is the sum of the three distributions above:

$$\frac{dN}{dW} = \left(\frac{25}{162}\right)^{1/3} \frac{n_0 s_0 \tau_r^{1/3}}{W^{1/6} V_0^{5/6}} + n_0 s_0 \left(S_p - S_r\right) \delta(W - V_0)$$
$$- \frac{2}{9} n_0 s_0 \frac{\tau_f W^{3/2}}{V_0^{5/2}} \left(\frac{2}{3}\tau_p + \frac{4}{15}\tau_r + \frac{4}{15}\tau_f \left(1 - \frac{W}{V_0}\right)^{5/2} \right)^{-2/3} \qquad (45)$$

The energy distribution (44) for $\tau > \tau_r + \tau_p$ is never a dominant term in this equation, and dN/dW (45) > 0 for the whole energy range. Figure 15, shows the energy distribution, dN/dW (solid line), plotted as a function of ion energy, W. The dotted line, which is mostly indistinguishable from the solid line, corresponds to the first term. The third term, which is not shown since it is negative decreases the total value of dN/dW (solid line) infinitesimally. As with Figure 8, the second term is responsible for the peak at $W = 10000$.

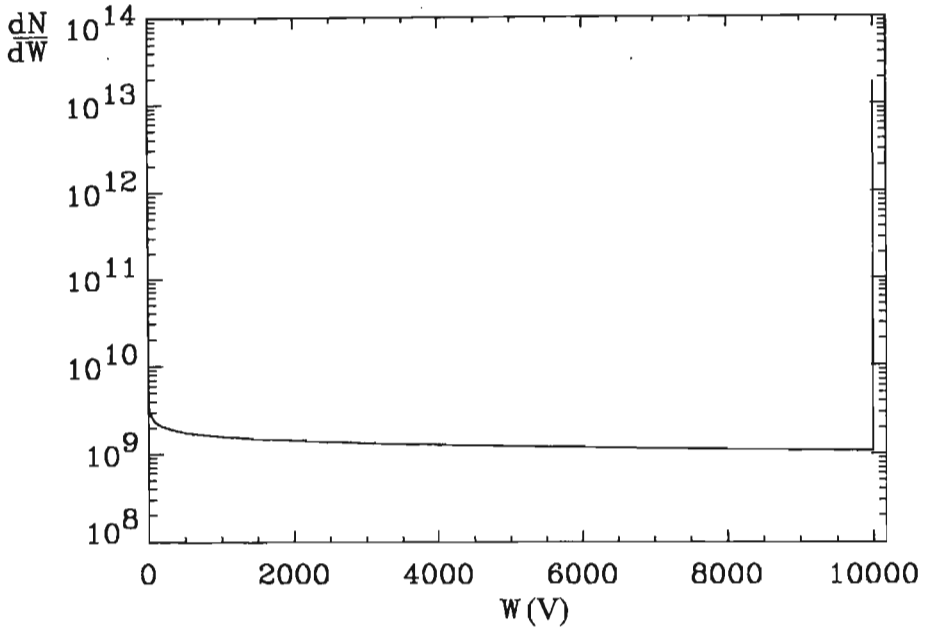

Fig 15. Energy distribution plotted as a function of incident ion energy. The first term and the total energy distribution are plotted separately, but are indistinguishable, except at $W = 10000$ V

Figure 16 shows the number of ions with energy less than W_{min}, plotted as a function of W_{min}. The upper and lower sums are again almost identical. It is worth noting that the number of ions incident at a particular energy is always positive.

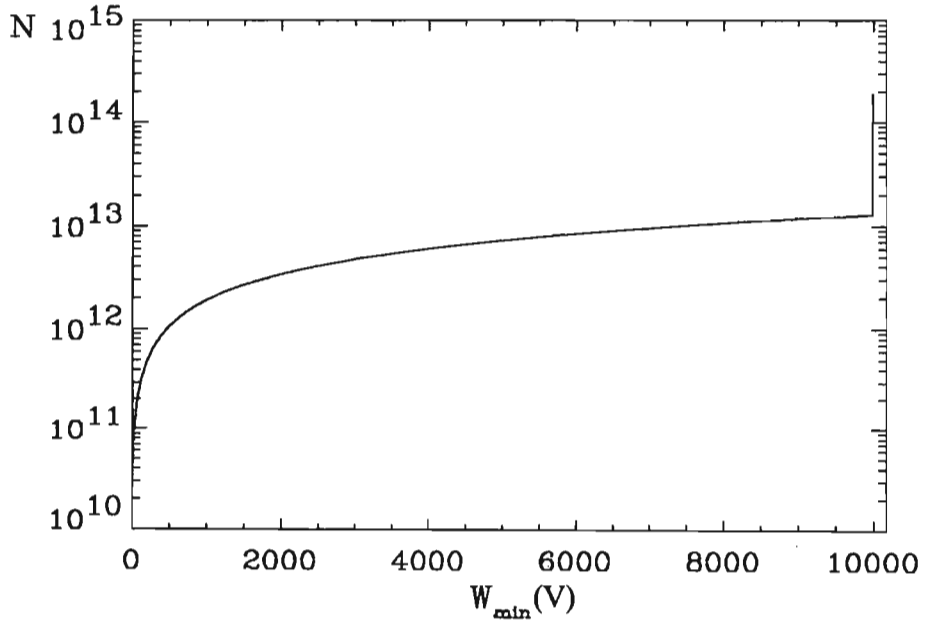

Fig 16. Number of ions incident with energy less than W_{min} plotted as a function of W_{min}. The total distribution (solid line) is virtually indistinguishable from the energy distribution generated for $\tau < \tau_r$ (dotted line).

3.3.3 Analytical Model for an Exponential Voltage Decay

3.3.3.1 Voltage Profile

Stewart and Lieberman's model has been adapted to describe a capacitative discharge which may be approximated as a wave form having a finite rise time and a short plateau, followed by an exponential decay, which closely models the Natal University experiment.

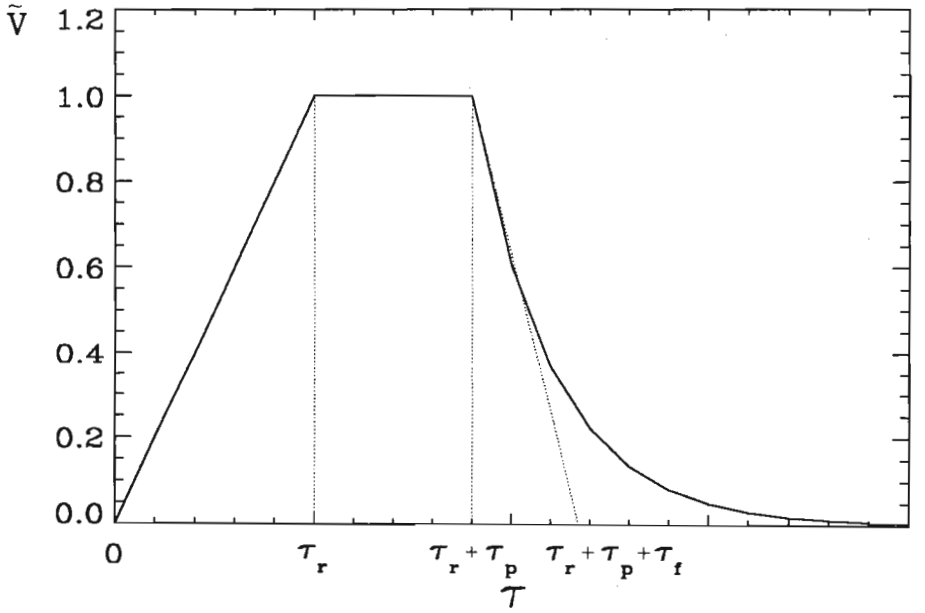

Fig. 17. The Natal University experimental voltage form.

$$\tilde{V}(\tau)=\begin{cases}0 & \tau<0\\ \tau/\tau_r & 0\le\tau\le\tau_r\\ 1 & \tau_r\le\tau\le\tau_r+\tau_p\\ \exp\left[\left(\tau_r+\tau_p-\tau\right)/\tau_f\right] & \tau_r+\tau_p\le\tau<\infty\end{cases} \qquad (46)$$

Thus, by varying the parameters, τ_r, τ_p and τ_f, the actual experimental wave form can be approximated to a reasonable degree of accuracy. The fall time, τ_f, is scaled to determine by what factor the potential decreases over a specific time period. To be consistent with a typical experimental waveform, τ_f was taken to be ~ 76.4

3.3.3.2 Sheath Edge Motion

The Child Law current density equation (5) is again equated to:

$$j_c = en_0\left(\frac{ds}{dt}+c_s\right) \qquad (47)$$

This results in the following equation:

$$\frac{ds}{dt} = \frac{4}{9}\frac{\varepsilon_0}{en_0}\left(\frac{2e}{M}\right)^{1/2}\frac{V^{3/2}}{s^2} - c_s \,, \tag{48}$$

which, when normalised, yields:

$$\frac{dS}{d\tau} = \frac{2}{9}\frac{\tilde{V}^{3/2}}{S^2} - \frac{c_s}{u_0} \tag{49}$$

Since the c_s/u_0 term is small ($\sim 10^{-3}$) in comparison to the first term ($\sim 10^{-1}$), it is reasonable to neglect it to obtain an analytical solution. A Runge-Kutta method is used in 3.3.4, for an exact numerical solution of the equation, where this term is not neglected. For large τ, the c_s/u_0 term may play a more important role in the sheath evolution, for low target voltages.

The solution of (49) is exactly the same as (28) for $0 \le \tau \le \tau_r + \tau_p$, but differs over $\tau \ge \tau_r + \tau_p$:

$$S(\tau) = \left(\tfrac{4}{15}\tau_r + \tfrac{2}{3}\tau_p + \tfrac{4}{9}\tau_f\left(1 - \exp\left[\tfrac{3}{2}\left(\tau_r + \tau_p - \tau\right)/\tau_f\right]\right)\right)^{1/3} \tag{50}$$

The sheath evolution is shown below in Figure 18, for the same rise and plateau times as in previous figures. The fall time (solid line) is given by $\tau_f \sim 76.4$. Two other decay times of $\tau_f \sim 101.8$ (dotted line) and $\tau_f \sim 61.1$ (dashed line) are also shown for comparison. The more rapidly the voltage decreases, the smaller the maximum sheath width, and the flatter the graph for $\tau > 300$.

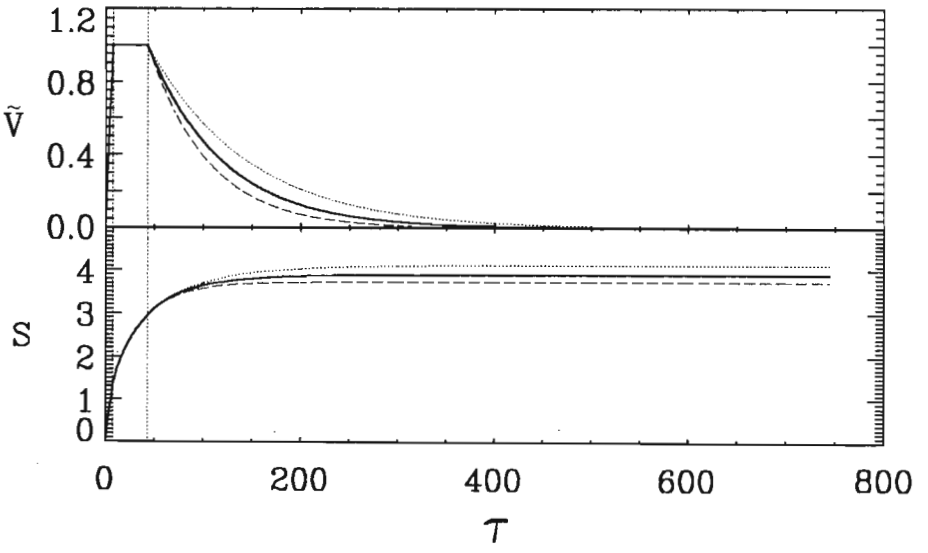

Fig. 18 A plot, showing both the potential and the sheath width as a function of time for varying τ_f. The dotted lines are at $\tau = \tau_r$ and $\tau_r + \tau_p$.

3.3.3.3 Current Density

Next, the normalised current density $J(\tau_s)$ was calculated, using a method similar to that given in the Stewart-Lieberman paper[11], except that the voltage form is not smoothed. The derivation is now described for $\tau_s > \tau_r + \tau_p$, the method being very similar for the other two time intervals. Firstly, $S(\tau)$ for $\tau_s > \tau_r + \tau_p$ is found, then X_0 is set to $S(\tau_s)$.

$$X_0 = \left(\frac{4}{15}\tau_r + \frac{2}{3}\tau_p + \frac{4}{9}\tau_f \left(1 - \exp\left[\frac{3}{2} \frac{\tau_r + \tau_p - \tau_s}{\tau_f} \right] \right) \right)^{1/3} \tag{51}$$

This equation is inverted to find τ_s as a function of X_0.

$$\tau_s = \tau_r + \tau_p - \frac{2}{3}\tau_f \ln\left[1 + \frac{\frac{3}{5}\tau_r + \frac{3}{2}\tau_p - \frac{9}{4}X_0^3}{\tau_f} \right] \tag{52}$$

At $\tau = \tau_s$, the ion begins its flight, the total flight time given by (29). For $\tau_s > \tau_r + \tau_p$,

$$\tau' = 3X_0 \exp\left[\frac{\tau_s - \tau_r - \tau_p}{2\tau_f} \right] \tag{53}$$

Now, both τ_s and τ' are differentiated with respect to X_0.

$$\frac{d\tau_s}{dX_0} = \frac{3X_0^2\tau_f}{\frac{2}{5}\tau_r + \tau_p + \frac{2}{3}\tau_f - \frac{3}{2}X_0^3} \tag{54}$$

$$\frac{d\tau'}{dX_0} = 3\left(1 + \frac{X_0}{2\tau_f}\frac{d\tau_s}{dX_0} \right) \exp\left[\frac{\tau_s - \tau_r - \tau_p}{2\tau_f} \right] \tag{55}$$

The ion, starting at X_0 reaches the target at time $\tau = \tau_s + \tau'$, with the normalised implantation current density given by (31): Now, for $0 < \tau_s < \tau_r$,

$$J(\tau_s) = \frac{5}{6}\left(\left(\frac{\tau_r}{\tau_s} \right)^{1/2} + \frac{\tau_s}{X_0} \right)^{-1} \tag{56}$$

while for $\tau_r < \tau_s < \tau_r + \tau_p$,

$$J(\tau_s) = \frac{1}{3 + \frac{9}{2}X_0^2}, \tag{57}$$

where X_0 is a function of τ_s. Lastly, for $\tau_s > \tau_r + \tau_p$,

$$J(\tau_s)=\left(3\left(1+\frac{\frac{3}{2}X_0^3}{\frac{2}{5}\tau_r+\tau_p+\frac{2}{3}\tau_f-\frac{3}{2}X_0^3}\right)\exp\left[\frac{\tau_s-\tau_r-\tau_p}{2\tau_f}\right]+\frac{3X_0^2\tau_f}{\frac{2}{5}\tau_r+\tau_p+\frac{2}{3}\tau_f-\frac{3}{2}X_0^3}\right)^{-1} \tag{58}$$

Figure 19 shows a plot of the applied voltage with different e-folding decay times (τ_f = 76.4 (solid line), 101.8 (dotted line) and 61.1 (dashed line)) together with the associated current density calculated from equations (56)-(58). As can be seen in the lower panel, there is little variation in J for the different voltage decay times. As the first derivative of the voltage form is again discontinuous, the current density plot has discontinuities at $\tau = \tau_r$ and $\tau_r + \tau_p$.

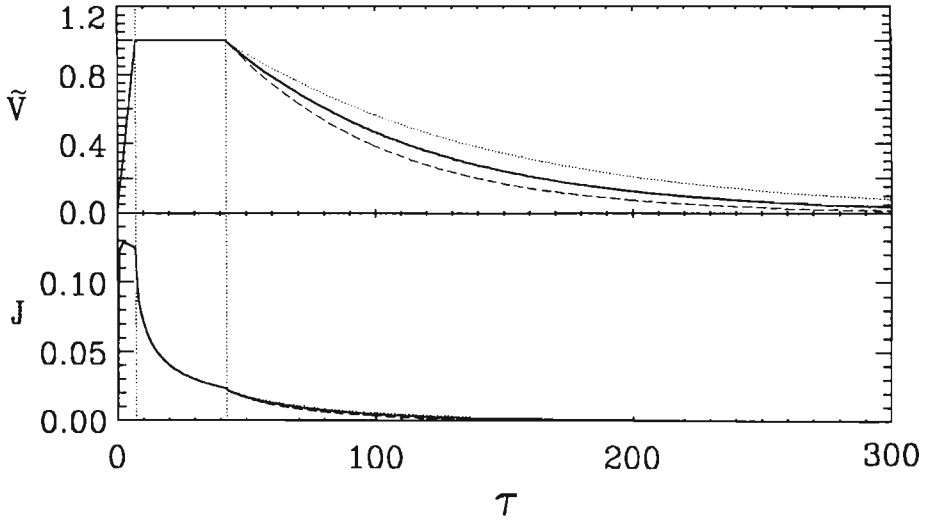

Fig. 19. A plot of voltage and current density as a function of time for different τ_f, showing discontinuities at $\tau = \tau_r$ and $\tau_r + \tau_p$.

3.3.3.4 Energy Distribution.

The energy distribution for the exponential voltage form is the same for the time periods $0 < \tau_s < \tau_r$ and $\tau_r < \tau_s < \tau_r + \tau_p$ as in 3.3.2.4 equations (43) and (44). The new energy distribution for $\tau_s > \tau_r + \tau_p$ is calculated below. Once again, the implantation energy of the ion is assumed to be $W = V(\tau_s)$, where W is given in the units of the potential. For $\tau_s > \tau_r + \tau_p$,

$$W = V(\tau_s) = V_0 \exp\left[\frac{\tau_r + \tau_p - \tau_s}{\tau_f}\right] \tag{59}$$

This equation is rearranged, to give:

$$\tau_s = \tau_r + \tau_p - \tau_f \ln\left[\frac{W}{V_0}\right] \tag{60}$$

From the current density calculation, we know (51):

$$X_0 = \left(\frac{4}{15}\tau_r + \frac{2}{3}\tau_p + \frac{4}{9}\tau_f \left(1 - \exp\left[\frac{3}{2} \frac{\tau_r + \tau_p - \tau_s}{\tau_f} \right] \right) \right)^{1/3}$$

which, when rearranged gives (52):

$$\tau_s = \tau_r + \tau_p - \frac{2}{3}\tau_f \ln\left[1 + \frac{\frac{3}{5}\tau_r + \frac{3}{2}\tau_p - \frac{9}{4}X_0^3}{\tau_f} \right]$$

Equations (60) and (52) are combined, solving for W:

$$W = V_0 \left(1 + \frac{\frac{3}{5}\tau_r + \frac{3}{2}\tau_p - \frac{9}{4}X_0^3}{\tau_f} \right)^{2/3} \qquad (61)$$

Now, there are $dN = n_0\, dx_0 = n_0\, s_0\, dX_0$ ions implanted per unit area within the energy interval

$$dW = -\frac{9}{2} V_0 \frac{X_0^2}{\tau_f} \left(1 + \frac{\frac{3}{5}\tau_r + \frac{3}{2}\tau_p - \frac{9}{4}X_0^3}{\tau_f} \right)^{-1/3} dX_0, \qquad (62)$$

so that,

$$\frac{dN}{dW} = -\frac{2}{9} \frac{n_0 s_0}{V_0 X_0^2} \tau_f \left(1 + \frac{\frac{3}{5}\tau_r + \frac{3}{2}\tau_p - \frac{9}{4}X_0^3}{\tau_f} \right)^{1/3}. \qquad (63)$$

This equation is then simplified, using (61), so that finally,

$$\frac{dN}{dW} = -\frac{2}{9} \frac{n_0 s_0}{X_0^2} \tau_f \left(\frac{W}{V_0^3} \right)^{1/2} \qquad (64)$$

Once again, this term is negative, due to the decrease of the target potential over time. Since the decrease is exponential, and therefore is more rapid than for the trapezoidal voltage form, this term plays a larger role in the total energy distribution.

To obtain the total energy distribution, equations (43), (44) and (64) are combined to give the complete energy distribution:

$$\frac{dN}{dW} = \left(\frac{25}{162} \right)^{1/3} \frac{n_0 s_0 \tau_r^{1/3}}{W^{1/6} V_0^{5/6}} + n_0 s_0 \left(S_p - S_r \right) \delta(W - V_0) - \frac{2}{9} \frac{n_0 s_0}{X_0^2} \tau_f \left(\frac{W}{V_0^3} \right)^{1/2} \qquad (65)$$

The resulting plot is shown in Figure 20. The energy distribution, dN/dW (solid line), is plotted as a function of ion energy, W. The dotted line corresponds to the first term for $0 < W < 9999$ V and the second term for $W = 10000$ V. The third term is again

negative, as the energy of the incident ions is decreasing during the exponential voltage drop. The dashed line (labelled -3) shows a plot of the absolute value of the third term. For larger W, this term dominates the others, so that dN/dW becomes negative.

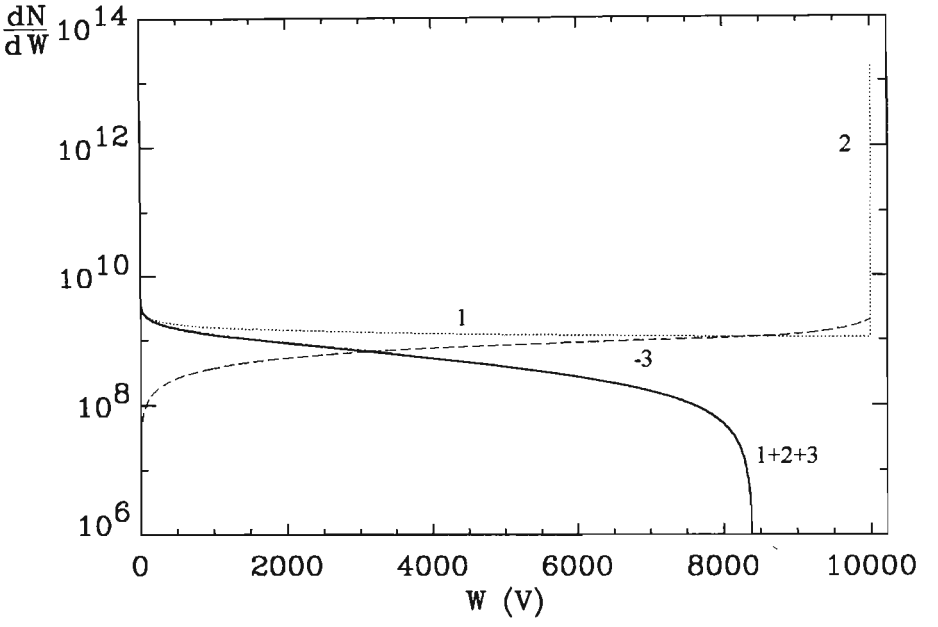

Fig. 20 A plot of the energy distribution as a function of incident ion energy. The dotted line (1) is that part of the energy distribution due to term 1. At W = 10000 V, (2) is the energy distribution due to ions incident at peak energy. The dashed line is the absolute value of the third term, while the solid line gives the sum of the three terms.

Figure 21 shows the number of ions with energy less than W_{min}, plotted as a function of W_{min}. The upper and lower sums are indistinguishable, as for 3.3.2.4.

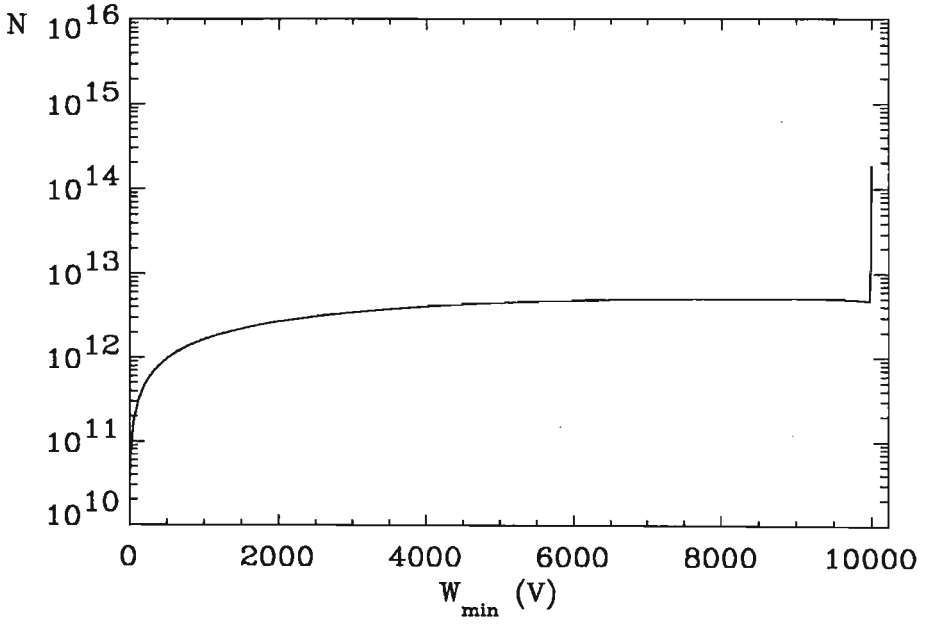

Fig. 21 The number of ions with energy less than W_{min}, plotted as a function of W_{min}.

While the energy distribution in Figure 20 does appear unlikely, when this function is integrated (Figure 21), the result is very similar to Figure 16. This would indicate that equation (65) and Figure 19 are correct.

3.3.4 Inclusion of the c_s Term in the Exponential Model

The c_s/u_0 term is neglected to obtain the analytical solution of equation (49), since it is small ($\sim 10^{-3}$) in comparison to the first term ($\sim 10^{-1}$). However, in the case of the exponential decay of 3.3.3, the target potential becomes very small ($\tilde{V} \sim 10^{-3}$), and the c_s/u_0 term dominates, so that the inclusion of this term in the solution becomes necessary. A Runge-Kutta method is used, for a numerical solution of equation (49).

3.3.4.1 Sheath Edge Position

The equation,

$$\frac{dS}{d\tau} = \frac{2}{9}\frac{\tilde{V}^{3/2}}{S^2} - \frac{c_s}{u_0} \tag{64}$$

is solved numerically, using the Runge-Kutta method. For each time interval, i, the following four terms are calculated[30]:

$$k_1 = d\tau\left(\frac{2}{9}\frac{\tilde{V}^{3/2}[\tau_i]}{S^2[i]} - \frac{c_s}{u_0}\right) \qquad k_3 = d\tau\left(\frac{2}{9}\frac{\tilde{V}^{3/2}[\tau_i + {}^{d\tau}/_2]}{\left(S[i] + {}^{k_2}/_2\right)^2} - \frac{c_s}{u_0}\right)$$

$$k_2 = d\tau\left(\frac{2}{9}\frac{\tilde{V}^{3/2}[\tau_i + {}^{d\tau}/_2]}{\left(S[i] + {}^{k_1}/_2\right)^2} - \frac{c_s}{u_0}\right) \qquad k_4 = d\tau\left(\frac{2}{9}\frac{\tilde{V}^{3/2}[\tau_i + d\tau]}{\left(S[i] + k_3\right)^2} - \frac{c_s}{u_0}\right)$$

(65)

with the sheath width in time interval i given by

$$S[i+1] = S[i] + \frac{k_1}{6} + \frac{k_2}{3} + \frac{k_3}{3} + \frac{k_4}{6} \tag{66}$$

$d\tau$ is set to 1 plasma period, and i is run through 0 to 800 for the equivalent of roughly 250 μs, depending on the specific experimental set-up. This method is very sensitive to initial conditions. $S(0)$ must be chosen very carefully, otherwise the result tends to oscillate around zero. For the following graphs, $S(0)$ is set to 0.01. For a smaller value, the value of $S(1)$ becomes very large. The size of the c_s/u_0 term also plays an important role.

In equation (64), as S becomes larger, the first term becomes smaller. At some point in time, the two terms will balance each other, so that $dS/d\tau$ tends to zero. This means that the sheath expansion slows down, allowing the sheath to reach a maximum width. As time continues and $V(\tau)$ decreases, the second term will dominate, and the sheath will move back towards the target, as its width decreases. All of this can be seen in the following graphs (Figures 22 and 23). Figure 22 shows the voltage and sheath

expansion for the trapezoidal voltage form used in Section 3.3.2. Figure 23 shows the results for the exponential decay of 3.3.3. The effect of the $c_s = \sqrt{(kT_e)/M}$ term can be seen by comparing the results for the electron temperature, T_e = 0 eV (solid line), T_e = 1 eV (dotted line) and T_e = 2 eV (dashed line) - the larger the value of c_s, the more rapidly the sheath width decreases.

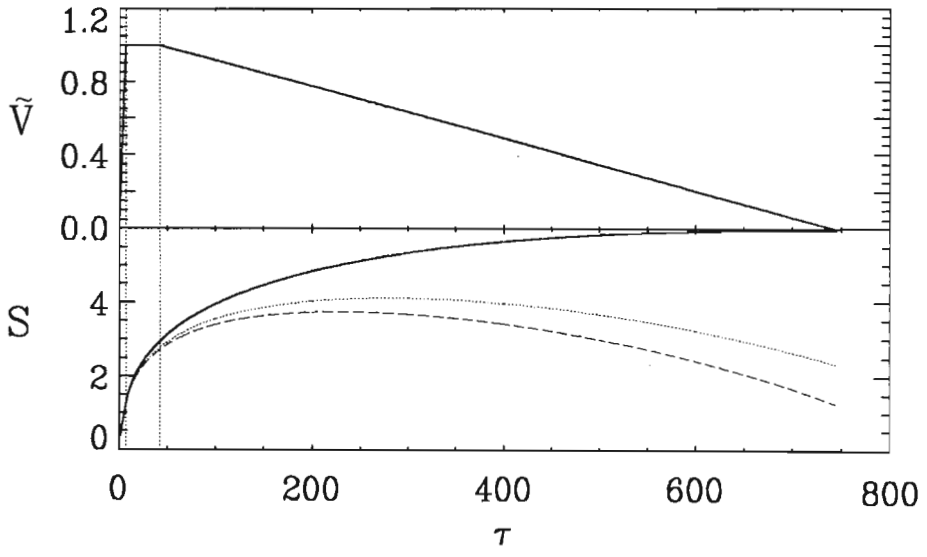

Fig. 22 Sheath width as a function of time, plotted with the trapezoidal voltage form. The solid line represents $S(\tau)$ for $T_e = 0$, the dotted line for $T_e = 1$ and the dashed line for $T_e = 2$. The vertical dotted lines mark $\tau = \tau_r$ and $\tau_r + \tau_p$.

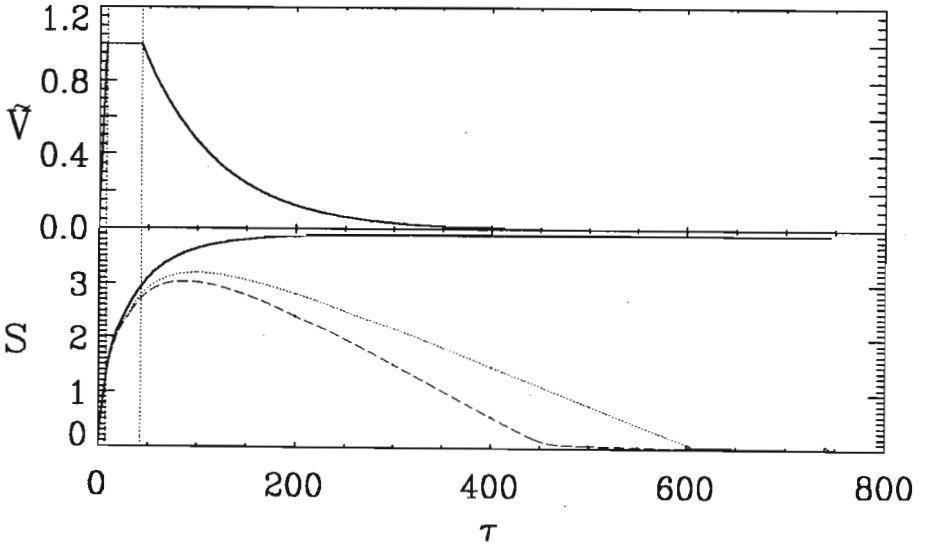

Fig. 23 Sheath width as a function of time, plotted with the exponential voltage form. The solid line represents $S(\tau)$ for $T_e = 0$, the dotted line for $T_e = 1$ and the dashed line for $T_e = 2$. The vertical dotted lines mark $\tau = \tau_r$ and $\tau_r + \tau_p$. The vertical dotted lines are again at $\tau = \tau_r$ and $\tau_r + \tau_p$.

The exponential voltage form decreases more rapidly and, as a result, so does the sheath width. As stated in Section 3.3.1, the validity of including the c_s term is still in question[3,9,11], with the argument that because the sheath edge moves out so rapidly, the presheath does not have time to form or accelerate ions to velocity c_s. The numerical simulation in 3.4, while allowing for a finite c_s term, is run for $c_s = 0$.

3.3.4.2 Current Density

The normalised current density $J(\tau)$, can also be calculated, using a method similar to the previous current density calculation. The real time variable, t is run over the required time period, with $\tau = \omega_{pi}\, t$ and $X_0(t) = S(\tau(t))$. At $\tau = \tau_S$, the ion begins its flight across the sheath. The total flight time is expressed as before, with the ion reaching the target at time

$$\tau(t) = \tau_s\ (t) + \frac{3X_0(t)}{\tilde{V}^{1/2}(\tau_s(t))} \qquad (67)$$

Now, the normalised implantation current density is given by:

$$J[\tau_s(t)] = \frac{dX_0(t)}{d\tau(t)} \qquad (68)$$

Figure 24 shows the voltage and current density for the trapezoidal voltage form used in Section 3.3.2, while Figure 25 shows similar results for the exponential decay of 3.3.3. The effect of the $c_s = \sqrt{(kT_e)/M}$ term is more marked in Figure 25, where the voltage decays more rapidly. Once again, the electron temperature is varied, with $T_e = 0$ eV (solid line), $T_e = 1$ eV (dotted line) and $T_e = 2$ eV (dashed line) - the larger the value of c_s, the more rapidly the sheath width decreases.

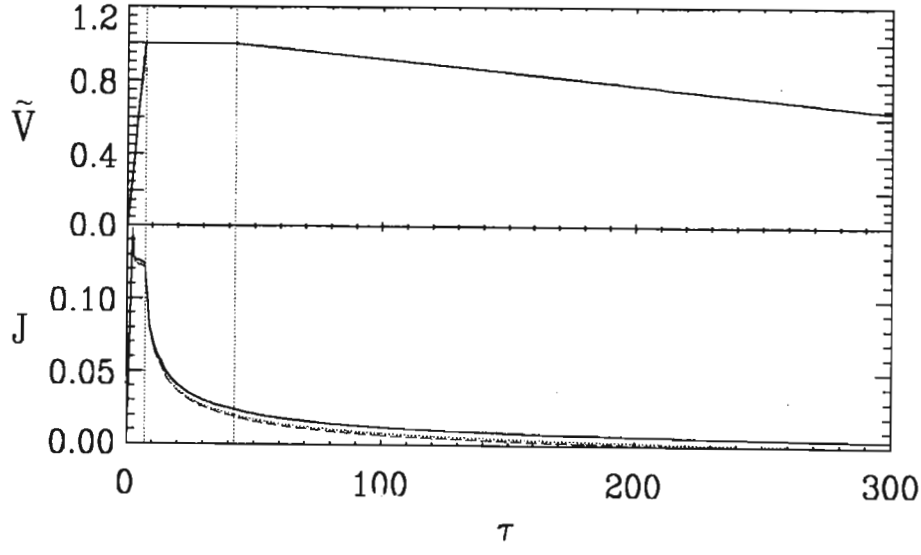

Fig. 24 Current density and potential as a function of time for the trapezoidal voltage pulse.

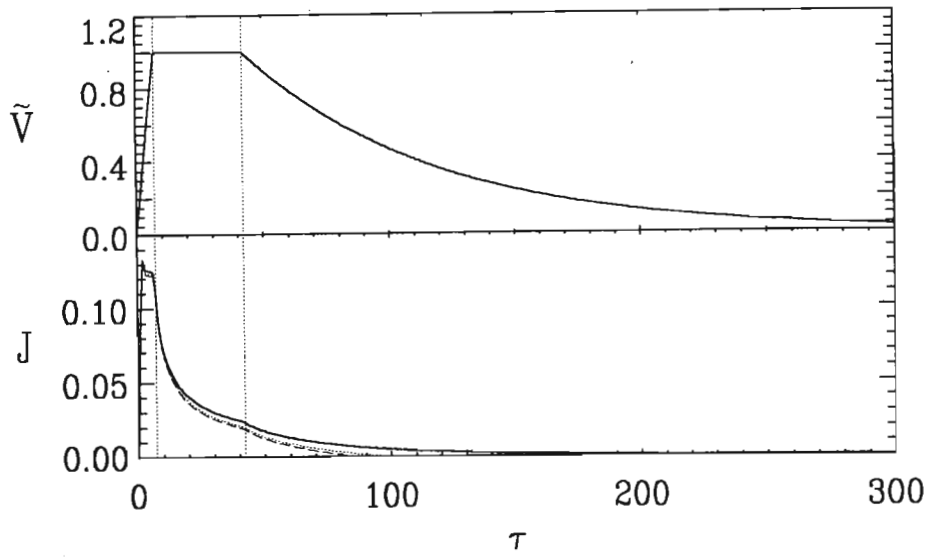

Fig. 25 Current density and potential as a function of time for the exponential voltage pulse.

The assumptions made in deriving the analytic models 3.3.2 and 3.3.3 (collisionless ion flow; inertialess electron motion; applied potential much greater than electron temperature; formation of a Quasistatic Child law sheath during the entire implantation, with the required current supplied by the uncovering of ions at the sheath edge and frozen electric field during an ion's flight across the sheath) limit the applicability of the numerical solutions obtained. For this reason, a more complete fluid model was used.

3.4 NUMERICAL MODELS

3.4.1 Introduction

Sheridan had previously developed a one dimensional fluid model[31] of the PSII process, based on a paper written by Widner *et al*[32]. This model predicts the plasma sheath potential, electric field, ion velocity, ion density, and sheath width for a negatively charged wall in contact with a plasma. Poisson's equation is solved, with the assumption that the electron density follows a Boltzmann distribution, and that the ions are cold and collisionless, with the ion density following the continuity equations and equations of motion.

This Sheridan model was adapted to include two ion fluids, since a lot of plasmas used for PSII have ions of different mass mixed together in varying ratios. In particular, a nitrogen plasma consists of two ions, the N^+ and N_2^+ ions, which occur in varying ratios, depending on gas pressure, discharge current and background gas[19]. The initial densities of each ion fluid n_{i1} (N^+) and n_{i2} (N_2^+) in a nitrogen plasma are variables and are typically in the ratio 1:3[19]. The ion fluid mass ratio is also a variable with $M_1/M_2 = 0.5$ in the result described here. Finally, to retain complete generality, an explicit charge state for each of the ions is included in 3.4.3.

3.4.2 Two ion fluids of different mass.

For the two fluid model, Poisson's equation is modified to explicitly allow for different abundances, n_{i1} and n_{i2}, of two singly charged ion species:

$$\nabla^2\phi = -\frac{e}{\varepsilon_0}\left(n_{i1}+n_{i2}-n_e\right) \tag{69}$$

The initial plasma density is then given by $n_0 = n_{i1}\big|_{t=0} + n_{i2}\big|_{t=0}$. Since the time scale of interest is that of the ion plasma period, which is much greater than the electron plasma period, $\omega_{pi}/\omega_{pe} \approx 10^4$, the electrons can be assumed to be massless. The electron density, n_e, is then given by the Boltzmann equation[29].

$$n_e = n_0 \exp\left(\frac{e\phi}{kT_e}\right) \tag{70}$$

The evolution of each species is described by the ion equations of continuity.

$$\begin{aligned}\frac{\partial n_{i1}}{\partial t}+\frac{\partial}{\partial x}\left(n_{i1}v_{i1}\right)&=0\\ \frac{\partial n_{i2}}{\partial t}+\frac{\partial}{\partial x}\left(n_{i2}v_{i2}\right)&=0\end{aligned} \tag{71}$$

and motion:

$$\begin{aligned}\frac{\partial v_{i1}}{\partial t}+v_{i1}\frac{\partial v_{i1}}{\partial x}&=-\frac{e}{M_1}\frac{\partial\phi}{\partial x}\\ \frac{\partial v_{i2}}{\partial t}+v_{i2}\frac{\partial v_{i2}}{\partial x}&=-\frac{e}{M_2}\frac{\partial\phi}{\partial x}\end{aligned} \tag{72}$$

where v_{i1} is the velocity of ion fluid 1, and v_{i2} is the velocity of ion fluid 2.

Species '1' is assumed to be the lighter species i.e. $M_1 < M_2$. Equations (69)-(72) can be rewritten using the following dimensionless variables: $\eta = -\frac{e\phi}{kT_e}$; $\xi = \frac{x}{\lambda_D}$ where the Debye length $\lambda_D = \sqrt{\frac{\varepsilon_0 kT_e}{n_0 e^2}}$; $u_1 = \frac{v_{i1}}{c_s}$ and $u_2 = \frac{v_{i2}}{c_s}$ where the ion sound speed, $c_s = \sqrt{\frac{kT_e}{M_1}}$ and $\tau = \omega_{pi}\, t$ where the ion plasma frequency, $\omega_{pi} = \sqrt{\frac{n_0 e^2}{\varepsilon_0 M_1}}$. The ion fluid densities are also normalised, with $\tilde{n}_1 = \frac{n_{i1}}{n_0}$, $\tilde{n}_2 = \frac{n_{i2}}{n_0}$ and the normalised electron density $\tilde{n}_e = \frac{n_e}{n_0}$. Since the ions are singly charged, the initial number of electrons is equal to the number of ions. Equations (70)-(72) may then be simplified to give:

$$\frac{\partial^2 \eta}{\partial \xi^2} = \tilde{n}_1 + \tilde{n}_2 - \exp(-\eta) \tag{73}$$

$$\begin{aligned} \frac{\partial \tilde{n}_1}{\partial \tau} + \frac{\partial}{\partial \xi}\left(\tilde{n}_1 u_1\right) &= 0 \\ \frac{\partial \tilde{n}_2}{\partial \tau} + \frac{\partial}{\partial \xi}\left(\tilde{n}_2 u_2\right) &= 0 \end{aligned} \tag{74}$$

$$\begin{aligned} \frac{\partial u_1}{\partial \tau} + u_1 \frac{\partial u_1}{\partial \xi} &= \frac{\partial \eta}{\partial \xi} \\ \frac{\partial u_2}{\partial \tau} + u_2 \frac{\partial u_2}{\partial \xi} &= \frac{M_1}{M_2} \frac{\partial \eta}{\partial \xi} \end{aligned} \tag{75}$$

3.4.3 Two ion fluids of different mass and charge

The possibility of a charge state other than unity may be explicitly included in equations (69)-(72). This will allow for the modelling of envisaged complex gas mixtures. Poisson's equation for two ion species is now given by:

$$\nabla^2 \phi = -\frac{e}{\varepsilon_0}\left(q_1 n_{i1} + q_2 n_{i2} - n_e\right) \tag{76}$$

where q_1 and q_2 are the charge states of the two respective ion species. For example, doubly charged N^{2+} will have $q_1 = 2$. The initial plasma density is again given by $n_0 = n_{i1}\big|_{t=0} + n_{i2}\big|_{t=0}$. The electron density, n_e, is given by a modified Boltzmann equation:

$$n_e = \left(q_1 n_{i1} + q_2 n_{i2}\right) \exp\left(\frac{e\phi}{kT_e}\right) \tag{77}$$

The equations of continuity remain unchanged:

$$\begin{aligned} \frac{\partial n_{i1}}{\partial t} + \frac{\partial}{\partial x}\left(n_{i1} v_{i1}\right) &= 0 \\ \frac{\partial n_{i2}}{\partial t} + \frac{\partial}{\partial x}\left(n_{i2} v_{i2}\right) &= 0 \end{aligned} \tag{78}$$

The equations of motion are modified:

$$\frac{\partial v_{i1}}{\partial t} + v_{i1}\frac{\partial v_{i1}}{\partial x} = -\frac{q_1 e}{M_1}\frac{\partial \phi}{\partial x}$$
$$\frac{\partial v_{i2}}{\partial t} + v_{i2}\frac{\partial v_{i2}}{\partial x} = -\frac{q_2 e}{M_2}\frac{\partial \phi}{\partial x} \qquad (79)$$

The equations are again normalised, using dimensionless variables, which are defined relative to the mass and charge of species '1': $\lambda_D = \sqrt{\frac{\varepsilon_0 k T_e}{n_0 q_1 e^2}}$; $c_s = \sqrt{\frac{q_1 k T_e}{M_1}}$ and $\omega_{pi} = \sqrt{\frac{n_0 q_1^2 e^2}{\varepsilon_0 M_1}}$. The ion and electron densities are all normalised relative to the initial density, n_0, so that $\tilde{n}_e = (q_1 \tilde{n}_1 + q_2 \tilde{n}_2)\exp(-\eta)$ and, initially, $\tilde{n}_1 + \tilde{n}_2 = 1$. With these normalisations, equations (76)-(79) become:

$$\frac{\partial^2 \eta}{\partial \xi^2} = \left(\tilde{n}_1 + \frac{q_1}{q_2}\tilde{n}_2\right)(1 - \exp(-\eta)) \qquad (80)$$

$$\frac{\partial \tilde{n}_1}{\partial \tau} + \frac{\partial}{\partial \xi}(\tilde{n}_1 u_1) = 0$$
$$\frac{\partial \tilde{n}_2}{\partial \tau} + \frac{\partial}{\partial \xi}(\tilde{n}_2 u_2) = 0 \qquad (81)$$

$$\frac{\partial u_1}{\partial \tau} + u_1\frac{\partial u_1}{\partial \xi} = \frac{\partial \eta}{\partial \xi}$$
$$\frac{\partial u_2}{\partial \tau} + u_2\frac{\partial u_2}{\partial \xi} = \left(\frac{q_2 M_1}{q_1 M_2}\right)\frac{\partial \eta}{\partial \xi} \qquad (82)$$

The expression for the ion matrix sheath width also changes :

$$s_0 = \left(\frac{2\varepsilon_0 V}{(q_1 \tilde{n}_1 + q_2 \tilde{n}_2) e n_0}\right)^{1/2} \qquad (83)$$

As a result, the ion matrix sheath width decreases by $\sqrt{2}$ for doubly ionised atoms.

3.4.4 Numerical Solution of Fluid Equations

The fluid equations (73)-(75) or (80)-(82) were solved numerically using finite differences based on an earlier single fluid, single charge program written by Sheridan[31] originally in BASIC. This program was translated into C, and modified for two fluids. Figure 26 shows a flow chart of the program, PLANAR1.C, used to obtain the numerical solution to the fluid equations. The program sequence with steps numbered 1-10 is shown on the left hand side of Figure 26, with individual routines shown in

bold face. Details including a description of the program variables and algorithms are shown in boxes on the right hand side.

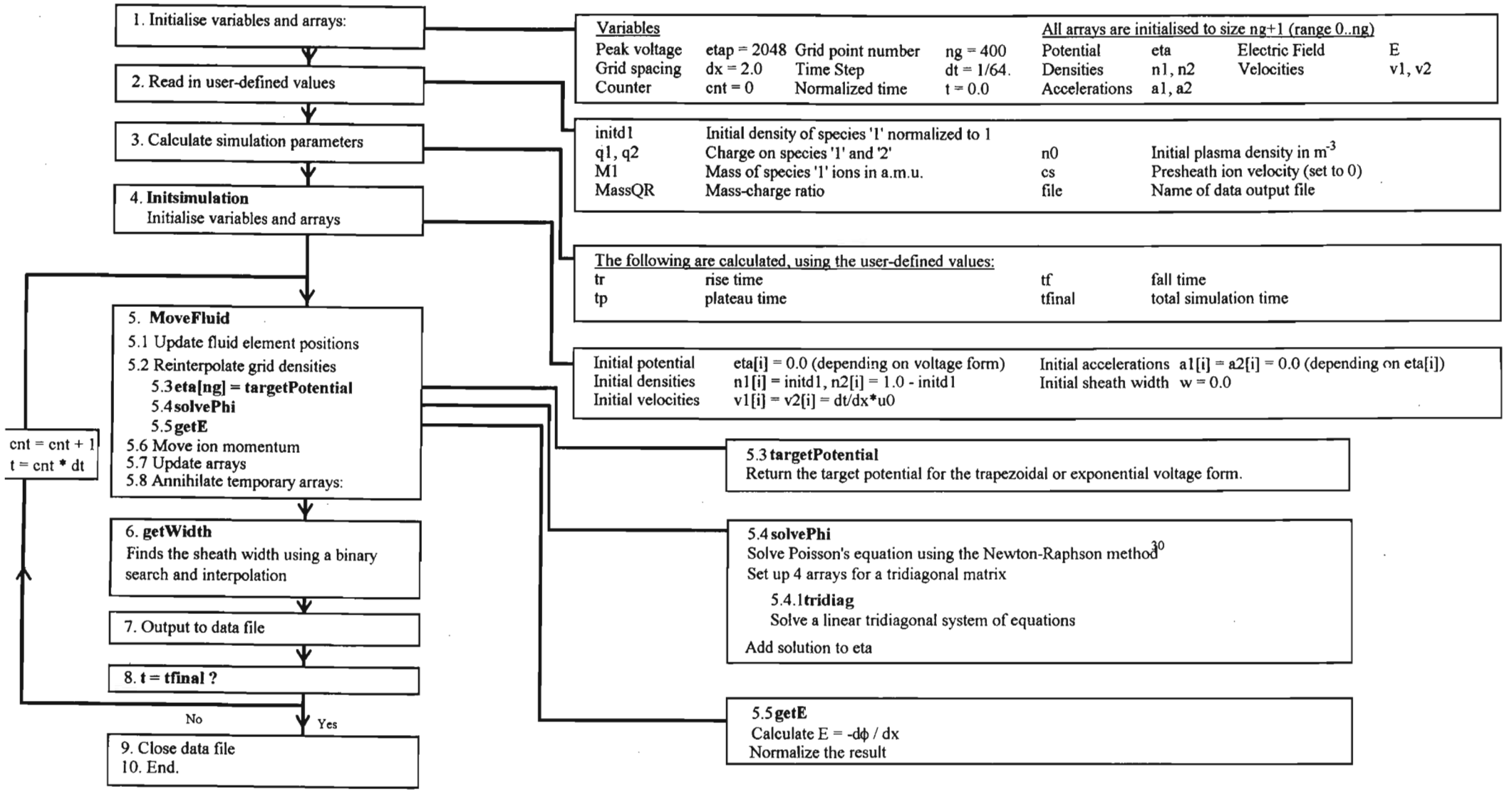

Fig. 26 Flow chart of PLANAR1.C

3.4.5 Description of PLANAR1.C program

The PLANAR1.C program flow chart may be used for the solution of equations (73)-(75), with minor modifications necessary to solve equations (80)-(82). The program is stored on stiffy in Appendix C.

It was felt that some aspects of the program should be described in greater detail. The numbering of the following paragraphs corresponds to the flow chart numbering.

1. The specific values of the variables are significant here. A peak voltage of 2048 means that the maximum possible ion velocity for the lighter ions (mass set to 1) is $v_{max} = \sqrt{2 \times 2048} = 64$, derived from $\phi = \frac{1}{2} m v^2$. Next, the grid spacing and time step must be chosen so that a fluid element will be unable to travel a distance greater than one grid spacing in one time step (the Courant condition). This means that (v.dt) must be less than dx at all times, so that for dx = 2, dt < 1/32, and is generally set to 1/40 or 1/64. If the charge, q, on a species is greater than unity, then $v_{max} = \sqrt{2.q.2048} = 64\sqrt{q}$. As a result, dt must be made smaller to satisfy the Courant condition.

The **Movefluid** procedure (5) is the main procedure that calls up a number of sub-procedures, as well as performing some routines, which are explained in greater detail below.

The first part of the procedure (5.1) updates the fluid element positions. Firstly, 2 arrays of fluid positions, x1[0..ng], x2[0..ng] are set up. In a time step dt, the fluid elements at position i will move to a new position determined by its initial velocity and acceleration, described by the equation: $x = x_0 + v_0 \Delta t + \frac{1}{2} a \Delta t^2$. Since velocity is multiplied by dt/dx, and Electric field which translates into acceleration (see later) is multiplied by $dt^2/2dx$, this equation is simplified to:

$$x1[i] = i + v1[i] + a1[i]$$
$$x2[i] = i + v2[i] + MassQR * a2[i] \qquad i = 0..ng \qquad (84)$$

for ion fluid 1 and 2. The inclusion of MassQR follows from equations (75) and (82).

Next, (5.2) the ion fluid densities are reinterpolated to the grid. The procedure for reinterpolating the density to the grid is best explained with the use of an example. Consider a species 1 fluid element at grid point i = 10 at time $t = t_1$. At this time, the fluid element represents the total density n1 = n1[10], at that point. At time $t = t_1 + dt$, its position is calculated using (84) and this fluid element moves to x[10] = 10.7, as a result of its acceleration and velocity calculated at x[10].

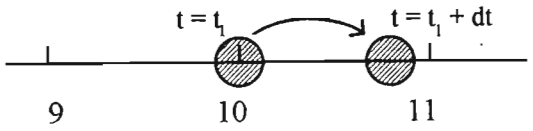

Now, a proportional part of the original density, n1[10], is interpolated to grid point j = 10, and part to grid point j+1 = 11, depending on its linear distance from these two points. Thus, the new density at grid point 10 from the fluid element initially at 10 is given by:

$$\text{newn1}[10] = \text{n1}[10]*(11-10.7) \tag{85}$$

and the new density at grid point 11 is given by:

$$\text{newn1}[11] = \text{n1}[10]*(10.7-10) \tag{86}$$

The larger portion of the density is thus allocated to the closer grid point. This process is used to reinterpolate the density of each species on the grid for each time step.

Next, (5.3) the **targetPotential** function is called, and returns the potential at the wall at time t, depending on the voltage form used.

With the potential, eta[], set, the **solvePhi** (5.4) procedure is then called. The **solvePhi** procedure solves Poisson's equation iteratively, using the Newton Raphson[30] method. This method involves the setting up of a tridiagonal matrix of ng x ng elements derived as follows. Firstly, Poisson's equation (73):

$$\frac{d^2\eta}{d\xi^2} = \tilde{n}_1 + \tilde{n}_2 - \exp(-\eta)$$

is rearranged:

$$\begin{aligned} \frac{\eta_{i-1} - 2\eta_i + \eta_{i+1}}{\Delta\xi^2} &\cong \tilde{n}_{1i} + \tilde{n}_{2i} - \exp(-\eta_i) \\ \eta_{i-1} - 2\eta_i + \eta_{i+1} &\cong \Delta\xi^2\left(\tilde{n}_{1i} + \tilde{n}_{2i} - \exp(-\eta_i)\right) \end{aligned} \tag{93}$$

The right hand side of the equation is now brought over, making:

$$0 = f_i = \eta_{i-1} - 2\eta_i + \eta_{i+1} - \Delta\xi^2\left(\tilde{n}_{1i} + \tilde{n}_{2i} - \exp(-\eta_i)\right) \tag{94}$$

Since f_i is equal to zero for all i, it is reasonable to state that:

$$\begin{bmatrix} df_1/d\eta_1 & df_1/d\eta_2 & 0 & . & 0 \\ df_1/d\eta_0 & . & . & 0 & . \\ 0 & . & . & . & 0 \\ . & 0 & . & . & df_{ng}/d\eta_{ng+1} \\ 0 & . & 0 & df_{ng}/d\eta_{ng-1} & df_{ng}/d\eta_{ng} \end{bmatrix} \times \begin{bmatrix} f_1 \\ . \\ . \\ . \\ f_{ng} \end{bmatrix} = \begin{bmatrix} 0 \\ . \\ . \\ . \\ 0 \end{bmatrix}$$

(95)

Now, the lower elements of the tridiagonal array are given by:

$$\frac{df_i}{d\eta_{i-1}} = 1 \qquad (96)$$

The middle elements by:

$$\frac{df_i}{d\eta_i} = -2 - \Delta\xi^2 \exp(-\eta_i) \qquad (97)$$

and the upper elements by:

$$\frac{df_i}{d\eta_{i+1}} = 1 \qquad (98)$$

The right hand side is set to:

$$rhs_i = \eta_{i-1} - 2\eta_i + \eta_{i+1} - \Delta\xi^2\left(\tilde{n}_{1i} + \tilde{n}_{2i} - \exp(-\eta_i)\right) \qquad (99)$$

Four arrays of size ng are set up: below, ondiag, above and rhs. Below, ondiag and above form the ng x ng tridiagonal matrix, and rhs is the right hand side of the equation. Procedure **tridiag** (5.4.1) is then called to solve (95). The method used is found in a number of references, for example, *Numerical Recipes*[30]. The solution of (95) is then added to eta.

Next, **MoveFluid** calls the **getE** (5.5) procedure. In this procedure, the electric field is found by differentiating the potential, eta, using second order finite differences.

$$E_i = \frac{\eta_{i+1} - \eta_{i-1}}{2d\xi}, \qquad (104)$$

or, E[i] = (eta[i+1] - eta[i-1]) /2 /dx. The counter, i, is run through i to ng-1, with E_0 = 0.0 and:

$$E_{ng} = \frac{\eta_{ng-2} - 4\eta_{ng-1} + 3\eta_{ng}}{2d\xi}, \qquad (105)$$

or, E[ng] = (eta[ng-2] - 4*eta[ng-1] + 3*eta[ng]) /2 /dx. The array, E, is then multiplied by a normalising factor $dt^2/2dx$.

Next, **Movefluid** moves the ion momentum, using a method very similar to 5.1. The new momentum for each ion fluid,

$$p = n1[i]*(v1[i]+a1[i]+E[i])$$
$$p = n2[i]*(v2[i]+a2[i]+MassQR*E[i]) \qquad (105)$$

is interpolated to the grid, to find the momentum of a fluid element at grid point i, using the same method as 5.2.

Finally, the arrays are updated (5.7), and temporary arrays are annihilated, to free memory space.

The **getWidth** procedure (7) is then called to calculate the sheath width, using a binary search and interpolation to find the grid point at which the electron density has fallen by a factor of two. Two integer variables, left and right are set to 0 and ng respectively. A loop is run, until (right - left) is no longer greater than 1. A variable, mid is calculated by:

$$mid = (left + right) / 2 \qquad (110)$$

If the potential eta[mid] is greater than ln(2), right is set to the value of mid, otherwise, left is set to mid. The two variables approach each other, and the loop ends at the point at which eta[left] ≈ ln(2) ≈ eta[right]. The sheath width is then given by:

$$w = d\xi * \left(ng - \left(left + \frac{(right - left) * (eta[left] - \ln 2)}{eta[left] - eta[right]} \right) \right) \qquad (111)$$

3.4.6 Typical plots

The following plots are for the same experimental values, using a trapezoidal voltage pulse. The sheath width form is quite different to the typical forms obtained previously in the analytical results, as it increases to a much larger value as τ becomes large. One reason for this is the choice of definition of the sheath edge as that point where the electron density, $\tilde{n}_e$ = exp(-η), decreases by a factor of 2. There are a number of other possible criteria for defining the sheath edge, for example, where the ion velocity becomes less than the ion sound speed, or where the ion density reaches some cut off value. In 3.2.2, equations (1)-(3), the initial ion matrix sheath width is set at the point at which $E = \phi = 0$. The two Lieberman models use this sheath width as the normalising factor, and, as a result, the calculated sheath widths are based on the $E = \phi = 0$ criterion. It should be pointed out that, experimentally, care should be taken in using the decrease in electron density as the sole criterion in identifying the sheath edge, since a rarefaction in the plasma would produce the same effect.

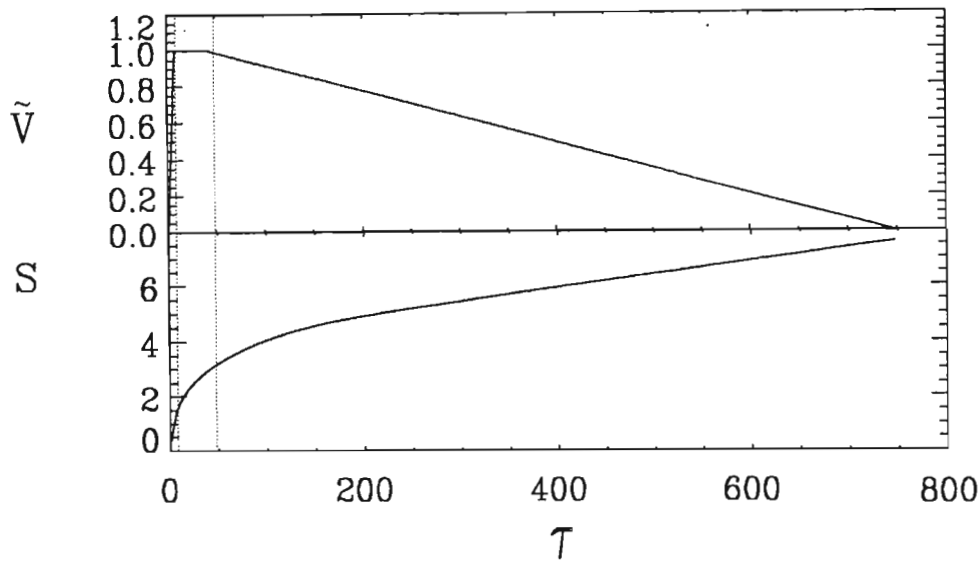

Fig. 27 Sheath evolution in time, shown with the potential form.

A plot of the temporal evolution of the current density and potential follows:

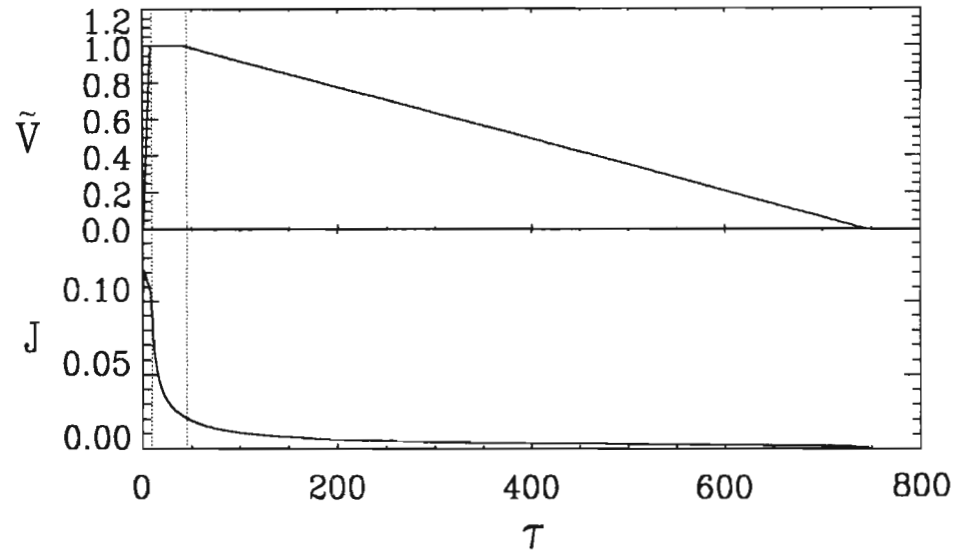

Fig. 28 Current density plotted as a function of time, with the trapezoidal voltage form from the Stewart-Lieberman[11] paper.

Next, the program was run, with procedure **targetPotential** set up for an exponential voltage decay. Once again, the predicted sheath width is much greater than the analytical models.

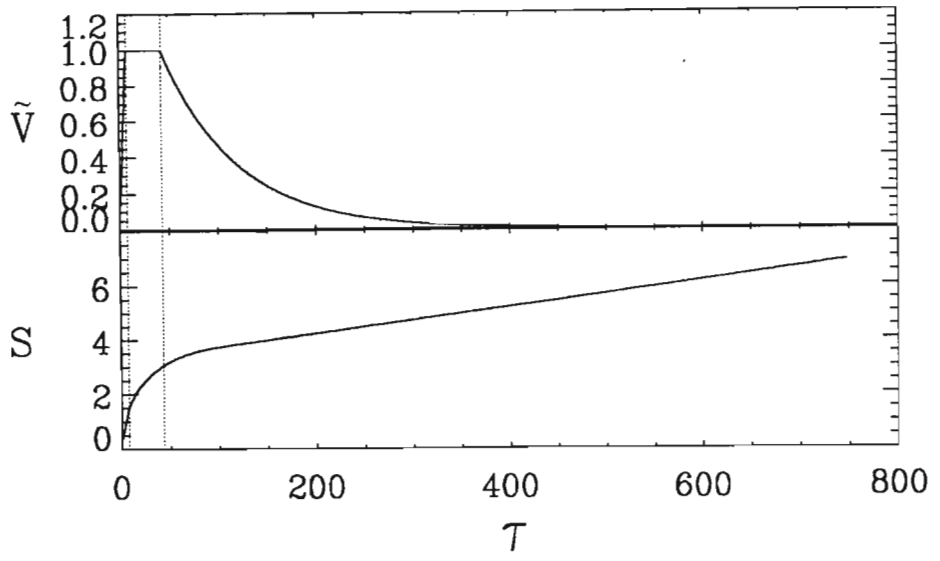

Fig. 29 Sheath evolution in time, shown with the exponentially decaying potential form.

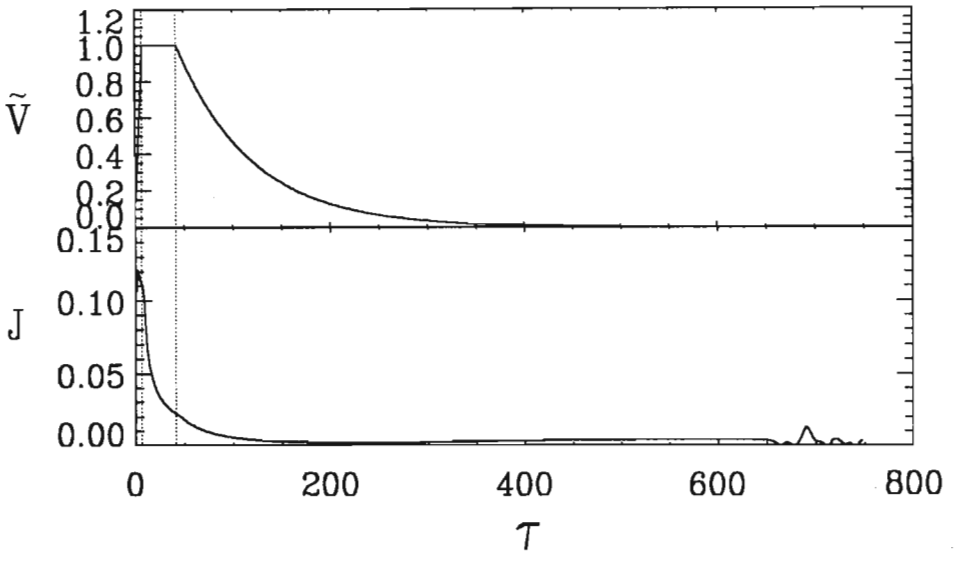

Fig. 30 Current density plotted as a function of time, with the exponential voltage form.

3.5 THE TAMIX PROGRAM

TAMIX[33,34] (Transport And MIXing from ion irradiation), is a program written by Seunghee H. Han, a Ph.D. student at the Dept. of Nuclear Engineering and Engineering Physics at the University of Wisconsin-Madison. It is used to model the motion of energetic ions striking and penetrating into a substrate, which may be metallic. For the experiment at Natal University, TAMIX was used to predict implantation depth for a specific ion current density and energy, generated by the models 3.3.3 and 3.4.

TAMIX is a highly optimised Monte Carlo program, making use of vectorization and the variance reduction scheme[33], which was achieved by the use of importance sampling (splitting and Russian Roulette). For vectorization, TAMIX uses an 'event-

based' algorithm[33], to follow a bundle of particles at a time, unlike the conventional 'history-based' method. TAMIX also incorporates some of the diffusional processes, to take into account the temperature-dependent behaviour of the target during irradiation. However, due to the uncertainties of the exact diffusion mechanism, and involved parameters, a simple diffusion model is used.

TAMIX was originally written in Cray FORTRAN, and was later translated by Jake Blanchard (University of Wisconsin-Madison) to FORTRAN-77. Unfortunately, something was lost in the translation, and thus far, it has been impossible to get TAMIX to run in the collisional-diffusional-dynamic mode. The other two modes, however, do work. These are the static and the collisional-dynamic modes.

TAMIX can be run in three modes: the static, collisional-dynamic or collisional-diffusional-dynamic modes, each of which is appropriate to a specific situation. In the static mode, the target is assumed to remain in its initial state, while in the collisional-dynamic mode, the dynamic response of the target due to the collisional processes induced by ion irradiation are simulated. In the collisional-diffusional-dynamic mode, the temperature-dependent diffusional processes are taken into account, in addition to the collisional features. Total ion fluence and target temperature determine the appropriate running mode.

3.5.1 The Static Mode.

In the static mode, the modification of the target due to bombarding ions is neglected. As a result, static mode is only suitable for low ion fluences, typically under 10^{16} ions.cm^{-2}, where the implanted ion concentration is quite low compared to that of the target atom, so that the target can be assumed to remain in its initial state. The target temperature must also remain low for the static mode to be applicable.

3.5.2 The Collisional-Dynamic Mode.

The collisional-dynamic mode only considers collisional processes. Preferential sputtering, altered layer formation, collisional mixing and rearrangement of the target composition profiles can be studied as a function of ion fluence. This mode is suitable for high ion fluences and low temperatures. The target is substantially modified, with implanted ions being incorporated as one of the target species for ion implanting later. The low temperature of the target prevents any diffusional process, which are neglected.

3.5.3 The Collisional-Diffusional-Dynamic Mode.

The collisional-diffusional-dynamic mode is suitable for high ion fluences and high target temperatures, where diffusional processes will occur. These include surface segregation, radiation enhanced diffusion, and radiation induced segregation. The latter two processes are taken into account by TAMIX by coupling the partial fluxes between point defects and atomic species.

3.5.4 Running TAMIX

A copy of the TAMIX source files and other related files are included in Appendix C. To run TAMIX on the SUN, the user must first sets up an input file, which determines the properties of the surface and the ions, for a specific situation. The input file is made up of a Master block, an Ion block, a Target block and a Compound block. (The input file must also contain a Diffusion block and Switch block, if the program is to run in the collisional-diffusional-dynamic mode, which unfortunately does not work, at present.)

TAMIX was used to simulate ion implantation into type 304 stainless steel, used for the Natal University experiment, which consists of:

Species	Fe	Cr	Ni	Mn	Si	C	P	S
Mass No.	26	24	28	25	14	12	15	16
Typical %	70.7	18.3	9.3	1.2	0.5	0.025	0.021	0.017

Table 1. Species making up type 304 stainless steel.

TAMIX limits the number of atomic species to 4, so that only Fe, Cr, Ni and Mn are used in the model. This does not significantly affect the simulation results. See Appendix A for further details on the input file, and running of the program.

CHAPTER 4

RESULTS

While this thesis is predominantly theoretical, the PSII simulation parameters were chosen to be consistent with preliminary experimental data, which was generated by Dr M.J. Alport at Natal University.

4. 1 EXPERIMENTAL ARRANGEMENT

The experimental data were obtained from a cylindrical filament discharge device[35], with a diameter of 39 cm and a length of 60 cm. The device was at a neutral pressure of 10^{-4} Torr. The target was a circular, 4 cm diameter, type 304 stainless steel plate, which was pulsed at 2 Hz to a peak potential of $V_0 \sim -8\,\mathrm{kV}$ with a rise time of $\sim 2\ \mu\mathrm{s}$ and a decay time of ~ 3 ms (Figure 31).

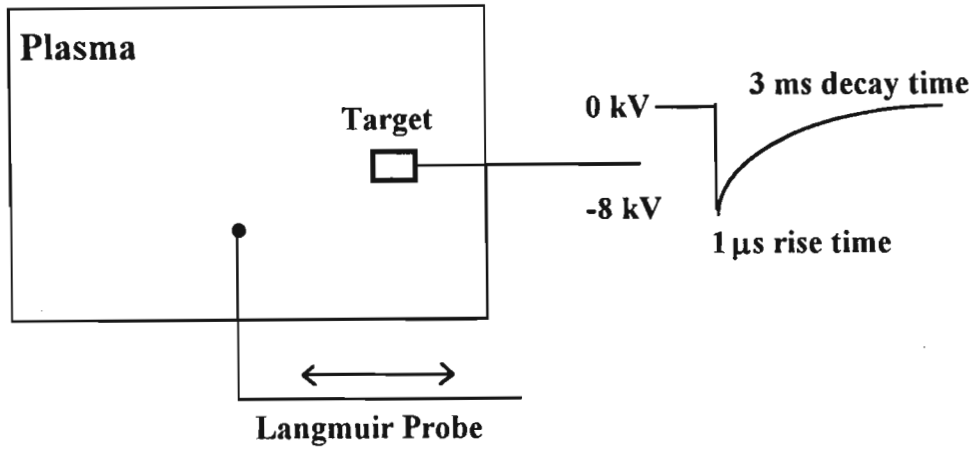

Fig. 31 The PSII experimental set-up.

The sheath edge position was measured by a moveable Langmuir probe biased at +35V, which measured electron saturation current, while moved along the longitudinal axis. These measurements were used for comparison with data generated by the models and the simulation described in Chapter 3.

4.2 EXPERIMENTAL RESULTS.

The results of the fluid code described in section 3.4 were compared with experimental data for an argon plasma, which consists of a single ion fluid. The voltage pulse is modelled as a short, linear rise (2 μs) to maximum voltage, V_0, then

a plateau (2 μs) and finally, a linear fall (200 μs) or an exponential fall (V_0/V_1 = 25 over a fall of 200 μs). The experimental voltage decay is seen in Figure 32 below, with the dotted line representing the exponential model, and the dashed line the trapezoidal model:

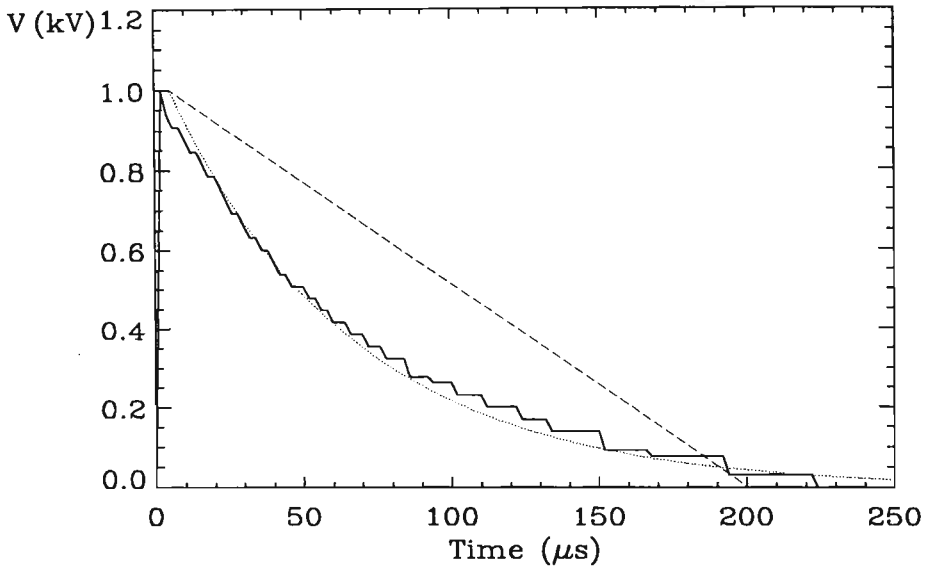

Fig. 32 The experimental voltage decay (solid line), compared with the trapezoidal model (dashed line) and the exponential model (dotted line).

Since the experimental sheath width measurements are only for the first 10 μs, both the trapezoidal (dashed line) and the exponential (dotted line) voltage forms are reasonable approximations to the experimental situation (solid line). The two potential decays can be seen in Figure 33.

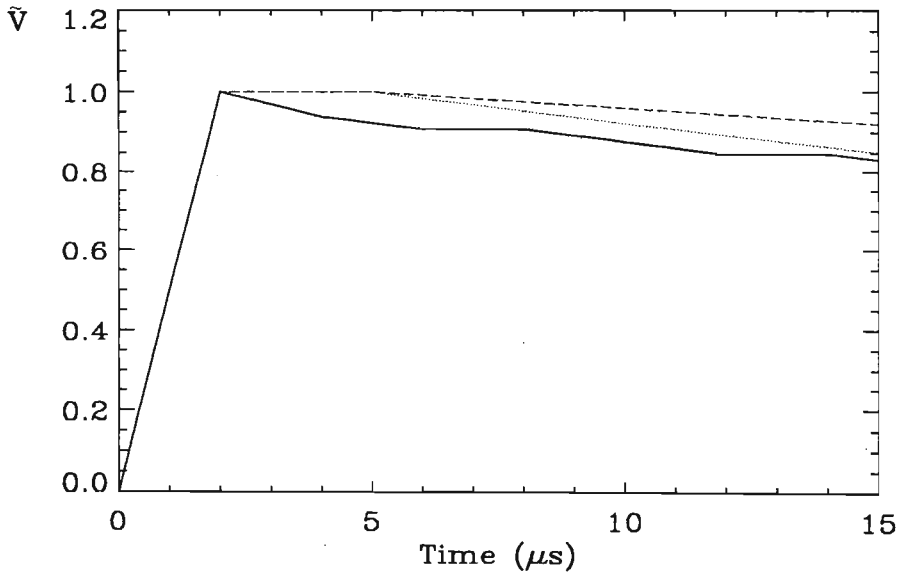

Fig. 33 A comparison of the experimental voltage form (solid line), with the trapezoidal model (dashed line) and the exponential model (dotted line).

The experimental argon plasma had a density of 10^8-10^9 cm^{-3} (10^{14}-10^{15} m^{-3}). The actual peak potential was 7800 V, slightly less than the value of V_0 = 10 kV in the models. The following graph shows the temporal evolution of the sheath for 3 different argon plasma densities. The densities are in the ratio 4.1:7.1:12, although their exact values are not known. For a sheath width greater than 3 cm, when the sheath front becomes less planar and more two dimensional, the identification of the falling sheath edge is less certain since it looks more like a propagating density depletion, and as a result, the sheath expansion appears to decelerate.

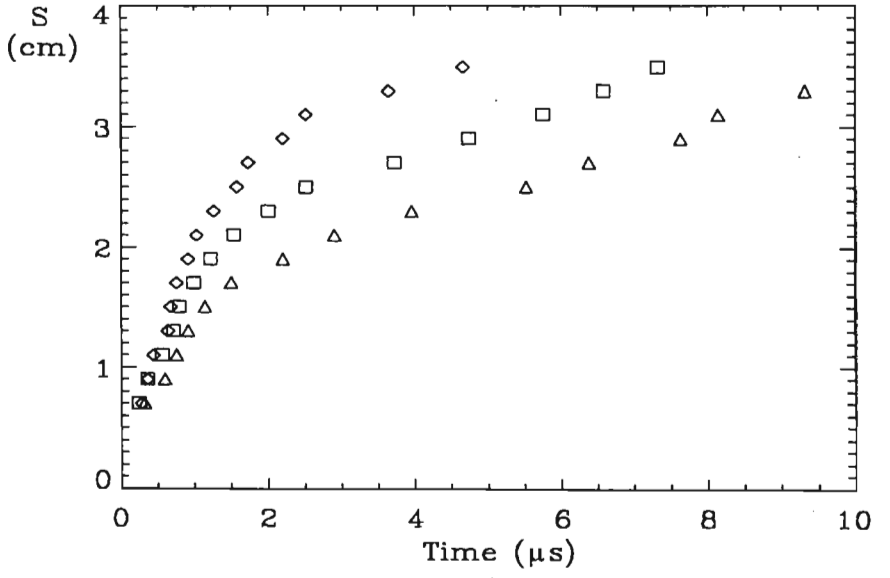

Fig. 34 The experimental sheath width plotted as a function of time. This data was generated by Dr M.J. Alport, as described in section 4.1. The three sets are for argon plasmas with densities in the ratio 4.1 (top) to 7.1 (middle) to 12 (bottom).

Figure 35 shows the temporal evolution of the current to the target.

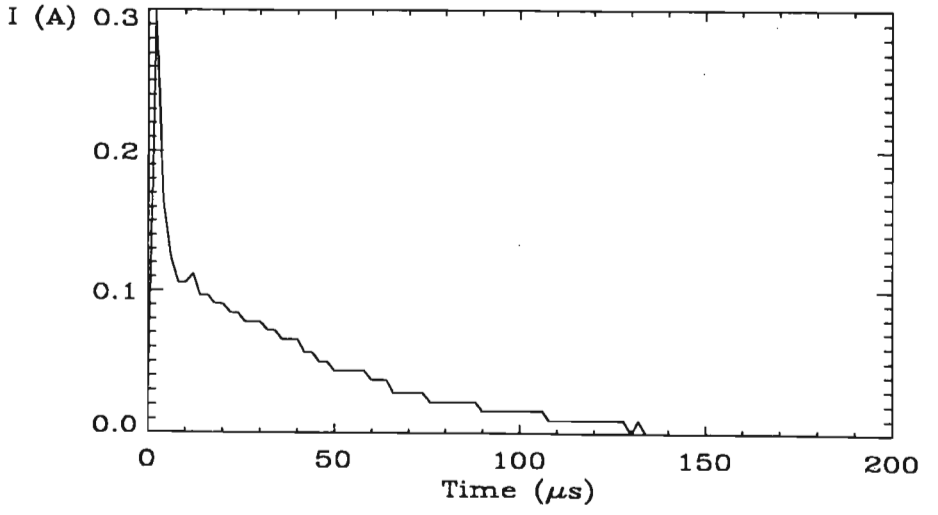

Fig. 35 The experimental current density, generated by Dr M.J. Alport, plotted as a function of time.

The current measured is not only due to the ions that are striking the target; secondary electron emission must also be taken into account. For every ion that strikes the target, there are γ electrons emitted. This means that for each ion of charge q striking the target, a current of $(q + \gamma)\ e$ is measured. Szapiro and Rocca[23] have measured the electron emission coefficient, γ, for a range of incident ion energies on different target surfaces. In particular, for argon ions incident on stainless steel, γ ranges from 1 for 1 keV ions to 5 for 20 keV ions. For 8-10 keV ions, γ was measured at 3-4. For the purpose of comparing the models with the experimental results, the results are decreased by a factor of 5, for the best agreement between the model and the experiment.

4.3 COMPARISON OF MODELS.

The analytical and numerical models are compared with each other and with the experimental results. Density is used as a parameter to obtain the best fit to the experimental data.

Figure 36 shows a comparison of the sheath width calculated from the numerical fluid model of Section 3.4 (solid lines) with the Stewart-Lieberman analytic results of Section 3.3.2 (dotted lines), both generated for a trapezoidal voltage form. Plasma density and ion mass are varied, with line 1: M = 14.02 a.m.u, n = 7.1 x 10^9 cm^{-3}; line 2: M = 39.948, n = 7.1 x 10^9 cm^{-3} and line 3: M = 39.948, n = 1.2 x 10^{10} cm^{-3}.

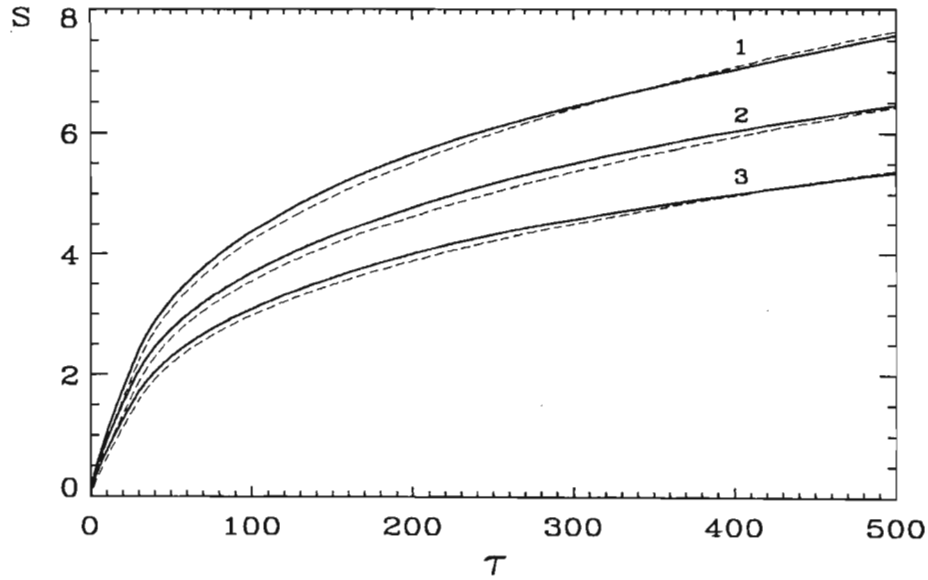

Fig. 36 A comparison of the predicted sheath widths for the numerical (solid lines) and analytical (dotted lines) models, for varying ion mass and plasma density.
Line 1: M = 14.02 a.m.u., n = 7.1 x 10^9 cm^{-3}.
Line 2: M = 39.948 a.m.u., n = 7.1 x 10^9 cm^{-3}.
Line 3: M = 39.948 a.m.u., n = 1.2 x 10^{10} cm^{-3}

Over the long time scale of τ = 500 ion plasma periods, the agreement is close, but it can be seen that for smaller time scales, e.g. τ = 20, the analytical results (dotted lines) are smaller than the numerical results (solid lines). It was established that this discrepancy is independent of plasma parameters and voltage form. Thus, the densities chosen to best fit the experimental data over the short time scale of the experiment are necessarily quite different.

Figure 37 illustrates the problem. Experimental data is obtained over a period of 10 μs, which corresponds roughly to τ = 20. The models are required to fit the data closely over the first 2-3 μs, when the sheath width is smaller than the target dimensions, so that the sheath can still be modelled in one dimension. The numerical model's calculated sheath width for a density of n_0 = 2.2 x 10^{10} cm^{-3} (solid line) fits the early time experimental data very closely. The dashed line shows the sheath width as a function of time for the analytical model for the same density (n_0 = 2.2 x 10^{10} cm^{-3}). It can be seen that the agreement between the model and experiment is not good, over the whole time range. Finally, the analytical model sheath width is plotted for a density of n_0 = 7 x 10^9 cm^{-3} (dotted line), resulting in a much better fit to experimental data.

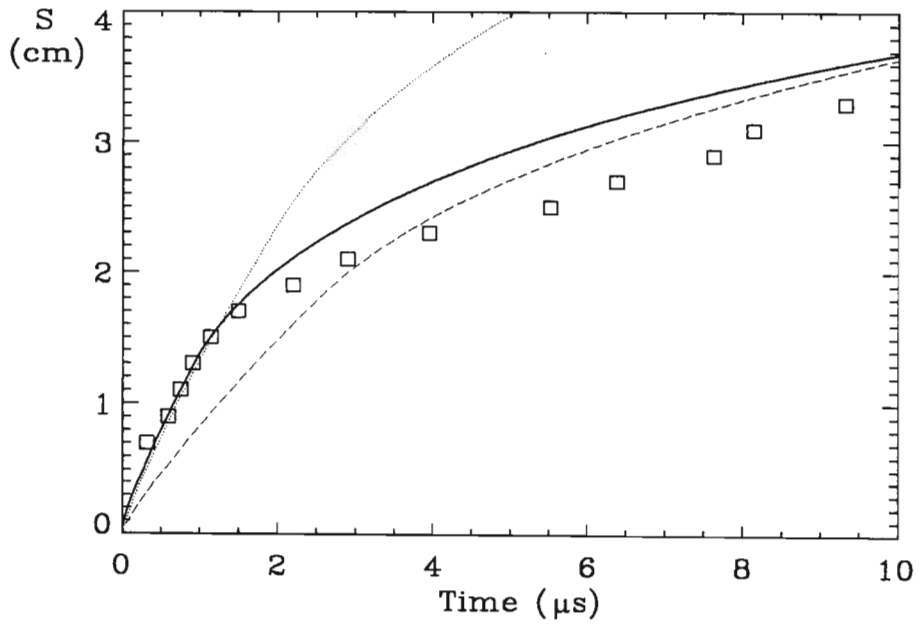

Fig. 37 Comparison of numerical model (solid line) and analytical model (dotted line) with experimental results (□).

The following sections compare the experimental results firstly with the analytical model and then with the numerical model. Next, the numerical model predictions for a two fluid nitrogen plasma are discussed, and in the final section, contour plots of the numerical simulation results are presented.

4.4 ANALYTICAL RESULTS

4.4.1 Comparison with Experimental Data

Density was used as a parameter to find the 'best fit' for the experimental data. Figure 38 shows a plot of the sheath position as a function of time for plasma densities of n_0 = 1.75 x 10^9 cm^{-3} (solid line), 3 x 10^9 cm^{-3} (dotted line) and 7 x 10^9 cm^{-3} (dashed line). These follow the ratio of n_{01} : n_{02} : n_{03} as 4.1 : 7 : 16, which is fairly close to the experimental ratio. Over this short time scale, a simple ramp up to a plateau is a suitable approximation for the experimental voltage form.

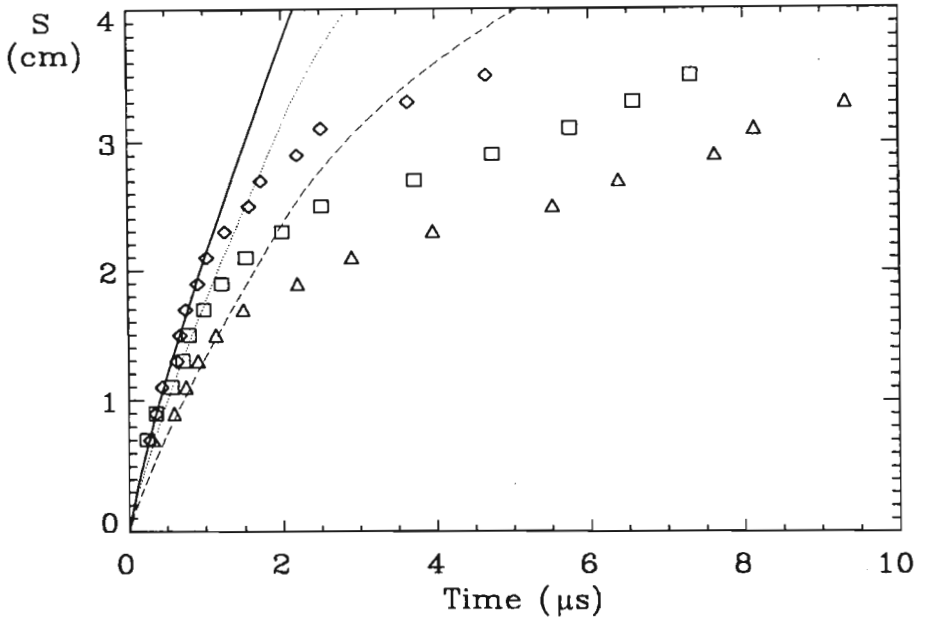

Fig. 38 A comparison of the analytically predicted and the experimental sheath width over time for 3 argon plasmas of densities in the ratio 4.1 : 7.1 : 12.

Using the equations from the Stewart-Lieberman[11] paper, for the ramp and plateau, the current density form in Figure 39 is produced for an argon plasma of density 10^{10} cm^{-3}. This is compared with the experimental current density form (Figure 35). Over the first part of the time scale (up to τ ~ 15), the agreement is fairly close, but for larger τ, the Stewart-Lieberman predicted current is much smaller. Better agreement is obtained for the Numerical model, in Figure 41.

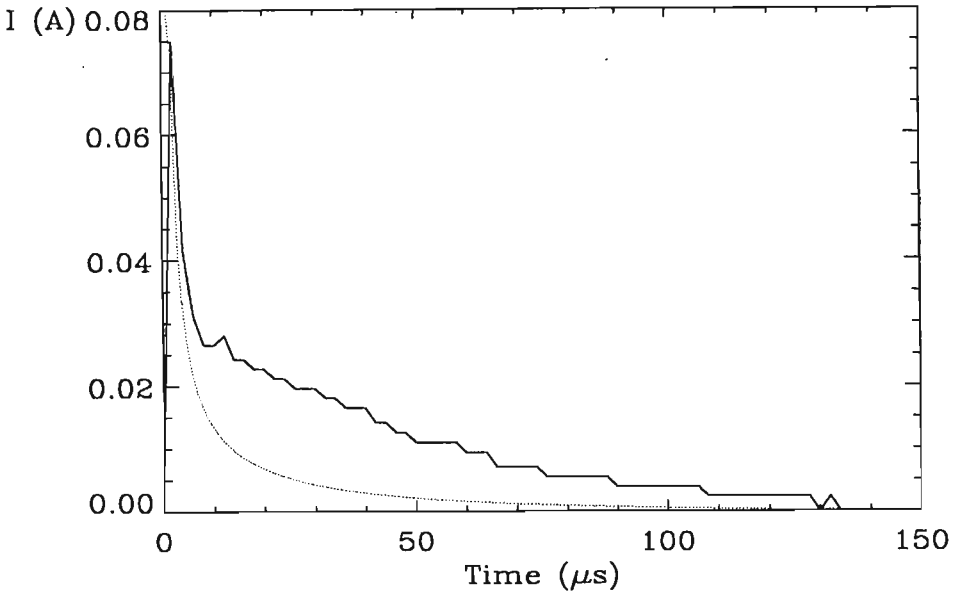

Fig. 39 A comparison of the simulation and the experimental current density.

4.5 NUMERICAL SIMULATION RESULTS

4.5.1 Comparison with Experimental Data.

First, the fluid code was run for an argon plasma for a range of densities around the experimental value of 10^9 cm^{-3}. These densities were used as parameters to find the 'best fit' densities for the experimental data. Figure 40 shows a plot of the sheath position as a function of time for plasma densities of n_0 = 7.5 x 10^9 cm^{-3} (solid line), 1.3 x 10^{10} cm^{-3} (dotted line) and 2.2 x 10^{10} cm^{-3} (dashed line). These follow the experimentally determined ratio of n_{01} : n_{02} : n_{03} as 4.1 : 7.1 : 12.

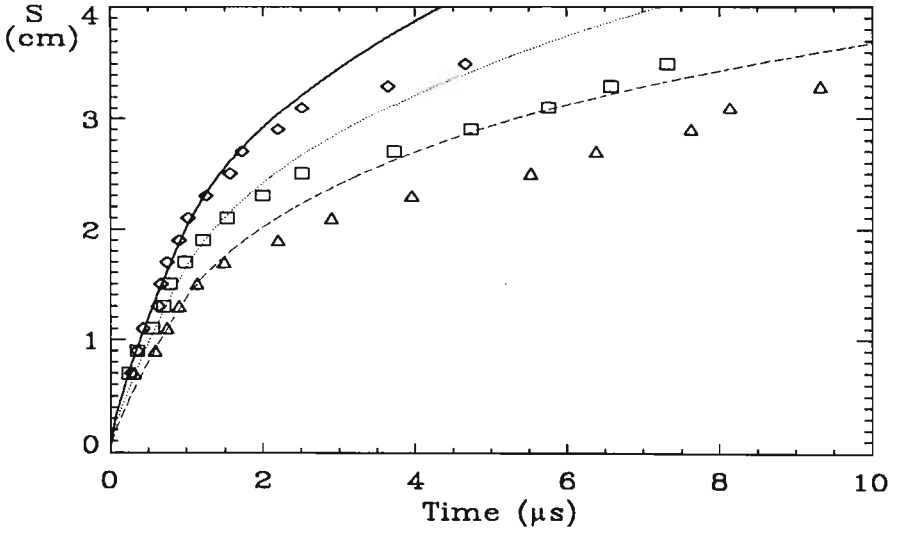

Fig. 40 A comparison of the simulation and the experimental sheath width for argon plasmas of density 7.5 x 10^9 cm^{-3} (solid line), 1.3 x 10^{10} cm^{-3} (dotted line) and 2.2 x 10^{10} cm^{-3} (dashed line).

The model fits the data much more closely, and for a longer time period than the analytical model (Figure 38). The following plot shows the experimental current density plot (Figure 41) compared with the PLANAR1.C prediction, for an argon plasma of density 10^{10} cm^{-3}:

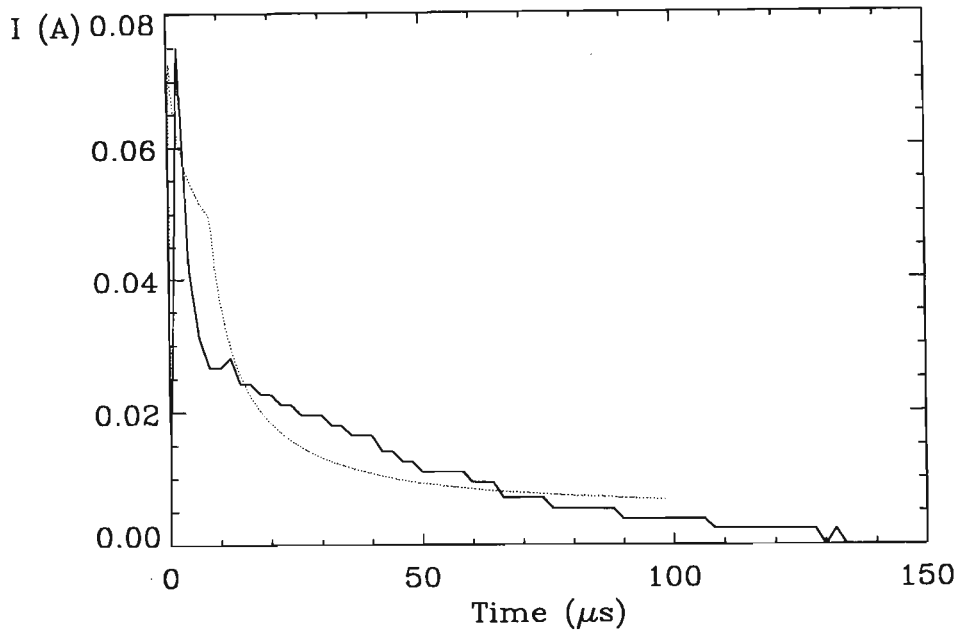

Fig. 41 A comparison of the numerical simulation and experimental current density, showing very good agreement.

In the above figure, the agreement is much closer than that obtained using the Stewart-Lieberman[11] model.

4.5.2 Modelling a Nitrogen Plasma

The fluid code described in Section 3.4 was then run for a two ion fluid nitrogen plasma. The initial plasma density, n_0 was set at 5 x 10^8 cm^{-3}, with a peak potential V_0 = 10 kV and the electron temperature, T_e = 2 eV. The simulation was run for both the trapezoidal and the exponential potential form, with a rise time of 2 μs, a plateau of 10 μs and a fall time of 200 μs, in the case of the trapezoidal voltage form, and in the case of the exponential voltage form, an e-folding decay time of 21.7 μs. A relatively small density was chosen because the ion plasma frequency, ω_{pi}, increases with density. A large plasma period will mean that less time steps are needed to complete the simulation. The largest possible time step, dt, is also used to decrease simulation time. The simulation was run for varying initial densities, ion mass/charge ratios and percentages as shown in Table 2. For most of these runs, dt = 1/40.

While a consistent normalisation with respect to species 1 would have been preferable in Table 2, since equations (73)-(75) and (80)-(82), and the description of program parameters in 3.4.4 and 3.4.5 use normalised charge and mass in terms of species 2, making a change in the notation at this stage would be a major undertaking. Instead, the reader's attention is explicitely drawn to the slightly inconsistent notation.

Data Set	% species 1	% species 2	M_1/M_2	q_1/q_2	Voltage Form
1	25	75	0.5	1.0	T,E
2			0.25	1.0	T
3	50	50	0.5	1.0	T,E
4			0.25	1.0	T
5	75	25	0.5	1.0	T,E
6			0.25	1.0	T
7	100	0	1.0, N^+	1.0	T,E
8	0	100	1.0,N_2^+	1.0	T,E
9	50	50	1.0, N^+	0.5	T
10	50	50	1.0, N^+	0.333	T

Table 2. The different permutations used for the PLANAR1.C simulations. T and E refer to the trapezoidal and exponential voltage forms used in the simulations.

The first column gives the data set reference number, referred to in the following results. Species '1' is always modelled as the N^+ ion fluid (mass 14.02 a.m.u.), while species '2' is always the N_2^+ ion fluid (mass 28.04 a.m.u.). The results are mainly qualitative, and remain normalised, unless it is necessary to use real units. The sheath width, S, is in terms of the ion matrix sheath width, s_0; time, τ, is given in terms of the species 1 ion plasma period and current density, J, is normalised with respect to the species '1' initial plasma density, n_0 and the ion sound speed, c_s.

Firstly, the difference in results for the two voltage forms is shown. Data set 1 is used: 25% N^+ and 75% N_2^+. The trapezoidal voltage form decreases at a less rapid rate in comparison to the exponential voltage form. As a result (Figure 42), for the trapezoidal voltage form, the sheath expands further, and the current density remains fairly large for a longer period. In the following two plots, the solid lines show the voltage form, sheath width and current density for the trapezoidal voltage form, while the dotted lines show comparable data for the exponential voltage form.

In both cases, the sheath width increases most rapidly and the current density is greatest as the voltage form ramps up, and then slows down over the plateau and fall. The sheath width and current density are identical for $\tau < \tau_r + \tau_p$. For $\tau > \tau_r + \tau_p$, the sheath width and current density are larger over the trapezoidal voltage fall.

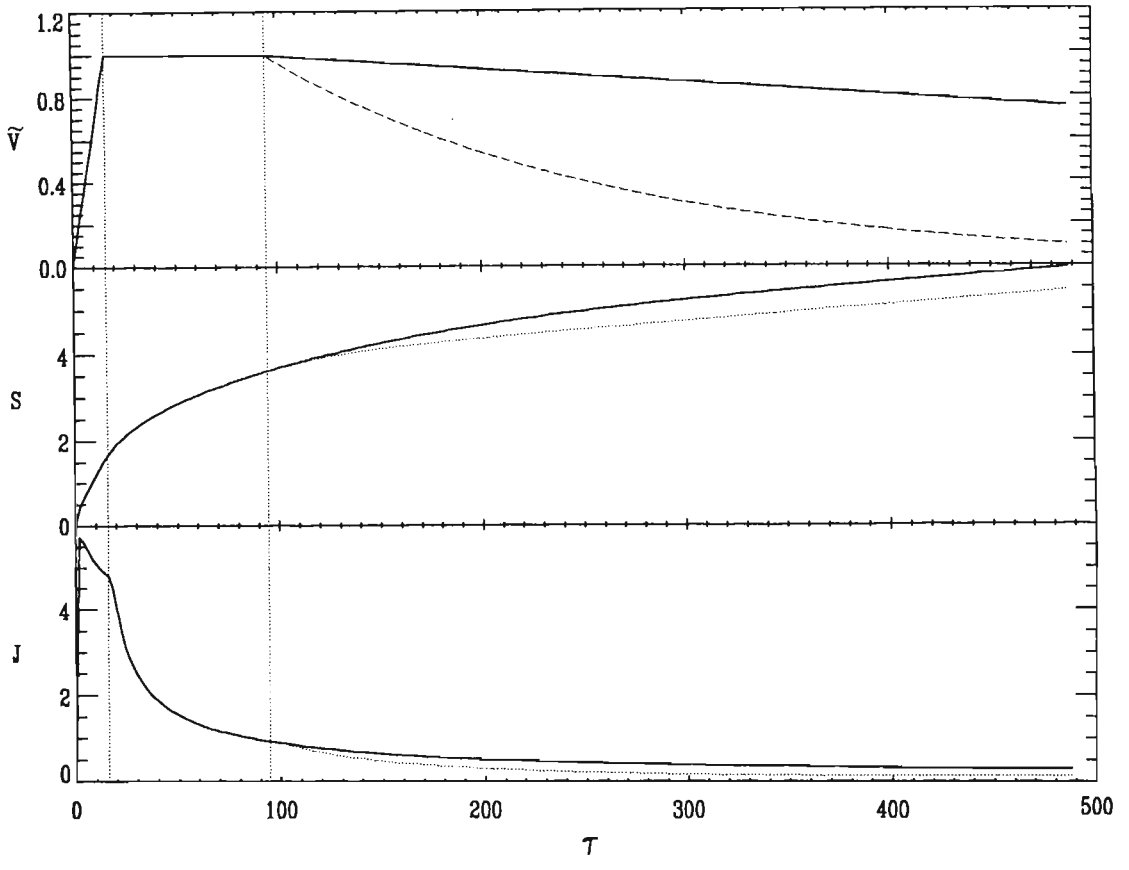

Fig. 42 Voltage form (top), sheath width (middle) and current density (bottom) plotted as a function of time for a trapezoidal voltage pulse (solid lines) and an exponential voltage pulse (dotted lines).

The following results are all given for a trapezoidal voltage form, for consistency. Figure 43 shows a plot sheath width as a function of time for data sets 1 (solid line), 3 (dotted line) and 5 (dashed line). As the percentage of N^+ ions increases, the sheath width tends to increase more rapidly. This would indicate that more ions must be uncovered to supply the sheath, and therefore, the lighter N^+ ions implant at a greater rate.

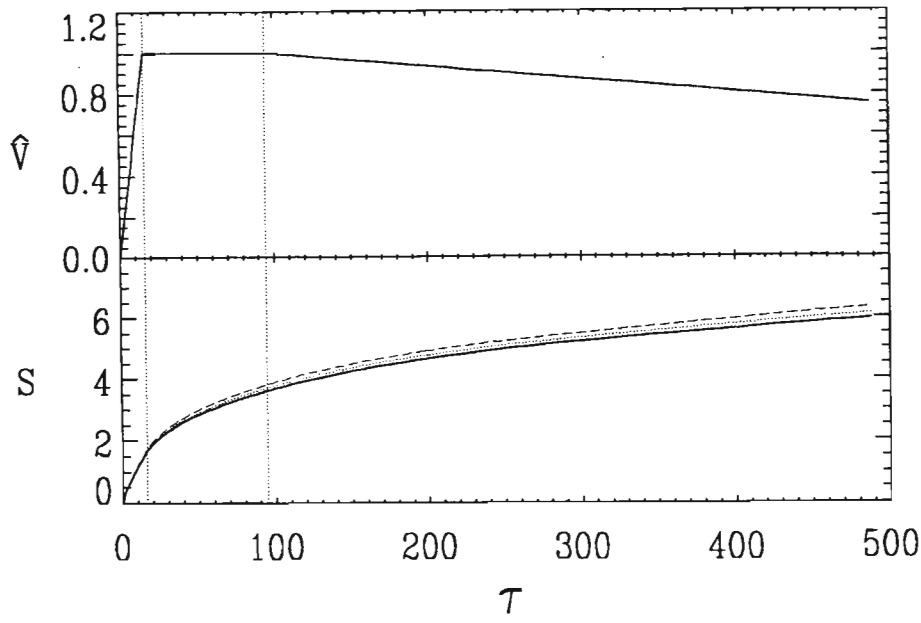

Fig. 43 Sheath width and voltage profile plotted as a function of time for data sets 1 (solid line), 3 (dotted line) and 5 (dashed line).

The fact that the lighter ions are more mobile and are implanted more rapidly is confirmed in Figure 44, which shows a plot of the current density at the target surface as a function of time, expressed in terms of the initial density , n_0, and ion sound speed, c_s. The dotted line is the current density due to the lighter ions (N^+), while the dashed line is the current density due to the heavier ions (N_2^+). The solid line is the sum of the two current densities in each case.

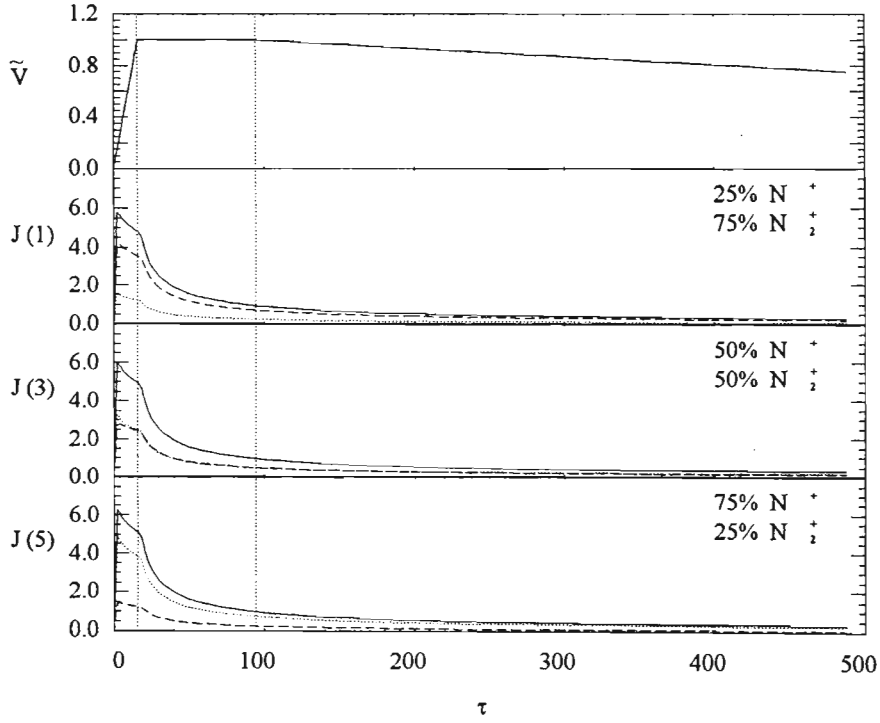

Fig. 44 Voltage profile and current density plotted as a function of time for data sets 1 (top), 3 (middle), and 5 (bottom).

As the percentage of N^+ ions increases, the peak current density also increases. The higher concentration of N^+ ions also causes the current density to remain larger for a longer time period. In the middle graph (data set 3), the current density due to the N^+ ions (dotted line) is larger than that due to the N_2^+ ions over the whole time period.

The next results were produced to see the effect of a much heavier species 2 ion. This is not realistic for a nitrogen plasma, but for plasmas consisting of gas mixtures, it gives a good idea of the effect of ion mass on the sheath width in Figure 45, and on current density in Figure 46. In Figure 45, sheath width is plotted as a function of time for data set 1 (solid line) and data set 2 (dotted line). The lighter ions are depleted more quickly, causing the sheath width to increase more rapidly.

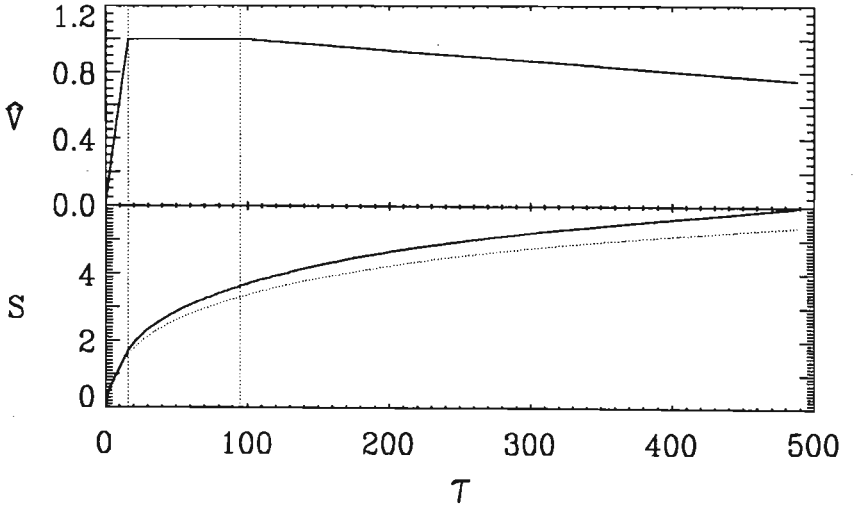

Fig. 45 Sheath width plotted as a function of time for data sets 1 (solid line) and 2 (dotted line).

In Figure 46, the trapezoidal voltage form is plotted above the current densities for data set 1, J(1) and data set 2, J(2). For both J(1) and J(2), the dotted line represents the species 1 current density, which are identicle. The dashed lines are the current densities due to species 2. The solid lines are their sum.

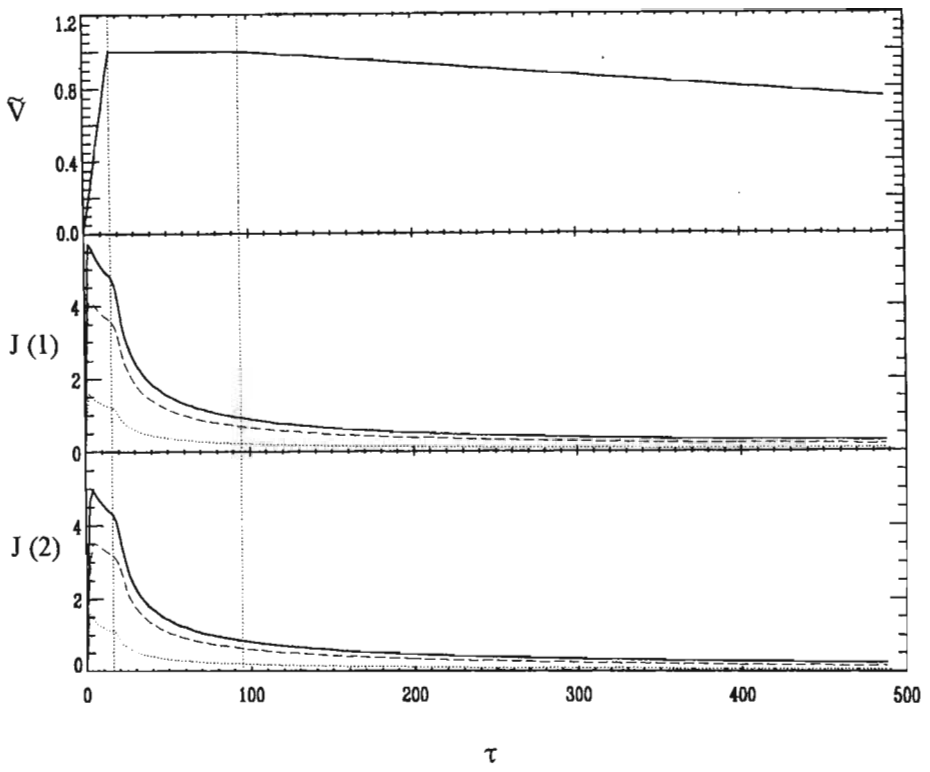

Fig. 46 Voltage plotted as a function of time with current for data set 1 (middle) and 2 (bottom).

It can be seen that the current density is much larger for the 'lighter' plasma, where the ions respond more rapidly to the applied potential.

The effect of charge is shown in Figure 47(a). Two more runs were made, one for a singly charged species 1 and a doubly charged species 2, both of mass M_1 (data set 9), and then another for a triply charged species 2 (data set 10). The resulting sheath width and current densities were compared with the results for a plasma consisting of a singly charged ions of mass M_1 (data set 7).

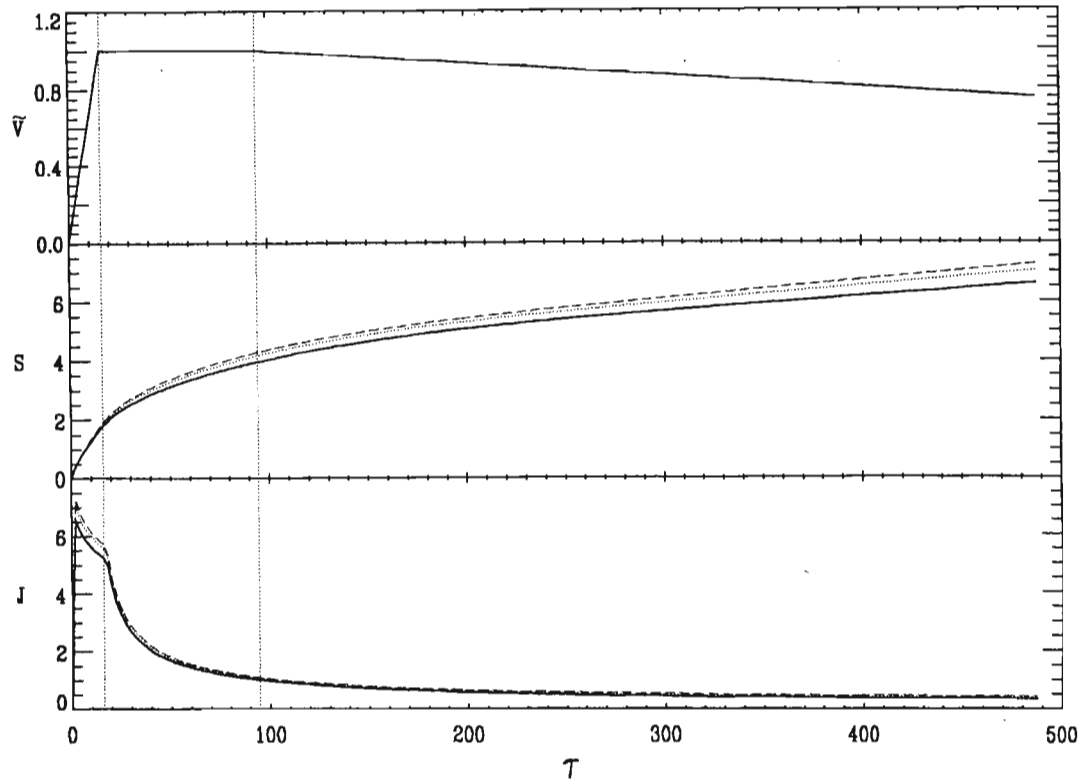

Fig. 47(a) Voltage, Sheath width and Current density plotted as a function of time for data set 7 (solid lines), 9 (dotted lines) and 10 (dashed lines).

Since the charge of species 2 (data sets 9 and 10) is greater, so is its acceleration, and therefore so is the resulting total current density. The sheath depletion and consequent expansion is also more rapid for larger ion charge. Figure 47(b) shows a plot of the velocities of the different charged species at the target (ng = 400). The solid line represents the singly charged ion velocity, while the dotted line is for the doubly charged ions, and the dashed line is for the triply charged ions. As the charge increases, so does the velocity of the ion as it strikes the target. The Courant condition limits the distance that a fluid element may travel in one time step. Since the velocity is proportional to $(Ze\phi)^{1/2}$, it is necessary to decrease the time step dt for data sets 9 and 10.

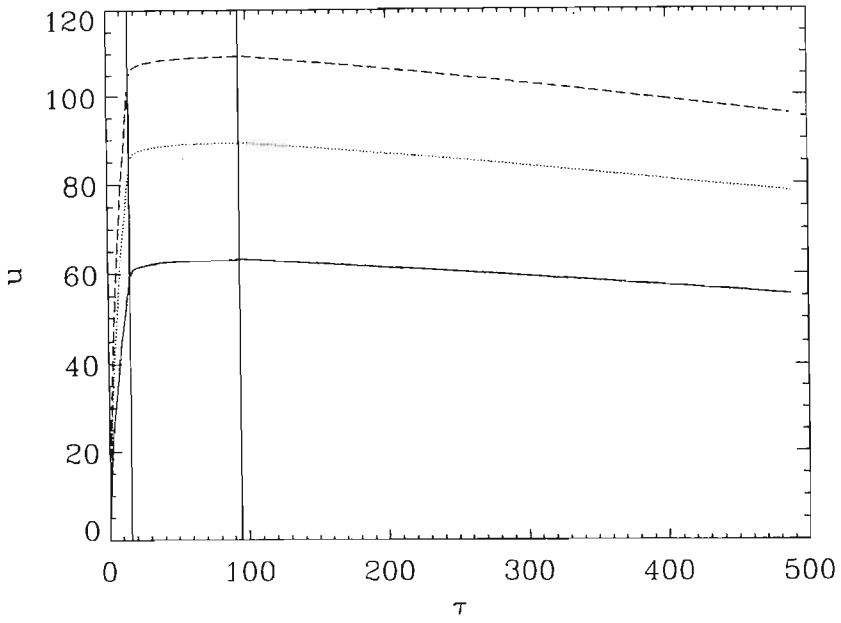

Fig. 47(b) Ion velocity at the target plotted as a function of time for ions of single charge (solid line), double charge (dotted line) and triple charge (dashed line).

Figures 42 to 47(b) illustrate the effects of voltage form, N^+ percentage, ion mass and ion charge. Optimum results are predicted for higher percentages of the N^+ ions, low ion mass and large ion charge, as well as longer plateaus on the voltage form.

4.5.3 Contour Plots.

The following plots were first presented by Dr M.J. Alport at the International Workshop on Plasma-Based Ion Implantation in Madison, Wisconsin in August 1993[36]. A contour plot of ion densities, $\tilde{n}_1$ and $\tilde{n}_2$ normalised with respect to n_0, as a function of normalised position in the grid, ξ, and normalised time, τ, was generated for a nitrogen plasma consisting initially of 25% N^+ ions of mass M_1 and 75% N_2^+ ions of mass M_2 (data set 1). This plot is shown below. Density is normalised relative to the initial density, $n_0 = 5 \times 10^8\ \mathrm{cm}^{-3}$, the specific value of which has a slight effect on the resulting data. Time is normalised relative to the ion plasma period, ω_{pi}^{-1} of the lighter ion. The pulsed target is situated at ξ = 400. The densities of both ion fluids decrease rapidly initially, but for larger τ the distribution becomes flatter. The ions are depleted over time, with the N^+ ions being depleted more rapidly than the more massive N_2^+ ions. This is because the more massive N_2^+ ions (M_2) have a greater inertia, and so move more slowly through the sheath, so that their density decreases less rapidly than that of the lighter N^+ ions (M_1).

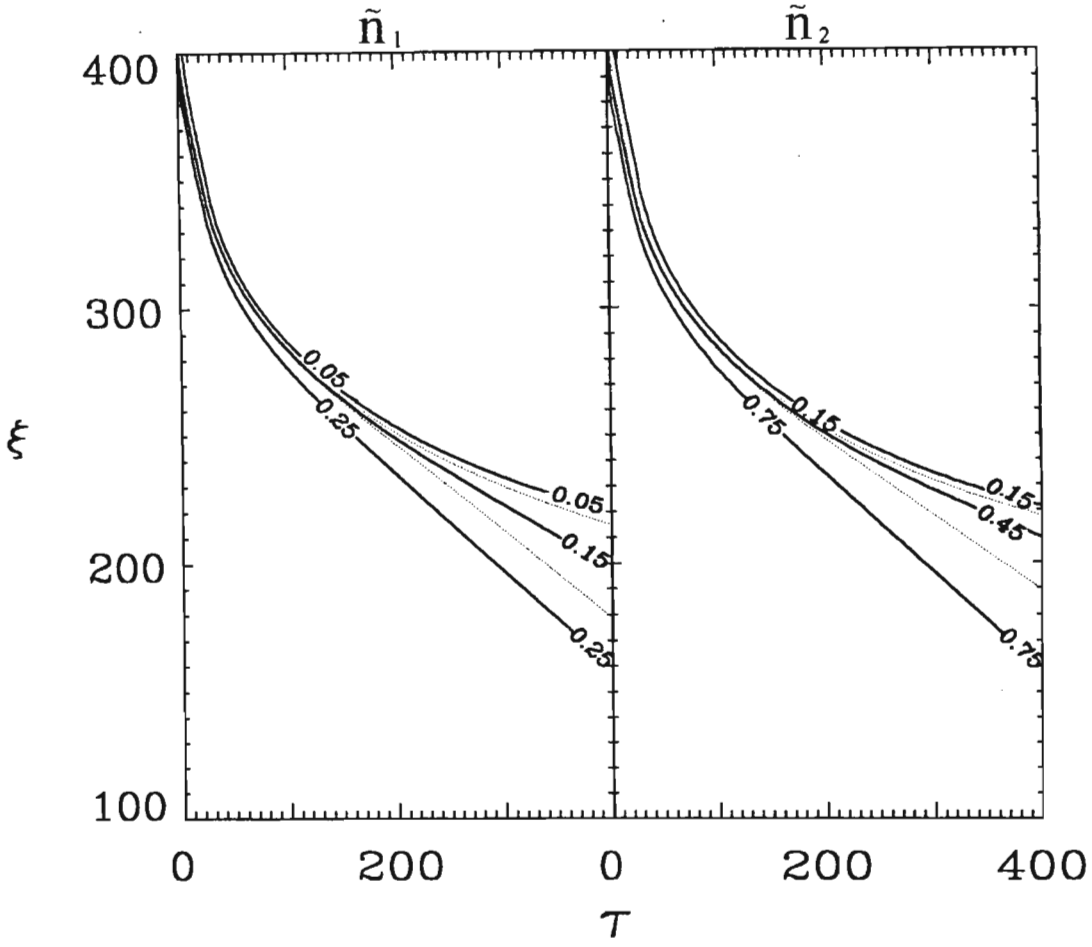

Fig. 48 A contour plot of the density normalised with respect to n_0, as a function of position in the grid, ξ, and normalised time, τ, for data set 1.

A contour plot of ion velocities u_1 and u_2 as a function of position, ξ, and time, τ, was generated for the same nitrogen ion densities (data set 1). The ion velocity is normalised relative to the ion sound speed, c_s of the lighter ion. Initially the ions closest to the target are accelerated, but as τ becomes larger, ions further away are accelerated towards the target. The lighter N^+ ions reach maximum velocity 63.8 c_s, which is close to $v_{max} = 64\ c_s$. The more massive N_2^+ ions require a longer time to reach a smaller maximum velocity. There is no ion velocity dependence on the initial percentages of N_2^+ and N^+ ions.

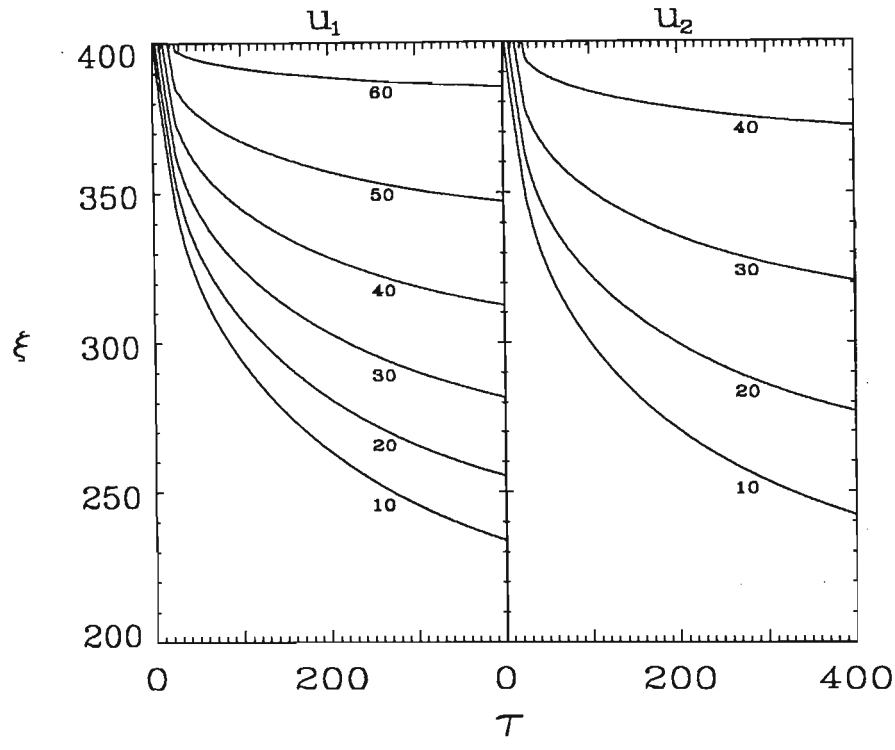

Fig. 49 A contour plot of the velocity, normalised with respect to c_s, the ion sound speed of the lighter species, as a function of position in the grid, ξ, and normalised time, τ, for data set 1.

From the density and the velocity, the current density, $J = \tilde{n}u$, for each ion fluid can be calculated. Figure 50 shows a contour plot of total current density as a function of normalised position, ξ, and normalised time, τ, for a nitrogen plasma with different initial percentages of N^+ and N_2^+ ions (data sets 1, 3 and 5). Current density is normalised relative to the species 1 mass and ionisation, and the time scale is in terms of the species 1 plasma frequency. Over the first 10 ion plasma periods, the current density increases rapidly to a maximum, which is greater and more sustained for plasmas consisting of a higher initial percentage of N^+ ions, as was seen in the density plots, where the less massive ions were depleted slightly more rapidly. The high current density they generate is due to the fact that they are less massive and so move at higher velocities towards the target surface, from the sheath edge. Over the rest of the time period, the current density slowly decreases, though it still remains largest in the bottom graph for 75% N^+ ions showing that the larger the percentage of N^+ ions, the greater and more sustained the current density peak.

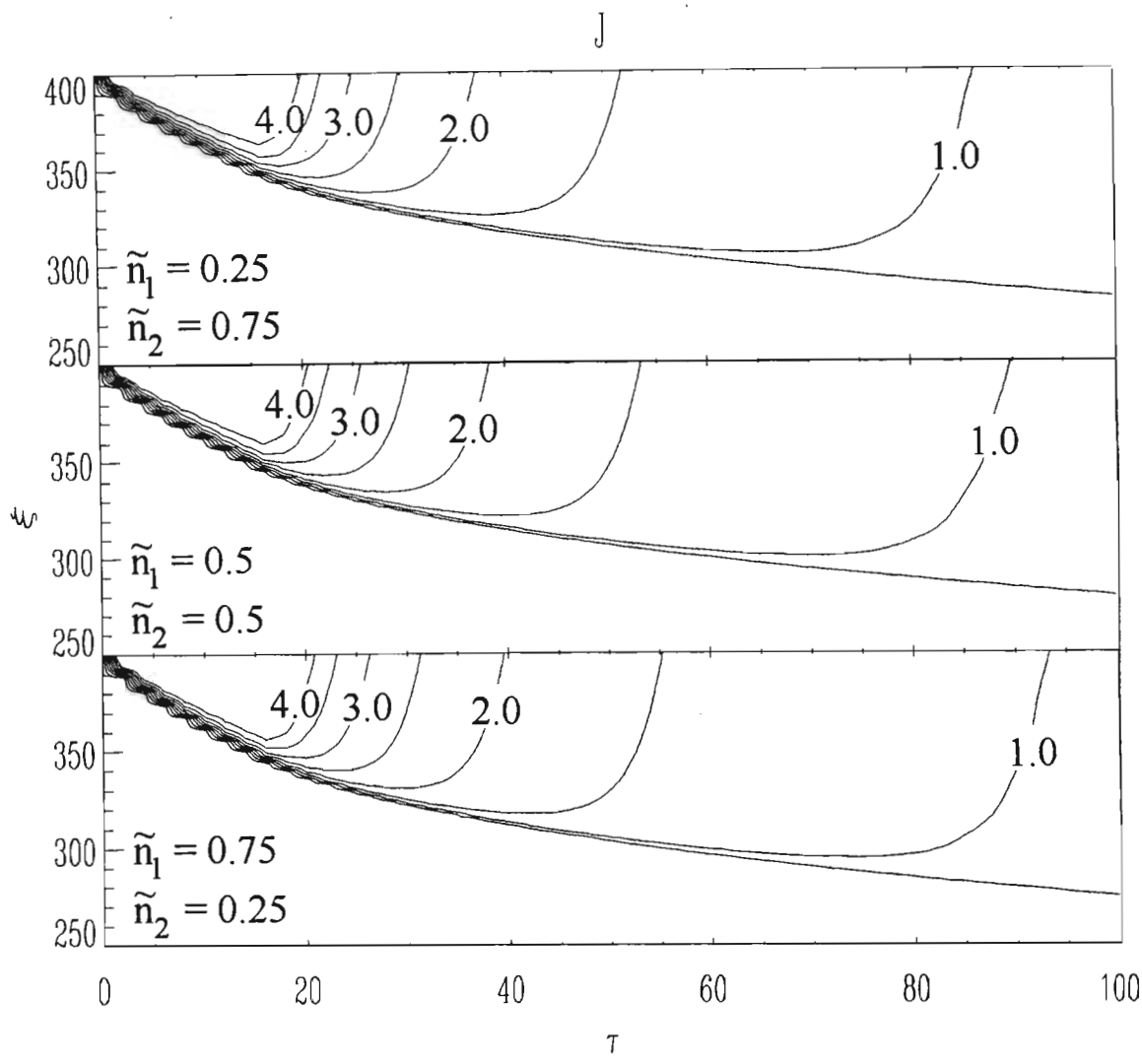

Fig. 50 A contour plot of the current density, normalised relative to the lighter species parameters, as a function of position in the grid, ξ, and normalised time, τ, for data sets 1, 3 and 5.

4.6 TAMIX RESULTS

The TAMIX program was run for a target material consisting of 304 stainless steel, with ion mass and energy given in Table 3. The atomic abundances of 304 stainless steel are given in Table 1 in Section 3.5.4. For best results, TAMIX allows only one ion species in the simulation, so that the implantation is necessarily modelled separately for the N^+ and N_2^+ ions. TAMIX also does not allow for the break up of the N_2^+ ion once it is inside the metal surface, which is a further limitation.

Data Set	Incident ion mass (u)	Incident ion energy (keV)	Maximum Fluence (cm^{-2})
1	14.02	8	10^{18}
2	28.04	8	10^{18}

Table 3. Data used in TAMIX runs.

The results of these runs are shown below. Firstly, in Figure 51, the percentage distribution of implanted N^+ ions with an incident energy of 8 keV (data set 1) is plotted as a function of depth and ion fluence. Figure 52, shows a similar plot for N_2^+ ions, with an incident energy of 8 keV (data set 2).

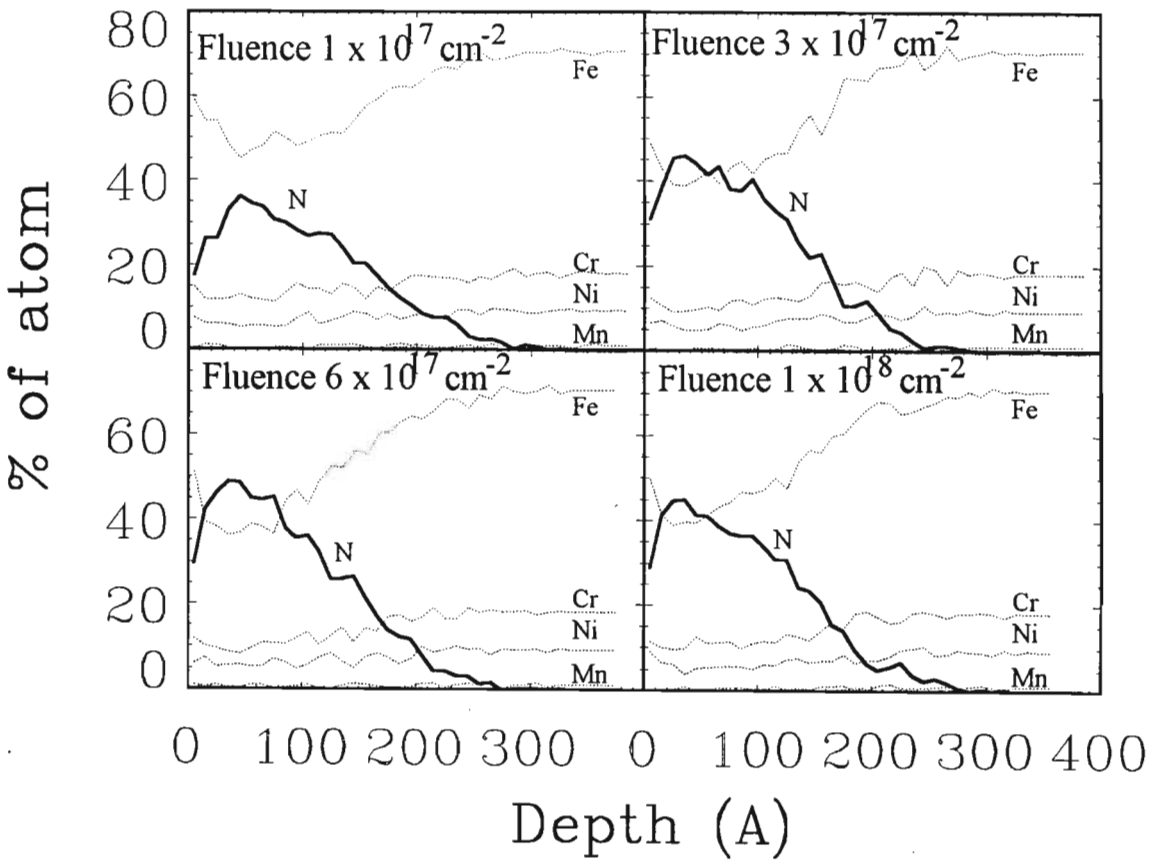

Figure 51 TAMIX results for data set 1: The percentage distribution of implanted N^+ ions with an incident energy of 8 keV (data set 1) is plotted as a function of depth and ion fluence.

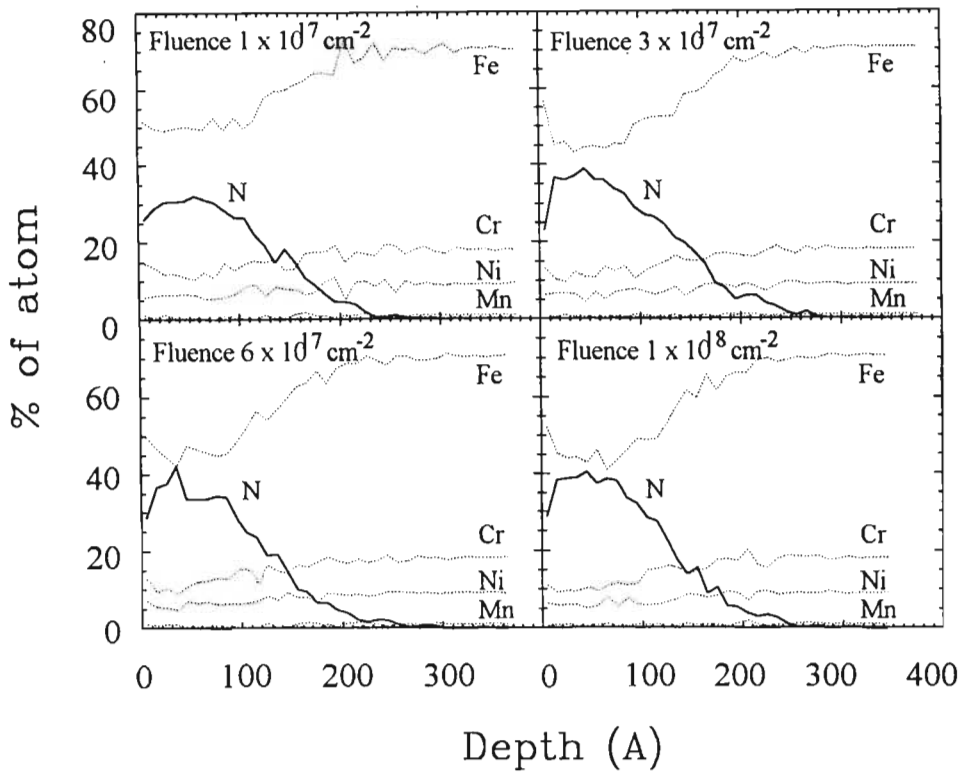

Figure 52 TAMIX results for data set 2: The percentage distribution of implanted N_2^+ ions with an incident energy of 8 keV (data set 2) is plotted as a function of depth and ion fluence.

The less massive N^+ ions implanted to a slightly greater depth and concentration than the more massive N_2^+ ions. It is also interesting to note how the surface concentration of the target atoms, in particular the Fe atoms, is decreased as the ion fluence increases. This is, in part, due to sputtering of the surface by the incident ions. The decrease in ion concentration was also more marked for the lighter N^+ ions.

Considering the greater decrease in concentration of target atoms for the incident N^+ ions, it would be expected that the wear on the surface of the target (surface recession) is much greater for these ions than for the N_2^+ ions. In Figure 53, the surface recession of the target is plotted as a function of ion fluence for the N^+ and N_2^+ ions.

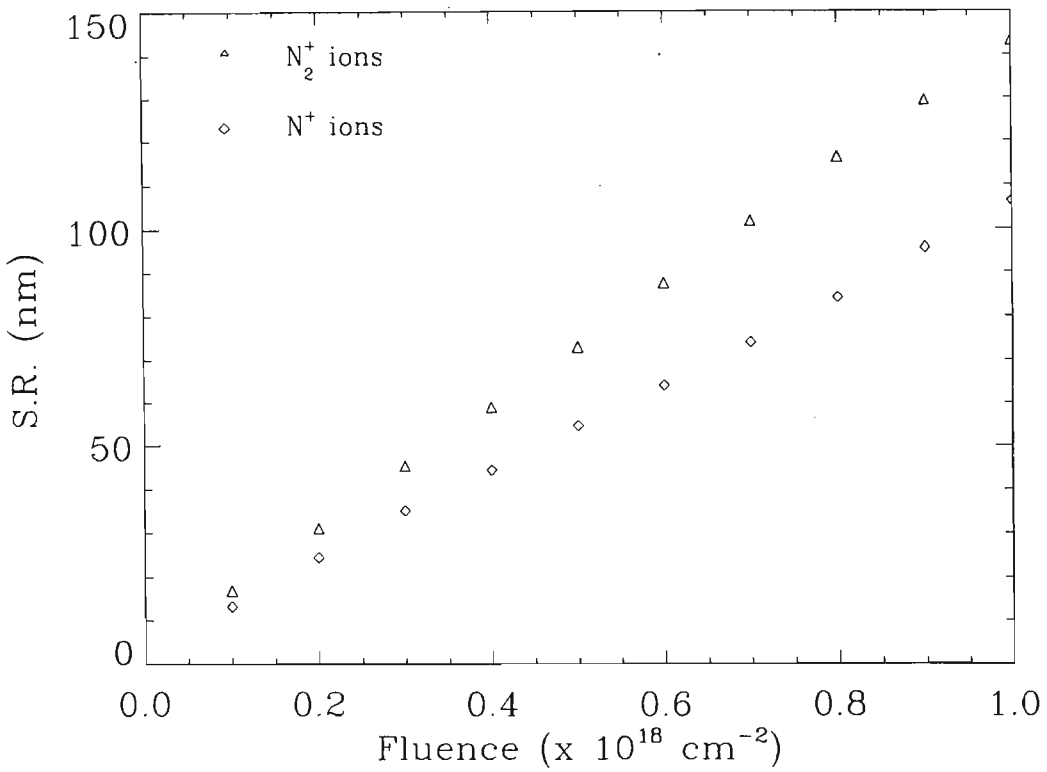

Figure 53 Surface recession plotted as a function of fluence. The surface recession for the more massive N_2^+ ions is approximately 35% greater.

It can be seen that the surface recession is greater for the equally energetic, but more massive N_2^+ ions.

4.7 DISCUSSION

From all these results, it would seem that the optimum nitrogen plasma for ion implantation would be one with a very high percentage of N^+ ions. These ions produce a larger ion current density at the target, and therefore a larger dose. TAMIX has also demonstrated that the lighter ions produce deeper implantation, to higher concentrations, with less surface recession of the target.

CHAPTER 5

CONCLUSION

5.1 SUMMARY

Plasma Source Ion implantation involves placing a metal target in a background (usually nitrogen) discharge plasma and repeatedly applying large (> 25 kV), short (~15 μs) pulses. The high energy implanted ions have been found to pin dislocations and so improve the wear and microhardness properties of industrial cutting tools.

In this thesis, a number of models have been used to examine the plasma response after the application of the voltage pulse. For the first time, the models specifically include aspects of a typical PSII experimental arrangement such as shape of the particular voltage waveform, a mixture of ion species and the atomic composition of the target.

Based on the early models of Lieberman *et al* [9,11], analytic expressions are derived for the sheath velocity, current density and ion energy profiles for a waveform having a 1 μs rise time and a slow 6 ms exponential decay. Next, a one dimensional time-dependent plasma fluid code has been developed to simulate sheath evolution following the high voltage pulse for a plasma consisting of one or two ion fluids. This is useful, in particular, to model the nitrogen plasma in typical nitriding PSII implantations which consists of approximately 25% N^+ ions and 75% N_2^+ ions[19]; the actual ion mix ratio varies with gas pressure, discharge current and background gas. The ions are assumed cold and collisionless, while the electrons are assumed to follow the Boltzmann equation. By using finite differences to solve the fluid equations of motion together with the Poisson equation, the spatially and temporally resolved plasma density, and velocity (and hence the ion flux to the target) as well as the sheath position and width have been calculated. For completeness, different charge states have also been included for the two ion species, thus describing the behaviour of other plasma mixtures.

Finally, results have been obtained from the Monte Carlo based TAMIX particle simulation code for mono-energetic ions incident on 304 stainless steel. The resulting atomic concentration profiles as well as the surface recession due to sputtering have

been described. In summary, a mixture of analytic, numerical and particle simulation models have been used to describe the complete PSII process including the application of a voltage pulse, the plasma response and finally the resulting atomic concentration profiles in the target. These models may thus be used to optimise the PSII process for various specific applications, although the model still needs more careful experimental verification.

5.2 POSSIBLE EXTENSIONS OF THE WORK.

There are a number of possible extensions to this thesis.

The effect of secondary electron emission needs to be examined. Since the typical secondary electron emission coefficient has a large value ~ 4, this represents a good proportion of the total load on the pulsed power supply since only a small fraction of the total current may be attributed to the incident ion flux. This also makes it difficult to infer an ion dose by measuring the current drawn to the workpiece.

The experimental identification of the sheath position is usually obtained from a Langmuir probe biased to collect electron saturation current. The fluid model could be used to determine the theoretical shape of this probe signal to provide a more unambiguous identification of the sheath position from the probe trace, so that the time scale of the experimental data could be extended.

Finally, the evolution of the plasma sheath around two dimensional targets needs to be examined for a number of reasons. The evolution of individual sheaths from a number of small targets in a batch processing arrangement can influence the implantation uniformity on each individual target. The issue of conformality or the ability of the sheath to follow the contour of the underlying object (e.g. gear teeth) still needs to be examined. It was initially thought that the sheath retained the shape of the target so ensuring almost normal ion incidence. More recently, it appears that this is not the case because the sheath rapidly becomes spherical. It is not clear to what extent this affects the final implant profiles.

APPENDIX A

RUNNING TAMIX

In this appendix details about running the TAMIX program are described. This information is specific to the data presented in this thesis and is included for completeness. More general information is available both in Han's thesis[33] and his paper[34].

TAMIX was originally written in Cray FORTRAN, and was later translated by Jake Blanchard to FORTRAN-77. Unfortunately, something was lost in the translation, and thus far, it has been impossible to get TAMIX to run in the collisional-diffusional-dynamic mode. The other two modes, however, do work. These are the static and the collisional-dynamic modes, described in Section 3.5.

TAMIX was run on the SUN (address: swift.ph.und.ac.za) at the University of Natal, and is still available, with a number of input files, on the directory PLASMA\PLASMA\KIMT. A copy of the source code is also included in Appendix B. Two other file, SATABLEU and ATDATA are also necessary for the running of TAMIX, and are included for convenience, although TAMIX is able to regenerate them. Typical input and output files are also included.

The input file is broken up into a number of groups, which are now explained in detail.

THE MASTER BLOCK

```
N+ ion impl on type 304SS
FLUT= 1.0E+19      NIH =   5000 NG =    20  NOUT=     10
ZI1A=    0.0  ZI2A= 1500.0        IMP =     5
DZL0=   10.0       DZLP=   10.0
```

The first line is a title line for the simulation.
The second line contains:

1. FLUT is the total ion fluence, or total number of ions striking the target, for the whole time period. Units: cm^{-2}
2. NIH is the number of ion histories, that is, the number of ions used to model the whole implantation process.
3. NG is the highest group index of recoils to be followed. To save simulation time, in some cases, grouping of recoil atoms is used in TAMIX. The ion has index 0, the first atom struck by the ion index 1, the second atom struck by the first atom index 2 and so on. For considering sputtering yield, or dynamic simulation, a full cascade should be used for accurate results.

4. NOUT is the number of outputs to be printed at intermediate ion fluences, as TAMIX models the process. For example, if NOUT = 5, for FLUT = 10^{19} cm^{-2}, results will be plotted for ion fluences of 10^{18} cm^{-2}, 2.5×10^{18} cm^{-2}, 5×10^{18} cm^{-2}, 7.5×10^{18} cm^{-2} and 1×10^{19} cm^{-2}.

The third line sets the important region. In this region, one ion history is divided up into a number of ion histories, for a more accurate result in this region. The larger the important region, the longer the program will take to run. The surface interactions are most important in PSII, and, as a result, this region is chosen as the important region.

1. ZI1A is the start of the important region, measured in Angstroms (10^{-10} m).
2. ZI2A is the end of the important region.
3. IMP is the number of ion histories, which one ion history becomes, in the important region.

The last line of the master block contains the layering information. During collisional calculation in TAMIX, the target is divided into many thin layers, in each of which the composition is assumed to be uniform.

1. DZL0 is the thickness of the sublayers in the collision region. If too small a thickness is used, part of the target may not be covered, but if too large a thickness is used, the results will be averaged unrealistically.
2. DZLP is the width of the profiling interval, for output, and should be larger than DZL0. If this is the same value as DZL0, non-smoothed data will be printed.

THE ION BLOCK

The Ion block contains information on the ion species and energies. Implantation of multiple ion species can be handled, though the maximum number of ion species with a different atomic number is 3 and the maximum number of different ion energies is 10. The incident angle for PSII is assumed to be zero, although there are now some indications that this is not the case for sharp edged targets[5-7].

```
Z =    7          M = 14.02  ES =  0.00  ED = 25.00
EKEV=  16.0       ANGL=  0.00       FKEV= 100.00
```

A nitrogen plasma consists of both N^+ ions (mass 14.02 u) and N_2^+ ions (mass 28.04 u), in varying percentages.

1. Z is the atomic number of the ion species.
2. M is the mass number of the ion species. If 0.00 is given as an input value for M, ES or ED, TAMIX will look up the information from an atomic data table.
3. ES is the sublimation energy of the ion species in eV.
4. ED is the displacement energy of the ion species in eV.
5. EKEV is the incident kinetic energy of the ion species, in keV.
6. ANGL is the incident angle of the ion species. (0° is perpendicular to the surface)
7. FKEV is the percentage of the ion species with the above characteristics. FKEV is not required to be normalised.

THE TARGET BLOCK

THLA= 5000.0 DENS= 7.78

Z =	26	ES =	4.34	ED =	17.00	CHI = 70.70
Z =	24	ES =	4.12	ED =	28.00	CHI = 18.30
Z =	28	ES =	4.46	ED =	24.00	CHI = 9.30
Z =	25	ES =	2.92	ED =	25.00	CHI = 1.20
Z =	14	ES =	4.70	ED =	14.00	CHI = 0.50

The Target block contains information about the composition of the target. The target may consist of up to 5 layers, and the maximum number of different atomic species in a layer is also 5. However, the total allowable number of atomic species in the plasma/target system is 6, so that for PSII using a nitrogen plasma with 2 ion species, only 4 other ion species can be used to describe the target. The Target block describes the 4 main elements of type 304 stainless steel, which actually consists of the following elements (Section 3.5.4):

Species	Fe	Cr	Ni	Mn	Si	C	P	S
Mass No.	26	24	28	25	14	12	15	16
Typical %	70.7	18.3	9.3	1.2	0.5	0.025	0.021	0.017

Table 1. The atomic composition of 304 stainless steel.

1. THLA is the thickness of a target layer in Angstroms.
2. DENS is the mass density of the target layer in $g.cm^{-3}$. If 0.00 is used for DENS, Z, ES or ED, TAMIX will read the data from an atomic data table.
3. Z is the atomic number of the target species.
4. ES is the sublimation energy of the target species in eV
5. ED is the displacement energy of the target species in eV
6. CHI is the percentage of a species in a layer, normalised automatically.

The compound block contains information on any compounds in the system. For a nitrogen plasma implanting ions into type 304 stainless steel, no compounds are necessary for the simulation.

TAMIX was run in the collisional mode, with the above settings. A large output file is produced, consisting of a number of different sections: the input data, with details on the run mode (collisional) and run type (random start), range and sputtering data, and profile and simulation information. As this is a dynamic simulation, the results at NOUT intermediate fluences are printed out. For further information on the output file, S. Han's Ph.D. thesis[33] or paper[34] on the subject may be consulted.

APPENDIX B

THE US PATENT

4,764,394

METHOD AND APPARATUS FOR PLASMA SOURCE ION IMPLANTATION

John R. Conrad, Madison, Wis., assignor to Wisconsin Alumni Research Foundation, Madison, Wis.

Filed Jan. 20, 1987, Ser. No. 5,457
Int. Cl.[4] B05D *3/06*
U.S. Cl. 427—38 37 Claims

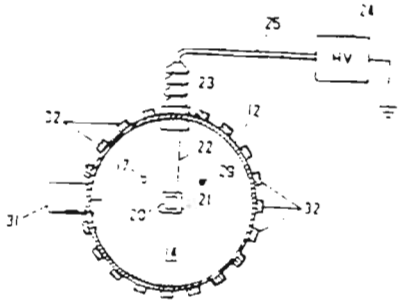

20. A method of implanting ions in a target object comprising the steps of:

(a) providing an enclosing chamber having walls of electrically conductive material;

(b) suspending a target object within the chamber spaced away from the walls of the chamber:

(c) evacuating the interior of the chamber to a very low base pressure;

(d) forming a plasma of ions in the chamber around the target object;

(e) applying repetitive pulses of high voltage between the chamber walls and the target object independently of the forming of the plasma to draw ions in the plasma to the target object at a voltage sufficient to implant ions from the plasma into the target object, the width of the pulses being selected such that the plasma sheath surrounding the target object does not expand to contact the enclosure walls during the pulse.

APPENDIX C

PROGRAMS

The following files are stored on the attached stiffy.

The Fluid Model:

PLANAR.C	Sheridans original C program
PLANAR1.C	The modified C program.
PLANAR*.EXE	The executable files.
PLANAR*.OBJ	Theobject files.

These are modifiable, using a Turbo C compiler.

TAMIX:

TAMIX.F	FORTRAN source code for TAMIX.
SATABLEU, ATDATA	2 data files for the TAMIX program. TAMIX can regenerate these, if necessary.
INPUT.DAT	A typical input file.

To recompile TAMIX.F on the SUN (swift.ph.und.ac.za), simply type:

```
f77 tamix.f -o tamix
```

REFERENCES

1. J.R. Conrad and C. Forest
   IEEE International Conference of Plasma Science, Saskatoon, Canada, 1986, Paper 2D7, pg 28, IEEE,New York, N.Y., Catalog No. 86CH2317-6

2. J.R. Conrad, R.A. Dodd, F.J. Worzala and X. Qiu
   Plasma Source Ion Implantation: A new, cost effective, non-line-of-sight technique for ion implantation of materials., Surf. and Coatings Tech., **36**, 1988, 927-937

3. J.R. Conrad, S. Baumann, R. Fleming and G.P. Meeker
   Plasma source ion implantation dose uniformity of a 2x2 array of spherical targets., J. Appl. Phys. **65** (4), 15 February 1989, 1707-1712

4. National Research Council
   Plasma Processing of Materials., National Academy Press, Washington, D.C., 1991

5. I.J. Donnelly and P.A. Watterson
   Ion-Matrix sheath structure around cathodes of complex shape., J. Phys. D, **22**, 1989, 90-93,

6. P.A. Watterson
   Child-Langmuir sheath structure around wedge-shaped cathodes., J. Phys D, **22**, 1989, 1300-1307

7. T.E. Sheridan and M.J. Alport,
   Two Dimensional Model of Ion Dynamics during Plasma Source Ion Implantation, Appl. Phys. Lett. **64** (14) 1994

8. F.J. Worzala, J.R. Conrad, R.A. Dodd, M.B. Madapura and K. Sridharan
   Recent Developments in Plasma Source Ion Implantation., Proceedings of 7th International Conference on Ion and Plasma-Assisted Techniques, Geneva, Switzerland, May 31 -June 2, 1989

9. M.A. Lieberman
   Model of plasma immersion ion implantation., J. Appl. Phys., **66** (7), 1989, 2926-2929

10. J.W. Cipolla,Jr and M.B. Silevitch
On the temporal development of a plasma sheath., J. Plasma Physics, **25** (3), 1981, 373-389

11. R.A. Stewart and M.A. Lieberman
Model of plasma source ion implantation for voltage pulses with finite rise and fall times., J. Appl. Phys. **70** (7), 1991, 3481-3487

12. T.E. Sheridan and J.A. Goree
Analytic Expression for the Electric Potential in the Plasma Sheath., IEEE Trans. on Plasma Science, **17** (6), 1989, 884-888

13. S. Qin, C. Chan, N.E. McGruer, J. Browning and K. Warner
The Response of a Microwave Multipolar Bucket Plasma to a High Voltage Pulse., IEEE Trans. on Plasma Science, **19** (6), 1991, 1272-1278

14. J.T. Scheuer, M. Shamim and J.R. Conrad
Model of plasma source ion implantation in planar, cylindrical and spherical geometries., J. Appl. Phys. **67** (3), 1990, 1241-1245

15. J.R. Conrad
Sheath Thickness and potential profiles of ion-matrix sheaths for cylindrical and spherical electrodes., J. Appl. Phys. **62** (3), 1987, 777-779

16. M. Shamim, J.T. Scheuer and J.R. Conrad
Measurements of spatial and temporal sheath evolution for spherical and cylindrical geometries in plasma source ion implantation., J. Appl. Phys. **69** (5), 1991, 2904-2908

17. G.A. Emmert and M.A. Henry
Numerical simulation of plasma sheath expansion, with applications to plasma-source ion implantation., J. Appl. Phys. **71** (1), 1992, 113-117

18. J. Tendys, I.J. Donnelly, M.J. Kenny and J.T.A. Pollock
PIII using plasmas generated by radio frequency techniques., Appl. Phys. Lett. **53** (22), 1988, 2143-2145

19. B.Y. Tang, R.P. Fetherston, M. Shamim, R.A. Breun, A. Chen and J.R. Conrad
Measurement of ion species ratio in the Plasma Source Ion Implantation process., J. Appl. Phys., **73** (9), 1993, 4176-4180

20. S. Qin, C. Chan and N.E. McGruer
Energy distribution of boron ions during plasma immersion ion implantation., Plasma Sources Sci. Technol. O, 1991, 1-6

21. R.F. Varey and K.F. Sander
Dynamic Sheath growth in a mercury plasma., Brit. J. Appl. Phys. (J. Phys. D), Ser. 2, **2**, 541-550

22. B. Szapiro, J.J. Rocca and T. Prabhuram
Electron yield of glow-discharge cathode materials under helium ion bombardment., Appl. Phys. Lett. **53** (5), 1988, 358-360

23. B. Szapiro and J.J. Rocca
Electron emmision from glow-discharge cathode materials due to neon and argon ion bombardment., J. Appl. Phys. **65** (9), 1989, 3713-3716

24. M.M. Shamim, J.T. Scheuer, R.P. Fetherston and J.R. Conrad
Measurement of electron emission due to energetic ion bombardment in plasma source ion implantation, J. Appl. Phys, **70** (9), 4756, (1991)

25. M.M. Shamim, R.P. Fetherston, K. Sridharan and J.R. Conrad
Sheath dynamics and dose analysis for planar targets in plasma source ion implantation, Plasma Sources Sci. Technol., **2** 81, (1993)

26. R. Wei, P.J. Wilbur, W.S. Sampath, D.L. Williamson, Y.Qu and L. Wang
Tribological Studies of Ion Implanted Steel Constituents Using an Oscillating Pin-On-Disk Wear Tester, Journal of Tribology, **112**, 27-34 (1990)

27. C.K. Birdsall and W.B. Bridges
Electron Dynamics of Diode Regions, (Academic, New York, 1966)

28. C.D. Child
Phys. Rev., **32**, 492 (1911)

29. F.F. Chen
Introduction to Plasma Physics, Plenum Press, New York (1974)

30. W.H. Press, B.P. Flannery, S.A. Teukolsky and W.T. Vetterling
Numerical Recipes: The Art of Scientific Computing, Cambridge University Press (1986)

31. T.E. Sheridan
Private communication during Dr Sheridan's visit to the Plasma Physics Research Institute at the University of Natal, Durban, Jan-Feb 1993.

32. M. Widner, I. Alexeff, W.D. Jones and K.E. Lonngren
Ion acoustic excitation and ion sheath evolution., Phys. Fluids, **13**, 1970, 2532-2540

33. S.H. Han
Computer Simulation of Ion Beam Mixing, Ph.D. Thesis, Univ. of Wisconsin-Madison (1988)

34. S.H. Han, G.L. Kulcinski and J.R. Conrad
Computer Simulation of Ion Beam Mixing, Nucl. Instrum. and Meth. **B45**, 701-706 (1990)

35. R.J. Taylor, K.R. McKenzie and H. Ikezi
Rev. Sci. Instrum., **43**, 1675 (1972)

36. K. Thomas, T.E. Sheridan and M.J. Alport
A two ion fluid model for plasma source ion implantation, J. Vac. Sci. Technol. B, **12** (2), Mar/Apr 1994

37. D. Pietersen
The properties of TiN coatings produced by reactive ion plating, Atomic Energy Corporation of South Africa, Ltd, Pretoria, UCOR 482 (B/R)